Geophysical Evolution of the Moon and Asteroid 16 Psyche

By

Fiona Nichols-Fleming

B.S. Physics and Astronomy – University of Rochester (2019)

M.S. Earth, Environmental and Planetary Sciences – Brown University (2022)

Dissertation

Submitted in partial fulfillment of the requirements for the degree of Doctor of Philosophy in the Department of Earth, Environmental and Planetary Sciences at Brown University

Providence, Rhode Island

February 2024

This dissertation by Fiona Nichols-Fleming is accepted in its present form by the Department of Earth, Environmental and Planetary Sciences as satisfying the dissertation requirement for the degree of Doctor of Philosophy.

Date______________ ____
Alexander J. Evans, Brown University, Advisor

Date______________ ____
Brandon C. Johnson, Purdue University, Advisor

Recommended to the Graduate Council

Date______________ ____
Ingrid Daubar, Brown University, Reader

Date______________ ____
Victor Tsai, Brown University, Reader

Date______________ ____
Michael M. Sori, Purdue University, Outside Reader

Approved by the Graduate Council

Date______________ ____
Thomas A. Lewis, Dean of the Graduate School

Curriculum Vitae

FIONA NICHOLS-FLEMING
fiona_nichols-fleming@brown.edu

EDUCATION

PhD in Planetary Science *Anticipated 2024*
Brown University, Department of Earth, Environmental, and Planetary Sciences

Master of Science in Planetary Science *May 2022*
Brown University, Department of Earth, Environmental, and Planetary Sciences

Bachelor of Science in Physics and Astronomy *August 2015 - May 2019*
University of Rochester, Department of Physics and Astronomy
Magna Cum Laude with highest distinction (GPA: 3.96/4.00)
Minor in Mathematics

RESEARCH INTERESTS

Planetary Geophysics:
Statistical and analytical modeling of geophysical systems; the interactions between planetary surface and interior processes; analyses of spacecraft-derived datasets including gravity and altimetry

PROFESSIONAL MEMBERSHIPS

Phi Beta Kappa, Academic Honor Society (ΦΒΚ)
Sigma Pi Sigma, National Physics Honor Society (ΣΠΣ)

HONORS & AWARDS

Dwornik Best Graduate Poster Presentation Award, 54th LPSC	2023
NSF Graduate Research Fellowship, Honorable Mention	2021
Dean's Award for Symposium Presentations, Univ. of Rochester	2018
Barry M. Goldwater Scholarship, Honorable Mention	2018
Award for Excellence in Programming: Earth Hour, Univ. of Rochester	2017

RELEVANT COURSES

Core Courses
Continuum Physics of Solid Earth
Gravitational Fields and Data
Planetary Interiors
Thermodynamics & Statistical Mechanics
Astrophysical Fluid Dynamics
Planetary Surface Processes

Other Courses
Solid Earth Geophysics
Evolution of the Earth
Modern Statistics & Large Datasets
Introduction to Computer Science
Calculus & Linear Algebra
Fourier Series & Boundary Value Problems

RESEARCH EXPERIENCE

Brown University Fall 2019 - Present
Graduate Researcher
Studying planetary geophysics in our solar system with Prof. Alexander Evans at Brown University and Prof. Brandon Johnson at Purdue.

University of Rochester
Research Assistant Fall 2017 - Spring 2019
Studying of the evolution of spot coverage in main sequence stars by relating sunspot coverage to stellar variability to increase understanding of the behavior of stars older than the Sun with Prof. Eric Blackman in the form of an Independent Study.

Research Assistant Fall 2016 - Spring 2017
Simulating and studying the tidal evolution of satellites under Prof. Alice Quillen. Specific projects include the high obliquities of Pluto's smaller satellites and the dissipation of energy in a tidally evolving satellite.

The SETI Institute Summer 2018
REU Intern
Investigating the crystallinity of the Mid-Sized Moons of Saturn based on asymmetry in the 2 μm spectral ice band and its implications for activity, formation and aging with Dr. Cristina Dalle Ore through an NSF funded Research Experience for Undergraduates (REU).

Cornell University Summer 2017
REU Intern
Tracking the latitudinal and seasonal variations in the haze distribution of Titan's atmosphere using the PyDISORT radiative transfer model with Prof. Alex Hayes through an NSF funded Research Experience for Undergraduates (REU).

TEACHING EXPERIENCE

Brown University
Teaching Assistant *Spring 2023*
EEPS 0810: Planetary Geology
Provided guest lectures when the professor was out of town. Held two hours of office hours each week to assist students with concepts and homework assignments, responsible for grading homework and exams

University of Rochester
Volunteer Physics Tutor *Fall 2016 - Spring 2019*
Hold a two hour per week tutoring session to work with students on problem solving skills and various physical concepts

Laboratory Teaching Intern *Spring 2019*
PHY 143: Waves and Modern Physics (Honors)
Monitor and assist with monthly labs and hold office hours on off weeks to help students with data collection, analysis, and lab report writing

TEACHING EXPERIENCE CONT.

University of Rochester
Workshop Leader *Fall 2016*
CSC 161: Intro to Programming
Hold a weekly 75 minute workshop, responsible for grading quizzes

Summer Program Co-Instructor *Summer 2016*
Designing an introductory level physics curriculum, teaching basic physics concepts to high school girls, and organizing educational field trips and guest lectures.

INVITED PRESENTATION

"Core Solidification & Contraction on 16 Psyche," MIT Planetary Lunch Seminar, November 2022.

CONFERENCE PRESENTATIONS

Nichols-Fleming, Evans, Johnson "Core Solidification and Contraction on 16 Psyche," LPSC Meeting 54, poster, 2023.

Nichols-Fleming, Evans, Johnson, Sori "Porosity Evolution of Psyche and Other M-Type Asteroids," LPSC Meeting 53, talk, 2022.

Nichols-Fleming, Evans, Johnson, Tikoo "Short-Lived Lunar Dynamos Powered by the Accretion of Cold Impactor Core Material," LPSC Meeting 52, virtual talk, 2021.

Nichols-Fleming, Evans, Johnson, "Short-Lived Lunar Dynamos Driven by the Accretion of Cold Impactor Material," LPSC Meeting 51, talk, 2020. Meeting Cancelled.

Nichols-Fleming and Blackman, "Constraining Spot Coverage as a Function of Age in Main-Sequence Stars," University of Rochester Undergraduate Research Exposition, talk, 2018.

Nichols-Fleming, Corlies, Hayes, Ádámkovics, "Tracking Short-Term Variations in Titan's Haze Distribution," LPSC Meeting 49, talk, 2018.

Nichols-Fleming, Corlies, Hayes, Ádámkovics, "Tracking Short-Term Variations in Titan's Haze Distribution with SINFONI VLT," CUWiP at RIT, talk, 2018.

Nichols-Fleming, Corlies, Hayes, Ádámkovics, "Tracking Short-Term Variations in Titan's Haze Distribution with SINFONI VLT," Titan Surface Meeting, talk, 2017.

PUBLICATIONS

Fiona Nichols-Fleming, Alexander J. Evans, Brandon C. Johnson, Michael M. Sori, "Moment of Inertia and Tectonic Record of Asteroid 16 Psyche May Reveal Interior Structure and Core Solidification Processes," in preparation.

Fiona Nichols-Fleming, Alexander J. Evans, Brandon C. Johnson, Sonia M. Tikoo "The Influence of Cool Impactor Accretion on the Early Lunar Paleomagnetic Record," in preparation.

Fiona Nichols-Fleming, Alexander J. Evans, Brandon C. Johnson, Michael M. Sori, "Porosity Evolution in Metallic Asteroids: Implications for the Origin and Thermal History of Asteroid 16 Psyche," JGR: Planets, 127, e2021JE007063, 2022.

Fiona Nichols-Fleming, Paul Corlies, A. G. Hayes, M. Ádámkovics, et al., "Tracking seasonal variations in the haze distribution of Titan's atmosphere with SINFONI VLT," Planetary Science Journal 2, 180, 2021.

Cristina M. Dalle Ore, Christopher J. Long, **Fiona Nichols-Fleming**, Francesca Scipioni, et al., "Dione's Wispy Terrain: A Cryovolcanic Story?" Planetary Science Journal 2, 83, 2021.

Fiona Nichols-Fleming, Eric G. Blackman, "Determination of the star-spot covering fraction as a function of stellar age from observational data," MNRAS 491, Issue 2, 2706-2714, 2020.

Alice C. Quillen, **Fiona Nichols-Fleming**, Yuan-Yuan Chen, Benoît Noyelles, "Obliquity evolution of the minor satellites of Pluto and Charon," Icarus 293, 94-113, 2017.

Acknowledgements

Throughout my time as a grad student at Brown I have learned so much and grown as a scientist and as a person. My success and all that I've learned is largely thanks to the support of numerous people including the faculty, staff, and other students within the DEEPS community, my friends, and my family. I extend my deepest appreciation to each and every one of you, but I especially want to acknowledge and thank a handful of people by name.

I first want to thank my advisors Alex Evans and Brandon Johnson who have been incredibly supportive throughout my time at Brown. I would not have been able to develop into the scientist I am today without your guidance and support over the last four years. I am deeply grateful for all you have taught me about science and academia. I also want to thank the members of my thesis committee: Ingrid Daubar, Victor Tsai, and Mike Sori. You have each taken time to share your insight with me and helped me improve my confidence and communication skills as well as the quality of my research contained within this dissertation. I am additionally very grateful for the research advisors I had prior to joining Brown for my PhD: Alice Quillen, Alex Hayes, Cristina Dalle Ore, and Eric Blackman. You have all taught me new things about what it means to be a scientist and helped guide my career to where it is today. And to Sam Birch and Paul Corlies, some of the first grad students I ever talked to back in 2016, thank you for welcoming me to the planetary science community, teaching me what it means to be a PhD student, and showing me that grad school can be fun even if it is a lot of work. I have been so happy to see you both find success in your careers.

I want to thank the amazing community of grad students we have here in DEEPS, both past and present, without you all I wouldn't have been able to get this PhD. Particularly, to the current and former GHOSST Lab members – Janie, Matt, Evan, and Steven – it has been an

honor to share my single braincell with you. In all seriousness, I have loved working alongside of you and am deeply grateful for the wide variety of knowledge I have gained from you. To all the other DEEPS grad students I've gotten to know in the past four years – Erica, Meg, Cody, Kierra, Carol, Beau, and Seb to name just a few – your friendship, advice, GCB nights, and beach and ski trips have brought me so much joy and have made my time at Brown truly special. Moreover, I would never have even made it to grad school without the love and support of my friends from Rochester. To Gen, Ryan, Bo, Jeremy, Adina, Josh, and Jack, thank you for all the amazing memories and help with physics homework through the years, I can't wait to see you all receive your PhDs and find success as well.

Most importantly, I want to thank my family. To my parents, thank you for your unconditional support in following my dreams for the past 26 years. From writing me the practice algebra problems I used to request for fun to driving me all over the northeast for track and gymnastics meets, you have always gone above and beyond to encourage my interests and you inspire me to be a better version of myself every day. To Nathaniel and Mariah, thank you for reminding me to keep humor in my life and for being the real adults of the family while I stay in school maybe forever. I am so proud of all you have accomplished and so grateful that we've been able to spend many holidays with the family at your place. And to their newest family member and my niece Hazel, you won't be old enough to get through this whole thing for a long time, but I hope someday you'll let me tell you all about space and the planets. Finally, to Tyler, thank you for being by my side through everything from years of long distance to a global pandemic on top of the typical stress of grad school. I am incredibly lucky that I met you so early in my life and that I will have you by my side for support and for countless adventures in the many years to come.

Table of Contents

List of Tables

List of Figures

Introduction

Fiona Nichols-Fleming

Department of Earth, Environmental and Planetary Sciences, Brown University, Providence, RI

1 Understanding the Thermal Evolution of Planetary Bodies

Modern surfaces of planetary bodies are shaped by their early thermal and interior evolution. In this chapter I provide a concise, historical summary of what is known about planetary thermal evolution and the interiors of the Moon and asteroid 16 Psyche, in particular. I first introduce the general concepts and processes of thermal evolution inside planetary bodies in this section. Then, in Section 2, I detail the historical knowledge of the thermal histories of the Moon and Psyche. Finally, I summarize the chapters of this dissertation in Section 3.

In the first few million years of solar system formation, pebbles grow to bodies on the scale of a few kilometers, called planetesimals, via mechanisms that remain uncertain (e.g., Morbidelli et al., 2012). The heating of planetesimals in this early era of the solar system is dominated by the decay of short-lived radionuclides ^{26}Al and ^{60}Fe. Due to the very short half-lives of these radionuclides (~0.75 and ~1.5 Myr for Al and Fe, respectively; e.g., Ghosh et al., 2006), their decay can produce a large amount of heat in a short period of time and these radionuclides are canonically thought to be responsible for melting and differentiation of asteroids and smaller bodies throughout the solar system (Ghosh et al., 2006 and references therein). To begin differentiation, a process in which multiple phases of different densities (generally iron and silicate phases) are separated, internal temperatures must reach the onset of silicate melting at ~1,400 K (Takahashi, 1983). Based on this requirement and thermal models of planetesimals including the decay of ^{26}Al, the lower limit on the size of differentiated bodies is a radius of only ~ 20 km, provided that the bodies formed within the first ~2 Myr of solar system evolution (Hevey & Sanders, 2006). Additional heat will also be released throughout differentiation due to the changes in gravitation potential energy associated with the changing internal distribution of mass. For larger bodies such as moons and planets, further energy is gained from continued accretion and impact events which allows for both ongoing and delayed stages of melting and differentiation.

The longer-term thermal evolution of planetary bodies is then determined by the balance between long-term heat production and the loss of internal heat. While ^{26}Al and ^{60}Fe produce large amounts of heat within the first few million years of solar system formation, radionuclides of potassium, thorium, and uranium have much longer half-lives and can continue to produce heat throughout the silicate layers of a planetary body for billions of years. Simultaneously, the planetary body's internal heat can be lost via conduction and/or convection. Conduction is a method of heat transfer in which heat is transported via net collisions of molecules within a material. This form of heat transfer occurs in any system where there is a spatial difference in temperatures. Alternatively, convection requires motion of material and will only become the dominant form of heat transfer in cases where the buoyancy forces greatly exceed the viscous forces within a fluid. In these cases, heat can be lost much faster than in a body of the same size where conduction is the dominant mechanism of heat transfer. A more detailed discussion of heat transfer in planetary bodies can be found in Turcotte & Schubert (2002). While the thermal evolution of all planetary bodies relies on these fundamental processes, the particular conditions of a body's formation will result in a unique evolutionary history.

2 Thermal Histories of the Moon and Psyche

This dissertation focuses on the thermal history and interiors of two particular planetary bodies: the Moon and asteroid 16 Psyche. While relying on the same fundamental physics, the Moon and Psyche formed in very different environments and their radii are different by over an order of magnitude (1,737 and 111 km, respectively; Shepard et al., 2021; Williams et al., 2014), which results in significant differences in internal structure and thermal evolution. Throughout the next two sections I cover a historical overview of the understanding of the interiors of the Moon and Psyche, respectively, how they have changed over time and where the chapters of this dissertation fit in to the evolving fields.

2.1 The Moon

The Moon has been a part of different cultures and mythologies throughout all human history. However, the interior of the Moon has historically been, and remains to this day, largely a mystery. The very first recorded calculation of the mass of the Moon was published by Isaac Newton in the first edition of his *Principia* based on measurements of sea tides (Newton, 1687). Through the three editions of this work, Newton determined that the Moon was approximately $1/40^{th}$ the mass of the Earth, however this is approximately twice as massive as the modern estimates due to complications in measuring the height of tides (e.g., Hughes, 2002). The estimates of lunar mass relative to the mass of the Earth from tidal measurements continued to be refined through to the 1800s as described in Hughes (2002), at which point the ratio of the mass of the Earth to the Moon had decreased to between 78 and 89. Alternatively, Kepler's 3^{rd} law with modifications based on Newton's second law of gravitation can provide estimates of the Moon's mass based on the semi-major axis and period of the lunar orbit. These estimates were limited by the uncertainty in the distances between the Earth and the Moon and the Earth and the Sun, and were improved with developing telescope accuracy until, prior to the Apollo mission, two slightly different accepted values of this ratio in the literature were 81.53 and 81.45 (e.g., Gurnette & Woolley, 1974). After the Apollo missions, where retroreflectors were placed on the lunar surface to accurately measure the travel time of ranged lasers and therefore distance between the Earth and Moon, this mass ratio has become one of the most accurately known astronomical values at 81.300588 (Seidelmann, 1992). Since the radius of the Moon has been known to reasonable accuracy for thousands of years, the variations in lunar mass estimates were the cause of large variations in estimates of the lunar bulk density as well. Newton's early mass estimates suggested that the Moon was more dense than the Earth. However, by the 1800s the lunar density estimates were around 3,400 kg/m^3, very close to the modern estimate of 3,340 kg/m^3 (e.g., Hughes, 2002 and references therein).

Before the space-age, any knowledge of the lunar interior beyond the mass and bulk density relied on Earth-based observations of the Moon's orbital and rotational motion. The physical libration of the Moon, small oscillations in the rotation and pole direction, can provide inferred values of the three principal moments of inertia (MOIs) as described in MacDonald (1963). The ratio of these values to the lunar MR^2 can provide a non-unique model of the distribution of mass within the Moon. These early derivations suggested that the outer part of the Moon was denser than the interior, although the calculations included many uncertainties and the extent of differentiation within the Moon remained unclear (Jeffreys, 1961; MacDonald, 1963). Given that there was no evidence at the time that the Moon had a core at all, let alone a convecting fluid portion of a core, there was no reason to expect that the Moon currently or ever had a magnetic field. Early observations of the shape of the Moon also suggested that it was not in hydrostatic equilibrium, and therefore there must be some internal strength or internal convection to support these deviations from equilibrium shape (Urey & Korff, 1952). This figure could be supported by a cold outer shell with a molten interior (Urey & Korff, 1952); however, an assumed chondritic composition would result in the melting of a homogeneous Moon. Therefore, the observed figure of the Moon is incompatible with a homogeneous chondritic composition, and it instead suggests that the moon has less radiogenic material than chondrites or that the moon is differentiated (MacDonald, 1963; Urey, 1957). These uncertainties in the structure of the lunar interior were largely thought to reflect the uncertainties in the origin of many lunar surface features, which planetary scientists have been working to explain for decades via the Apollo missions and subsequent lunar exploration.

As NASA (the National Aeronautics and Space Administration) and other space agencies have successfully completed more and more missions focused on lunar exploration, the presence of an iron core has become widely accepted. However, the exact size, composition, and phase of the lunar core are still debated to this day. Through the Apollo program, the seismometers and magnetometers that were placed on the lunar surface and the lunar samples that were returned to Earth revolutionized the understanding of the lunar interior. As discussed in more detail below, the Apollo magnetometers detected much higher natural remanent magnetizations than anticipated with an inferred lunar source (e.g., Dyal et al., 1974 and references therein). This implies that the Moon has an iron core that produced a magnetic field at some point in its history, which could be consistent with the measured MOI as long as it is smaller than 20% of the lunar radius (Runcorn et al., 1970). However, this level of differentiation was not fully supported by the geochemical data at the time. The depletion of Apollo samples in siderophile elements does suggest removal of iron towards the interior, but this could be consistent with an iron enriched silicate core rather than a true iron core (see Hinners, 1971 for a summary). The lunar seismic network was also able to provide data which indicated some level of seismic softening in the deep interior that could be consistent with many different interior compositions including a fluid core, however a core with a radius less than 500 km, if present, could not be resolved (e.g., Toksoz, 1974 and references therein). Following the successful Clementine and Lunar

Prospector missions, completed in 1995 and 1999, respectively, measurements of geophysical properties such as the MOI and tidal love number were improved, and further analysis of Apollo samples and data was completed. The updated value for the normalized MOI was found to be below that of a uniform sphere indicating a small iron core (Konopliv et al., 1998) or a slightly larger iron-rich silicate core (e.g., Wieczorek, 2006). Continued analysis of the Apollo seismic data provided tentative evidence of a small low-velocity core (see Wieczorek, 2006 for summary), but the difference between iron and iron-rich silicate could not be distinguished. Most recently, two groups in 2011 independently interpreted a solid-liquid boundary reflection in the seismic data to estimate a core radii (Garcia et al., 2011; Weber et al., 2011) and the latter group also presented an estimate for a solid inner core radii and suggested that there is a low seismic velocity layer in the deep mantle. These seismic models were used alongside the vastly improved gravity data from the GRAIL mission (Gravity Recovery and Interior Laboratory; Zuber et al., 2013) to produce interior models for the Moon with and without the inclusion of a low-velocity layer in the deep mantle (Matsuyama et al., 2016; Williams et al., 2014). While this model is widely used today, many uncertainties remain including the potential presence and thickness of a low-velocity layer in the deep mantle and the thermal structure of the deep mantle through time.

Together with developing knowledge of the lunar interior, knowledge of the history of magnetism on the Moon has been overturned through the space-age and beyond. Prior to the Apollo missions, there was no evidence that the Moon had any current magnetic field or any remanent magnetization in the crust (as summarized by Dyal et al., 1974). However, the first magnetometer on the lunar surface, placed by Apollo 12 astronauts, found evidence for an intrinsic lunar magnetic field via direct detection of higher than expected remanent magnetization of the lunar crust (Dyal et al., 1970). Following these observations, further studies of the lunar magnetic field were developed and data from the pre-Apollo Explorer 35 mission was reanalyzed finding indirect evidence of several regions of magnetized lunar crust (Mihalov et al., 1971). After the conclusion of the Apollo missions, it became widely accepted that large regions of crust across the lunar surface are magnetized, however, the source of the magnetic field that is recorded in the crust was highly debated and local sources rather than a global dynamo were preferred (e.g., Dyal et al., 1974). Furthermore, analysis of returned Apollo samples provided a record of magnetic field strengths ranging between ~10 and ~100 μT that were recorded up to 4.6 Ga based on the host rock ages (see Figure 1; Fuller & Cisowski, 1987; Wieczorek, 2006).

The methods used to determine paleointensities during the Apollo-era are now considered to be a bit antiquated, and major developments have been made in the understanding of rock magnetism to improve the fidelity of paleointensity experiments. To determine the paleointensity recorded by an igneous sample, the natural remanent magnetization is assumed to be acquired as the sample cooled through its Curie temperature in a planetary field. This type of magnetization is called thermal remanent magnetization (TRM) and the intensity of this magnetization is directly proportional to the strength of the field magnetizing the sample, i.e., the paleointensity, via the TRM susceptibility of the particular rock sample. Under these assumptions, paleointensities are typically determined via two main processes where the samples are demagnetized in a stepwise fashion. This demagnetization is often done by either the application of alternating magnetic fields of increasing intensity at room temperature or by heating to increasing temperatures in a zero-field environment, called the isothermal remanent magnetization at saturation (SIRM) and Thellier-Thellier methods, respectively. These step-by-step demagnetization processes provide measurements of the paleointensity of the field responsible for the magnetization of the sample via the product of the slope of the demagnetization trends and a calibration constant specific to the method used. However, the thermal Thellier-Thellier method must be done in an atmosphere of the same redox state as the sample formed under to prevent the occurrence of oxidation reactions (e.g., Suavet et al., 2014). This is very difficult to replicate in a laboratory for lunar samples, and therefore non-thermal methods are mainly used in analysis of Apollo samples. Further details of these methodologies can be found in Tikoo & Evans (2022). Using these improved experimental methods, a high-fidelity history of lunar paleointensities is constructed, as shown in Figure 2, where it can be seen that the range of intensities seen in the Apollo-era analysis is preserved, but there is far less variability in the data (e.g., Mighani et al., 2020; Weiss & Tikoo, 2014). Non-thermal measurements of paleointensities have an inherent uncertainty of a factor of ~2 – 5 (e.g., Gattacceca & Rochette, 2004; Stephenson & Collinson, 1974; Yu, 2010), but beyond this some of the previously observed variability may be indicative of real variation in the lunar dynamo (e.g., Jung et al., 2021) and continued paleointensity experiments are necessary to determine the true variability of the early lunar dynamo.

While many developments have been made in understanding rock magnetism, many questions remain for the lunar dynamo including how the early high intensities were powered and whether the samples truly imply a core dynamo origin. It has long been accepted by the lunar community that magnetized Apollo samples represent a magnetic field produced by a core dynamo because most of these samples cooled over periods longer than the lifetimes of impact-related fields and had no evidence of major shock features (as summarized in Tikoo & Evans, 2022). However, recent analysis of five Apollo samples, has found that they do not preserve a magnetic signature even though four of these five samples should have been able to record a high intensity magnetic field if it was present at the time of their cooling (Tarduno et al., 2021). It has been argued by Tarduno et al. (2021) that these results indicate that the Moon did not have a long-lived core dynamo, but this is an ongoing area of debate within the lunar paleomagnetism community. Under the assumption that the magnetized samples do represent fields from an ancient lunar core dynamo, scaling laws based on fundamentals of electrodynamics as well as observations of magnetic fields in both planetary bodies and rapidly rotating stars can estimate the required super-adiabatic heat flux across the core-mantle boundary for a given surface field intensity (Christensen et al., 2009). These scaling laws, even when considered with a maximized energy budget within the Moon, indicate that there is not enough internal energy to sustain a core dynamo of both the paleofield intensities and longevity indicated by the lunar samples (Evans et al., 2018). Many hypotheses have been proposed to explain the early, high-intensity era of the lunar paleointensity record separately from the long-lived portion of the lunar dynamo including, but not limited to, large impact-driven differential rotation of the lunar core and mantle (Le Bars et al., 2011), influence from a basal magma ocean (Scheinberg et al., 2018), and the foundering of cool titanium-rich material to the core-mantle boundary (Evans & Tikoo, 2022). Another such process in which cool material from the cores of large impactors reaches the lunar core-mantle boundary and promotes a temporarily enhanced lunar dynamo is discussed in more detail in Chapter 2 of this dissertation. However, there is still no consensus for what process(es) explain the lunar paleomagnetic record.

2.2 Asteroid 16 Psyche

Asteroid (16) Psyche became the 16th asteroid ever discovered on March 17, 1852, by the Italian astronomer Annibale de Gasparis. This first observation of Psyche and subsequent observations from the first half of 1852 are described in Runkle (1852) and Ferguson (1852). Psyche is one of numerous asteroids that make up the asteroid belt, a region of the solar system between Mars and Jupiter. The region between Mars and Jupiter was first considered by Johannes Kepler in 1596, who noticed that the gap between their orbits appeared too large and suggested that there may be an additional planet somewhere between the two orbits. Over the next two hundred years, many astronomers searched for this missing planet, and in 1802 the first asteroid Ceres was discovered followed by another three (Pallas, Juno, and Vesta) over the next 5 years. A more detailed history of the asteroid belt can be found in Peebles (2000), but the total mass is now know to be $\sim 2.6 \times 10^{21}$ kg or ~3.5% of the mass of the Moon (Kuchynka & Folkner, 2013) and the vast majority of this mass is made up of asteroids thought to be rocky in composition (e.g., DeMeo & Carry, 2013).

Since Psyche's discovery in the 19th century, ongoing observations have suggested that Psyche has a very metal-rich surface and may even be an ancient remnant core of a planetesimal from the early solar system (e.g., Bell et al., 1989; Elkins-Tanton et al., 2020; Ostro et al., 1985). In addition to the relatively featureless spectrum in the visible and near infrared wavelengths and similarity to iron meteorites, which are discussed further below, Psyche has been observed to have a very high radar albedo (e.g., Ostro et al., 1985; Shepard et al., 2008, 2010, 2015, 2017). Psyche's average radar albedo of 0.34 (Shepard et al., 2021) is much higher than that the typical values of 0.14 – 0.15 for the more rocky C- and S-type asteroids (Magri et al., 2007) and this is consistent with and has long been interpreted as indicated a nearly entirely metal surface composition (Ostro et al., 1985). Measurements of the thermal inertia of Psyche have varied widely with two studies finding high values consistent with a metal rich surface (de Kleer et al., 2021; Matter et al., 2013) and one finding a very low thermal inertia value more consistent with a rocky composition (Landsman et al., 2018). These inconsistencies continue with several detections of silicates on the surface (Hardersen et al., 2005; Ockert-Bell et al., 2008, 2010; Sanchez et al., 2021) and hydrated mineral phases (Takir et al., 2016), both of which suggest Psyche may have a more complicated composition than previously thought.

A major development in asteroid science came with the construction of taxonomic classification schemes for all known asteroids. The first asteroid taxonomy was constructed based on visible and near-infrared spectrophotometry, polarimetry, and infrared radiometry of 110 asteroids and only two groups were formally created: siliceous or S-type asteroids and carbonaceous or C-type asteroids (Chapman et al., 1975). This division was solely based on the measured physical parameters but is thought to generally represent the expected composition of the C- and S-type asteroids based on inferred compositions from spectral similarities between the asteroids and meteorite analogs. Additionally, a group called unclassified or U-type asteroids was created for anomalous spectra in the sample, including asteroid (16) Psyche. Even at this time, similarities between the observed spectra of Psyche and those of iron meteorites or metal-rich enstatites were acknowledged. Further observations of asteroids led to the formation of the metallic or M-type group, meant to represent asteroids with suggested iron-nickel compositions (Zellner & Gradie, 1976), and Psyche is the largest of this group of asteroids. These early classification schemes were revolutionized by the incorporation of the eight-color photometric asteroid survey results and additional radiometric results (Tholen, 1984) and again decades later by the addition of near-infrared observations (DeMeo et al., 2009). In these most recent taxonomic schemes, Psyche, and the other M-type asteroids, are part of the X-complex, a group with similarly featureless spectra, but a range of albedos and therefore likely a range of compositions as well.

As mentioned previously, comparisons with known meteorites are a common strategy for improving our understanding of asteroids and asteroid classes. Perhaps the most famous example of this is the link between the howardite-eucrite-diogenite meteorites and the asteroid Vesta (e.g., McSween Jr. et al., 2013). For Psyche and the M-type asteroids, the most common comparisons made are those with iron meteorites due to the numerous observations indicating a metal-rich surface composition and Psyche is often hypothesized to be a parent body for some portion of the iron meteorites. However, comparisons have also been made between Psyche and the stony-iron meteorites such as pallasites and mesosiderites. A more detailed discussion of Psyche's potential meteorite analogs can be found in Elkins-Tanton et al. (2020), but generally, each of these potential links to classes of meteorites implies something different for the formation and evolution of Psyche. For example, the cooling rates of the iron meteorites and pallasites are highly variable and this is commonly interpreted as evidence that planetesimal cores experience mantle-stripping impact events (e.g., Yang et al., 2007, 2008; Yang, Goldstein, Michael, et al., 2010; Yang, Goldstein, & Scott, 2010). If Psyche is the parent body for some of these meteorites, it would imply a differentiated internal structure that has undergone one or more mantle-stripping events. The mesosiderites however, are crust or mantle material mixed with metal (e.g., Mittlefehldt et al., 2018) and therefore, if Psyche is the parent body of this class of meteorites, the implied composition would be more representative of a body in which the metals and silicates remain mixed. Continued ground-based and additional spacecraft observations of Psyche are required to determine which class of meteorites, if any, truly originated from Psyche.

While taxonomic classifications and spectral similarities to meteorites may inform the surface composition of asteroids, any knowledge of Psyche's interior relies on bulk measurements such as mass and density. The first estimation of Psyche's mass was reported in

2000 based on a close encounter between Psyche and a smaller asteroid, (94) Aurora, in 1937 (Viateau, 2000). Based upon the deflection in Psyche's orbital trajectory after this encounter, they found a mass of $1.74 \pm 0.52 \times 10^{19}$ kg, corresponding to an average density of $1{,}800 \pm 600$ kg/m^3 under the assumption of spherical body with a mean diameter of 264 ± 4 km. Through time, additional close encounters between Psyche and other small bodies have been detected and more accurate shape models have been produced, which has allowed for higher precision mass and density measurements as summarized in Elkins-Tanton et al. (2020). While mass and bulk density estimates prior to 2010 had high amounts of variability (see Figure 3), modern estimates have converged on a bulk density of $4{,}000 \pm 200$ kg/m^3 (Shepard et al., 2021). Although this density is significantly lower than those of meteoritic metals such as kamacite (7,870 kg/m^3; Smyth & Mccormick, 1995) and thus is seemingly incompatible with the exposed core hypothesis, Psyche remains one of the densest known asteroids.

The combination of surface observations and bulk measurements for Psyche presents a difficult problem to reconcile for the asteroid's formation and evolution. Perhaps the simplest explanation of the metal-rich surface would be the accretion of unmelted, primitive material in a highly reduced state where the iron is in the form of metal, potentially from material near the young Sun (e.g., Weidenschilling, 1978). Similarly, the traditional formation theory that Psyche is a core of a differentiated planetesimal that underwent one or more mantle stripping events is a relatively straightforward way to produce a large body with a metal-rich surface. In this model, glancing impact events between planetesimals during the first few million years of solar system formation lead to removal of mantle material from the smaller planetesimal and may eventually leave an isolated planetesimal core (e.g., Asphaug et al., 2006; Asphaug & Reufer, 2014). While both of these hypotheses readily explain the metal-rich surface observations, the predicted densities of bodies formed by these mechanisms are twice that measured for Psyche and therefore these scenarios on their own are not consistent with our current understanding of the asteroid. A potential solution to this density disparity that doesn't require the inclusion of any silicate material is the inclusion of a large amount of pore space. As discussed in Elkins-Tanton et al. (2020), Psyche's density would require a ~52% bulk porosity, however, a small porous iron body may experience a large amount of porosity removal via viscous flow. This process is considered in more detail and a high porosity metal composition is found to be unlikely for Psyche in Chapter 3 of this dissertation. Alternatively, some hypothesize that Psyche is a mix of metal and silicates that may be a parent body for stony-iron meteorites such as mesosiderites (Viikinkoski et al., 2018). However, a recent study suggests that pyroxene signatures observed in mesosiderite samples should be preserved on their parent body, regardless of collisional history and therefore the very low amount of pyroxene observed on Psyche is inconsistent with this hypothesized composition and formation scenario (Libourel et al., 2023). The final formation process often considered is that Psyche is a differentiated planetary body with a silicate mantle of unknown thickness (e.g., Kim & Hirabayashi, 2022). This hypothesis could but is not required to include one or more mantle striping impact events and is shown in Figure 4 along with the hypothesis of a primitive, highly-reduced iron composition. Furthermore, models of Psyche that contain a silicate outer layer must also include a mechanism to bring metal to the surface to match existing observations. While this could be done by impacts, it has also been hypothesized that fluid core material could intrude into a silicate mantle and potentially reach a planetesimal's surface in a process called ferrovolcanism (Johnson et al., 2020; illustrated in Figure 5). The true level of surface variability is still unknown, and therefore, the extent of any hypothesized process to bring iron to the surface remains unknown as well.

To address the many uncertainties for Psyche, a Discovery-class NASA mission to Psyche was proposed and selected in 2017. The primary science objective of this mission is to understand the formation of the asteroid Psyche and therefore determine if it is part or the whole of a planetesimal core (e.g., Elkins-Tanton et al., 2022). As Psyche is the largest of the class of M-type asteroids, this mission may also reveal the origin of a whole class of objects within the asteroid belt and how their formation fits with the evolution of the early solar system. The spacecraft's instrument suite contains a multispectral imager, a magnetometer, and a gamma-ray and neutron spectrometer. These instruments, along with the planned gravity investigation, will discern Psyche's structure and formation process upon the mission's arrival in 2029 assuming the current launch window in October of 2023 (e.g., Hart et al., 2018; Polanskey et al., 2018). In the meantime, models of the hypothesized structures for Psyche can be created and related to observable features that may be detected by the Psyche spacecraft. One such model of the thermal evolution of a differentiated body with a relatively thin outer silicate layer and its influence on MOI and global contraction and faulting is described in Chapter 4 of this dissertation.

3 Summary

The purpose of the work in this dissertation is to study the magnetic and thermal evolutions of two early solar system bodies: the Moon and Psyche. The individual chapters of this dissertation, while relying on the same fundamental physics, are intended to be complete individually as peer-reviewed publications, and therefore there may be some repetition in introductory information.

In Chapter 2, "The Influence of Cool Impactor Accretion on the Early Lunar Paleomagnetic Record," we investigate impactor material as a novel source of energy for the ancient lunar dynamo. Analysis of Apollo samples suggests that the Moon's early core dynamo had surface field strengths on the same order of magnitude as the Earth's current field strength (e.g., Weiss & Tikoo, 2014). However, with the much smaller core size of the Moon, there does not appear to be enough internal energy to power the dynamo strengths suggested by the Apollo samples (Evans et al., 2018). Chapter 2 outlines the limitations for impact scenarios in which an enhanced magnetic field may occur. In cases where cool impactor core material is able to reach the lunar core-mantle boundary, enhanced field strengths could last as long as thousands of years and portions of the largest scale impact melt sheets may be able to record their associated enhanced magnetic fields.

Chapter 3, "Porosity Evolution in Metallic Asteroids: Implications for the Origin and Thermal History of Asteroid 16 Psyche," presents the thermal requirements for a high porosity iron asteroid. Psyche, and many other M-type asteroids, have surface observations indicating a high metal content (e.g., Shepard et al., 2008, 2010, 2015), but bulk densities much lower than expected for a purely metal body (e.g., Descamps et al., 2008; Elkins-Tanton et al., 2020; Marchis et al., 2021; Pätzold et al., 2011; Sierks et al., 2011). One hypothesis to reconcile these observations is that M-type asteroids may be iron rubble piles with porosities $\gtrsim$ 50%. In this chapter we model the viscous removal of pore space to determine the thermal conditions required to preserve high porosity iron bodies. We find that these bodies must have cooled below 800 – 900 K prior to the addition of porosity, which is expected to take 10s to 100s of Myrs (e.g., Bryson et al., 2015; Scheinberg et al., 2016; Tarduno et al., 2012). We expect the catastrophic events able to add ~50% porosity to occur prior to these timescales, and therefore do not favor this structure for Psyche. This work is reproduced with permission from Nichols-Fleming et al. (2022).

In Chapter 4, “Moment of Inertia and Tectonic Record of Asteroid 16 Psyche May Reveal Interior Structure and Core Solidification Processes,” we investigate a different formation scenario for Psyche. To explain the relatively low density previously discussed, Psyche may have an outer silicate layer of unknown thickness in addition to an iron core. Along with uncertainty in silicate layer thickness from existing data, analysis of the cooling rates of iron meteorites suggests that core solidification in small bodies such as Psyche could progress from the top down or from the bottom up (Yang et al., 2008; Yang, Goldstein, Michael, et al., 2010). In this chapter, we make predictions for the extent of radial contraction and moment of inertia values from models of varying silicate layer thickness, core sulfur content, and core solidification direction. We find that the Psyche spacecraft should be able to independently determine the thickness of an outer silicate layer on Psyche based on estimates of radial contraction from thrust faults, if they are observed on the surface, and the moment of inertia measured by the spacecraft should be able to distinguish the direction of core solidification. This work is being prepared for submission to *JGR: Planets*.

In the final chapter of this dissertation, I briefly summarize each project contained within this dissertation and discuss future work that can build upon this dissertation and address some of the outstanding questions for the Moon and Psyche. With the Artemis missions planning further human exploration of the Moon and a dedicated spacecraft planned to arrive at Psyche in 2029, the next few decades will surely contain major developments in the fields of thermal and magnetic modeling of early solar system bodies.

References

Asphaug, E., & Reufer, A. (2014). Mercury and other iron-rich planetary bodies as relics of inefficient accretion. *Nature Geoscience*, *7*, 564–568. https://doi.org/10.1038/ngeo2189

Asphaug, E., Agnor, C. B., & Williams, Q. (2006). Hit-and-run planetary collisions. *Nature*, *439*, 155–160. https://doi.org/10.1038/nature04311

Bell, J. F., Davis, D. R., Hartmann, W. K., & Gaffey, M. J. (1989). Asteroids: the big picture. In R. P. Binzel, T. Gehrels, & M. S. Matthews (Eds.), *Asteroids II* (pp. 921–945).

Bryson, J. F. J., Nichols, C. I. O., Herrero-Albillos, J., Kronast, F., Kasama, T., Alimadadi, H., et al. (2015). Long-lived magnetism from solidification-driven convection on the pallasite parent body. *Nature*, *517*(7535), 472–475. https://doi.org/10.1038/nature14114

Chapman, C. R., Morrison, D., & Zellner, B. (1975). Surface properties of asteroids: A synthesis of polarimetry, radiometry, and spectrophotometry. *Icarus*, *25*(1), 104–130. https://doi.org/10.1016/0019-1035(75)90191-8

Christensen, U. R., Holzwarth, V., & Reiners, A. (2009). Energy flux determines magnetic field strength of planets and stars. *Nature*, *457*(7226), 167–169. https://doi.org/10.1038/nature07626

DeMeo, F. E., & Carry, B. (2013). The taxonomic distribution of asteroids from multi-filter all-sky photometric surveys. *Icarus*, *226*(1), 723–741. https://doi.org/10.1016/j.icarus.2013.06.027

DeMeo, F. E., Binzel, R. P., Slivan, S. M., & Bus, S. J. (2009). An extension of the Bus asteroid taxonomy into the near-infrared. *Icarus*, *202*(1), 160–180. https://doi.org/10.1016/j.icarus.2009.02.005

Descamps, P., Marchis, F., Pollock, J., Berthier, J., Vachier, F., Birlan, M., et al. (2008). New determination of the size and bulk density of the binary Asteroid 22 Kalliope from observations of mutual eclipses. *Icarus*, *196*(2), 578–600. https://doi.org/10.1016/j.icarus.2008.03.014

Dyal, P., Parkin, C. W., & Sonett, C. P. (1970). Apollo 12 Magnetometer: Measurement of a Steady Magnetic Field on the Surface of the Moon. *Science*, *169*(3947), 762–764. https://doi.org/10.1126/science.169.3947.762

Dyal, P., Parkin, C. W., & Daily, W. D. (1974). Magnetism and the interior of the Moon. *Reviews of Geophysics*, *12*(4), 568–591. https://doi.org/10.1029/RG012i004p00568

Elkins-Tanton, L. T., Asphaug, E., Bell, J. F., Bercovici, H., Bills, B., Binzel, R., et al. (2020). Observations, Meteorites, and Models: A Preflight Assessment of the Composition and Formation of (16) Psyche. *Journal of Geophysical Research (Planets)*, *125*, e06296. https://doi.org/10.1029/2019JE006296

Elkins-Tanton, L. T., Asphaug, E., Bell, J. F., Bierson, C. J., Bills, B. G., Bottke, W. F., et al. (2022). Distinguishing the Origin of Asteroid (16) Psyche. *Space Science Reviews*, *218*(3), 17. https://doi.org/10.1007/s11214-022-00880-9

Evans, A. J., & Tikoo, S. M. (2022). An episodic high-intensity lunar core dynamo. *Nature Astronomy*, *6*(3), 325–330. https://doi.org/10.1038/s41550-021-01574-y

Evans, A. J., Tikoo, S. M., & Andrews-Hanna, J. C. (2018). The Case Against an Early Lunar Dynamo Powered by Core Convection. *Geophysical Research Letters*, *45*(1), 98–107. https://doi.org/10.1002/2017GL075441

Ferguson, J. (1852). Elements of (16) Psyche. *The Astronomical Journal*, *2*, 184–184. https://doi.org/10.1086/100278

Fuller, M., & Cisowski, S. M. (1987). Lunar paleomagnetism. *Geomatik*, *2*, 307–455.

Garcia, R. F., Gagnepain-Beyneix, J., Chevrot, S., & Lognonné, P. (2011). Very preliminary reference Moon model. *Physics of the Earth and Planetary Interiors*, *188*(1), 96–113. https://doi.org/10.1016/j.pepi.2011.06.015

Gattacceca, J., & Rochette, P. (2004). Toward a robust normalized magnetic paleointensity method applied to meteorites. *Earth and Planetary Science Letters*, *227*(3), 377–393. https://doi.org/10.1016/j.epsl.2004.09.013

Ghosh, A., Weidenschilling, S. J., McSween, H. Y., Jr., & Rubin, A. (2006). *Asteroidal Heating and Thermal Stratification of the Asteroidal Belt*. *Meteorites and the Early Solar System II* (p. 555). Retrieved from https://ui.adsabs.harvard.edu/abs/2006mess.book..555G

Gurnette, B. L., & Woolley, R. v. d. R. (1974). *Explanatory supplement to the Astronomical ephemeris and the American ephemeris and nautical almanac* (Third impression with amendments). London: Her Majesty's Stationery Office.

Hardersen, P. S., Gaffey, M. J., & Abell, P. A. (2005). Near-IR spectral evidence for the presence of iron-poor orthopyroxenes on the surfaces of six M-type asteroids. *Icarus*, *175*, 141–158. https://doi.org/10.1016/j.icarus.2004.10.017

Hart, W., Brown, G. M., Collins, S. M., Pich, M. D. S.-S., Fieseler, P., Goebel, D., et al. (2018). Overview of the spacecraft design for the Psyche mission concept. In *2018 IEEE Aerospace Conference* (pp. 1–20). https://doi.org/10.1109/AERO.2018.8396444

Hevey, P. J., & Sanders, I. S. (2006). A model for planetesimal meltdown by $^{26\$}$Al and its implications for meteorite parent bodies. *Meteoritics and Planetary Science*, *41*(1), 95–106. https://doi.org/10.1111/j.1945-5100.2006.tb00195.x

Hinners, N. W. (1971). The new Moon: A view. *Reviews of Geophysics*, *9*(3), 447–522. https://doi.org/10.1029/RG009i003p00447

Hughes, D. W. (2002). Measuring the Moon's mass (125th Anniversary Review). *The Observatory*, *122*, 61.

Jeffreys, H. (1961). On the Figure of the Moon. *Monthly Notices of the Royal Astronomical Society*, *122*(5), 421–432. https://doi.org/10.1093/mnras/122.5.421

Johnson, B. C., Sori, M. M., & Evans, A. J. (2020). Ferrovolcanism on metal worlds and the origin of pallasites. *Nature Astronomy*, *4*(1), 41–44. https://doi.org/10.1038/s41550-019-0885-x

Jung, J., Tikoo, S. M., Gattacceca, J., & Lepaulard, C. (2021). Shock Demagnetization Does Not Fully Explain Variations in the Lunar Paleointensity Record, 2388. Presented at the 52nd Lunar and Planetary Science Conference.

Kim, Y., & Hirabayashi, M. (2022). A Numerical Approach Using a Finite Element Model to Constrain the Possible Interior Layout of (16) Psyche. *The Planetary Science Journal*, *3*(5), 122. https://doi.org/10.3847/PSJ/ac6b39

de Kleer, K., Cambioni, S., & Shepard, M. (2021). The Surface of (16) Psyche from Thermal Emission and Polarization Mapping. *The Planetary Science Journal*, *2*(4), 149. https://doi.org/10.3847/PSJ/ac01ec

Konopliv, A. S., Binder, A. B., Hood, L. L., Kucinskas, A. B., Sjogren, W. L., & Williams, J. G. (1998). Improved Gravity Field of the Moon from Lunar Prospector. *Science*, *281*(5382), 1476–1480. https://doi.org/10.1126/science.281.5382.1476

Kuchynka, P., & Folkner, W. M. (2013). A new approach to determining asteroid masses from planetary range measurements. *Icarus*, *222*(1), 243–253. https://doi.org/10.1016/j.icarus.2012.11.003

Landsman, Z. A., Emery, J. P., Campins, H., Hanuš, J., Lim, L. F., & Cruikshank, D. P. (2018). Asteroid (16) Psyche: Evidence for a silicate regolith from spitzer space telescope spectroscopy. *Icarus*, *304*, 58–73. https://doi.org/10.1016/j.icarus.2017.11.035

Le Bars, M., Wieczorek, M. A., Karatekin, Ö., Cébron, D., & Laneuville, M. (2011). An impact-driven dynamo for the early Moon. *Nature*, *479*(7372), 215–218. https://doi.org/10.1038/nature10565

Libourel, G., Beck, P., Nakamura, A. M., Vernazza, P., Ganino, C., & Michel, P. (2023). V-type Asteroids as the Origin of Mesosiderites. *The Planetary Science Journal*, *4*(7), 123. https://doi.org/10.3847/PSJ/ace114

MacDonald, G. J. F. (1963). The internal constitutions of the inner planets and the moon. *Space Science Reviews*, *2*(4), 473–557. https://doi.org/10.1007/BF00172383

Magri, C., Nolan, M. C., Ostro, S. J., & Giorgini, J. D. (2007). A radar survey of main-belt asteroids: Arecibo observations of 55 objects during 1999–2003. *Icarus*, *186*(1), 126–151. https://doi.org/10.1016/j.icarus.2006.08.018

Marchis, F., Jorda, L., Vernazza, P., Brož, M., Hanuš, J., Ferrais, M., et al. (2021). (216) Kleopatra, a low density critically rotating M-type asteroid. *Astronomy & Astrophysics*, *653*, A57. https://doi.org/10.1051/0004-6361/202140874

Matsuyama, I., Nimmo, F., Keane, J. T., Chan, N. H., Taylor, G. J., Wieczorek, M. A., et al. (2016). GRAIL, LLR, and LOLA constraints on the interior structure of the Moon. *Geophysical Research Letters*, *43*(16), 8365–8375. https://doi.org/10.1002/2016GL069952

Matter, A., Delbo, M., Carry, B., & Ligori, S. (2013). Evidence of a metal-rich surface for the Asteroid (16) Psyche from interferometric observations in the thermal infrared. *Icarus*, *226*(1), 419–427. https://doi.org/10.1016/j.icarus.2013.06.004

McSween Jr., H. Y., Binzel, R. P., De Sanctis, M. C., Ammannito, E., Prettyman, T. H., Beck, A. W., et al. (2013). Dawn; the Vesta–HED connection; and the geologic context for eucrites, diogenites, and howardites. *Meteoritics & Planetary Science*, *48*(11), 2090–2104. https://doi.org/10.1111/maps.12108

Mighani, S., Wang, H., Shuster, D. L., Borlina, C. S., Nichols, C. I. O., & Weiss, B. P. (2020). The end of the lunar dynamo. *Science Advances*, *6*(1), eaax0883. https://doi.org/10.1126/sciadv.aax0883

Mihalov, J. D., Sonett, C. P., Binsack, J. H., & Moutsoulas, M. D. (1971). Possible Fossil Lunar Magnetism Inferred from Satellite Data. *Science*, *171*(3974), 892–895.

Mittlefehldt, D. W., McCoy, T. J., Goodrich, C. A., & Kracher, A. (2018). Chapter 4. NON-CHONDRITIC METEORITES FROM ASTEROIDAL BODIES. In *Chapter 4. NON-CHONDRITIC METEORITES FROM ASTEROIDAL BODIES* (pp. 523–718). De Gruyter. https://doi.org/10.1515/9781501508806-019

Morbidelli, A., Lunine, J. I., O'Brien, D. P., Raymond, S. N., & Walsh, K. J. (2012). Building Terrestrial Planets. *Annual Review of Earth and Planetary Sciences*, *40*(1), 251–275. https://doi.org/10.1146/annurev-earth-042711-105319

Newton, I. (1687). *Philosophiæ naturalis principia mathematica*. London: Royal Society. Retrieved from https://www.loc.gov/item/2021667054/

Nichols-Fleming, F., Evans, A. J., Johnson, B. C., & Sori, M. M. (2022). Porosity Evolution in Metallic Asteroids: Implications for the Origin and Thermal History of Asteroid 16 Psyche. *Journal of Geophysical Research: Planets*, *127*(2), e2021JE007063. https://doi.org/10.1029/2021JE007063

Ockert-Bell, M. E., Clark, B. E., Shepard, M. K., Rivkin, A. S., Binzel, R. P., Thomas, C. A., et al. (2008). Observations of X/M asteroids across multiple wavelengths. *Icarus*, *195*, 206–219. https://doi.org/10.1016/j.icarus.2007.11.006

Ockert-Bell, M. E., Clark, B. E., Shepard, M. K., Isaacs, R. A., Cloutis, E. A., Fornasier, S., & Bus, S. J. (2010). The composition of M-type asteroids: Synthesis of spectroscopic and radar observations. *Icarus*, *210*, 674–692. https://doi.org/10.1016/j.icarus.2010.08.002

Ostro, S. J., Campbell, D. B., & Shapiro, I. I. (1985). Mainbelt Asteroids: Dual-Polarization Radar Observations. *Science*, *229*(4712), 442–446. https://doi.org/10.1126/science.229.4712.442

Pätzold, M., Andert, T. P., Asmar, S. W., Anderson, J. D., Barriot, J.-P., Bird, M. K., et al. (2011). Asteroid 21 Lutetia: Low Mass, High Density. *Science*, *334*(6055), 491–492. https://doi.org/10.1126/science.1209389

Peebles, C. (2000). *Asteroids : a history*. *Asteroids : a history*. Retrieved from https://ui.adsabs.harvard.edu/abs/2000ashi.book.....P

Polanskey, C. A., Elkins-Tanton, L., Jaumann, R., Lawrence, D. J., Marsh, D. M., Moore, R. R., et al. (2018). Psyche Science Operations Concept: Maximize Reuse to Minimize Risk. In *2018 SpaceOps Conference*. American Institute of Aeronautics and Astronautics. https://doi.org/10.2514/6.2018-2703

Runcorn, S. K., Collinson, D. W., O'Reilly, W., Battey, M. H., Stephenson, A., Jones, J. M., et al. (1970). Magnetic properties of Apollo 11 lunar samples. *Geochimica et Cosmochimica Acta Supplement*, *1*, 2369.

Runkle, J. D. (1852). Elements of (16) Psyche. *The Astronomical Journal*, *2*, 166–166. https://doi.org/10.1086/100264

Sanchez, J. A., Reddy, V., Bottke, W. F., Battle, A., Sharkey, B., Kareta, T., et al. (2021). Physical Characterization of Metal-rich Near-Earth Asteroids 6178 (1986 DA) and 2016 ED85. *The Planetary Science Journal*, *2*(5), 205. https://doi.org/10.3847/PSJ/ac235f

Scheinberg, A., Elkins-Tanton, L. T., Schubert, G., & Bercovici, D. (2016). Core solidification and dynamo evolution in a mantle-stripped planetesimal. *Journal of Geophysical Research (Planets)*, *121*, 2–20. https://doi.org/10.1002/2015JE004843

Scheinberg, A., Soderlund, K. M., & Elkins-Tanton, L. T. (2018). A basal magma ocean dynamo to explain the early lunar magnetic field. *Earth and Planetary Science Letters*, *492*, 144–151. https://doi.org/10.1016/j.epsl.2018.04.015

Seidelmann, P. K. (1992). *Explanatory Supplement to the Astronomical Almanac*. *Published by University Science Books*. Retrieved from https://ui.adsabs.harvard.edu/abs/1992esaa.book.....S

Shepard, M. K., Clark, B. E., Nolan, M. C., Howell, E. S., Magri, C., Giorgini, J. D., et al. (2008). A radar survey of M- and X-class asteroids. *Icarus*, *195*(1), 184–205. https://doi.org/10.1016/j.icarus.2007.11.032

Shepard, M. K., Clark, B. E., Ockert-Bell, M., Nolan, M. C., Howell, E. S., Magri, C., et al. (2010). A radar survey of M- and X-class asteroids II. Summary and synthesis. *Icarus*, *208*(1), 221–237. https://doi.org/10.1016/j.icarus.2010.01.017

Shepard, M. K., Taylor, P. A., Nolan, M. C., Howell, E. S., Springmann, A., Giorgini, J. D., et al. (2015). A radar survey of M- and X-class asteroids. III. Insights into their composition, hydration state, & structure. *Icarus*, *245*, 38–55. https://doi.org/10.1016/j.icarus.2014.09.016

Shepard, M. K., Richardson, J., Taylor, P. A., Rodriguez-Ford, L. A., Conrad, A., de Pater, I., et al. (2017). Radar observations and shape model of asteroid 16 Psyche. *Icarus*, *281*, 388–403. https://doi.org/10.1016/j.icarus.2016.08.011

Shepard, M. K., de Kleer, K., Cambioni, S., Taylor, P. A., Virkki, A. K., Rívera-Valentin, E. G., et al. (2021). Asteroid 16 Psyche: Shape, Features, and Global Map. *The Planetary Science Journal*, *2*, 125. https://doi.org/10.3847/PSJ/abfdba

Sierks, H., Lamy, P., Barbieri, C., Koschny, D., Rickman, H., Rodrigo, R., et al. (2011). Images of Asteroid 21 Lutetia: A Remnant Planetesimal from the Early Solar System. *Science*, *334*(6055), 487–490. https://doi.org/10.1126/science.1207325

Siltala, L., & Granvik, M. (2021). Mass and Density of Asteroid (16) Psyche. *The Astrophysical Journal Letters*, *909*(1), L14. https://doi.org/10.3847/2041-8213/abe948

Smyth, J. R., & Mccormick, T. C. (1995). Crystallographic Data for Minerals. In *Mineral Physics & Crystallography* (pp. 1–17). American Geophysical Union (AGU). https://doi.org/10.1029/RF002p0001

Stephenson, A., & Collinson, D. W. (1974). Lunar magnetic field palaeointensities determined by an anhysteretic remanent magnetization method. *Earth and Planetary Science Letters*, *23*(2), 220–228. https://doi.org/10.1016/0012-821X(74)90196-4

Suavet, C., Weiss, B. P., & Grove, T. L. (2014). Controlled-atmosphere thermal demagnetization and paleointensity analyses of extraterrestrial rocks. *Geochemistry, Geophysics, Geosystems*, *15*(7), 2733–2743. https://doi.org/10.1002/2013GC005215

Takahashi, E. (1983). Melting of a Yamato L3 chondorite (Y-74191) up to 30 kbar. *National Institute Polar Research Memoirs*, *30*, 168–180.

Takir, D., Reddy, V., Sanchez, J. A., Shepard, M. K., & Emery, J. P. (2016). DETECTION OF WATER AND/OR HYDROXYL ON ASTEROID (16) Psyche. *The Astronomical Journal*, *153*(1), 31. https://doi.org/10.3847/1538-3881/153/1/31

Tarduno, J. A., Cottrell, R. D., Nimmo, F., Hopkins, J., Voronov, J., Erickson, A., et al. (2012). Evidence for a Dynamo in the Main Group Pallasite Parent Body. *Science*, *338*(6109), 939–942. https://doi.org/10.1126/science.1223932

Tarduno, J. A., Cottrell, R. D., Lawrence, K., Bono, R. K., Huang, W., Johnson, C. L., et al. (2021). Absence of a long-lived lunar paleomagnetosphere. *Science Advances*, *7*(32), eabi7647. https://doi.org/10.1126/sciadv.abi7647

Tholen, D. J. (1984, September). *Asteroid Taxonomy from Cluster Analysis of Photometry.* (PhD Thesis). University of Arizona, Tucson.

Tikoo, S. M., & Evans, A. J. (2022). Dynamos in the Inner Solar System. *Annual Review of Earth and Planetary Sciences*, *50*(1), 99–122. https://doi.org/10.1146/annurev-earth-032320-102418

Toksoz, M. N. (1974). Geophysical Data and the Interior of the Moon. *Annual Review of Earth and Planetary Sciences*, *2*, 151. https://doi.org/10.1146/annurev.ea.02.050174.001055

Turcotte, D. L., & Schubert, G. (2002). Geodynamics - 2nd Edition. *Geodynamics - 2nd Edition, by Donald L. Turcotte and Gerald Schubert, Pp. 472. Cambridge University Press, April 2002. ISBN-10: 0521661862. ISBN-13: 9780521661867. LCCN: QE501 .T83 2002*. https://doi.org/10.2277/0521661862

Urey, H. C. (1957). Boundary conditions for theories of the origin of the solar system. *Physics and Chemistry of the Earth*, *2*, 46–76. https://doi.org/10.1016/0079-1946(57)90006-X

Urey, H. C., & Korff, S. A. (1952). The Planets: Their Origin and Development. *Physics Today*, *5*(8), 12. https://doi.org/10.1063/1.3067687

Viateau, B. (2000). Mass and density of asteroids (16) Psyche and (121) Hermione. *Astronomy and Astrophysics*, *354*, 725–731.

Viikinkoski, M., Vernazza, P., Hanuš, J., Le Coroller, H., Tazhenova, K., Carry, B., et al. (2018). (16) Psyche: A mesosiderite-like asteroid? *Astronomy and Astrophysics*, *619*, L3. https://doi.org/10.1051/0004-6361/201834091

Weber, R. C., Lin, P.-Y., Garnero, E. J., Williams, Q., & Lognonné, P. (2011). Seismic Detection of the Lunar Core. *Science*, *331*(6015), 309–312. https://doi.org/10.1126/science.1199375

Weidenschilling, S. J. (1978). Iron/silicate fractionation and the origin of Mercury. *Icarus*, *35*(1), 99–111. https://doi.org/10.1016/0019-1035(78)90064-7

Weiss, B. P., & Tikoo, S. M. (2014). The lunar dynamo. *Science*, *346*(6214), 1198. https://doi.org/10.1126/science.1246753

Wieczorek, M. A. (2006). The Constitution and Structure of the Lunar Interior. *Reviews in Mineralogy and Geochemistry*, *60*(1), 221–364. https://doi.org/10.2138/rmg.2006.60.3

Williams, J. G., Konopliv, A. S., Boggs, D. H., Park, R. S., Yuan, D.-N., Lemoine, F. G., et al. (2014). Lunar interior properties from the GRAIL mission. *Journal of Geophysical Research: Planets*, *119*(7), 1546–1578. https://doi.org/10.1002/2013JE004559

Yang, J., Goldstein, J. I., & Scott, E. R. D. (2007). Iron meteorite evidence for early formation and catastrophic disruption of protoplanets. *Nature*, *446*(7138), 888–891. https://doi.org/10.1038/nature05735

Yang, J., Goldstein, J. I., & Scott, E. R. D. (2008). Metallographic cooling rates and origin of IVA iron meteorites. *Geochimica et Cosmochimica Acta*, *72*(12), 3043–3061. https://doi.org/10.1016/j.gca.2008.04.009

Yang, J., Goldstein, J. I., & Scott, E. R. D. (2010). Main-group pallasites: Thermal history, relationship to IIIAB irons, and origin. *Geochimica et Cosmochimica Acta*, *74*(15), 4471–4492. https://doi.org/10.1016/j.gca.2010.04.016

Yang, J., Goldstein, J. I., Michael, J. R., Kotula, P. G., & Scott, E. R. D. (2010). Thermal history and origin of the IVB iron meteorites and their parent body. *Geochimica et Cosmochimica Acta*, *74*(15), 4493–4506. https://doi.org/10.1016/j.gca.2010.04.011

Yu, Y. (2010). Paleointensity determination using anhysteretic remanence and saturation isothermal remanence. *Geochemistry, Geophysics, Geosystems*, *11*(2). https://doi.org/10.1029/2009GC002804

Zellner, B., & Gradie, J. (1976). Minor planets and related objects. XX. Polarimetric evidence for the albedos and compositions of 94 asteroids. *The Astronomical Journal*, *81*, 262–280. https://doi.org/10.1086/111882

Zuber, M. T., Smith, D. E., Lehman, D. H., Hoffman, T. L., Asmar, S. W., & Watkins, M. M. (2013). Gravity Recovery and Interior Laboratory (GRAIL): Mapping the Lunar Interior from Crust to Core. *Space Science Reviews*, *178*(1), 3–24. https://doi.org/10.1007/s11214-012-9952-7

Figures

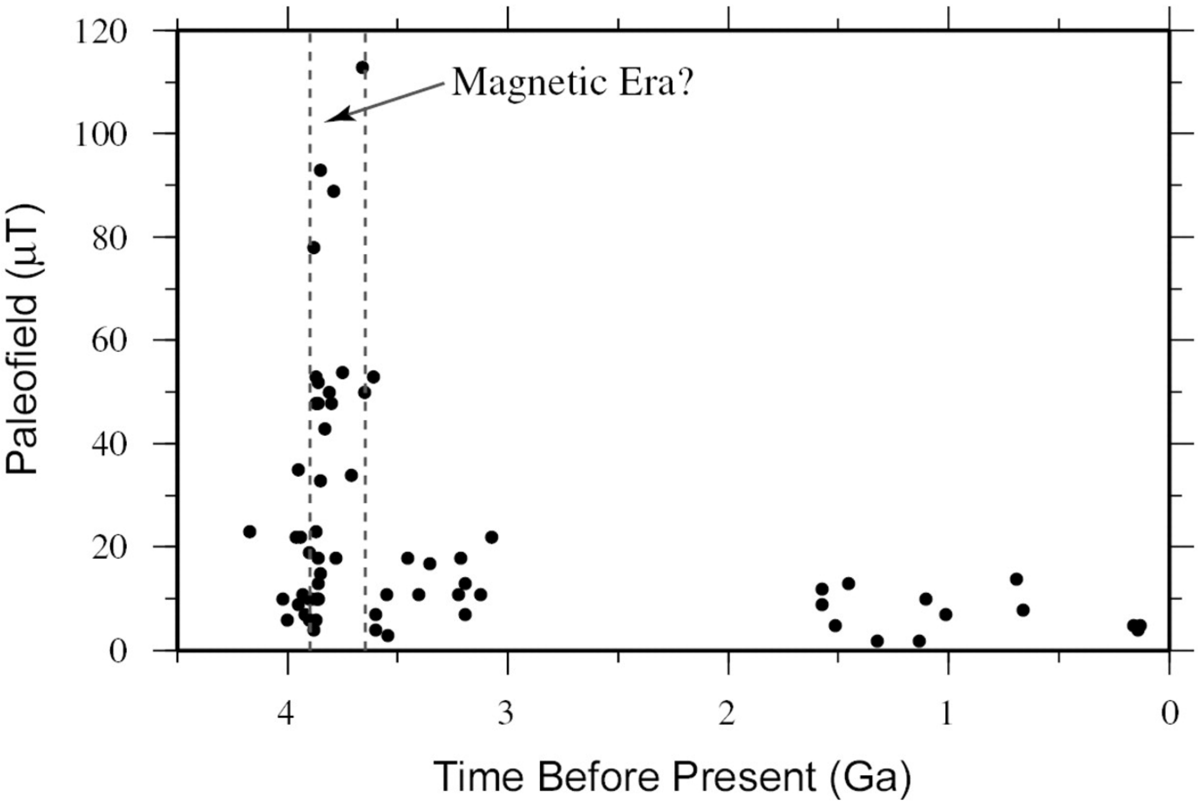

Figure 1. Apollo-era measurements of the lunar paleointensity record. This figure has been reproduced from Wieczorek (2006) and is based on data from Fuller & Cisowski (1987).

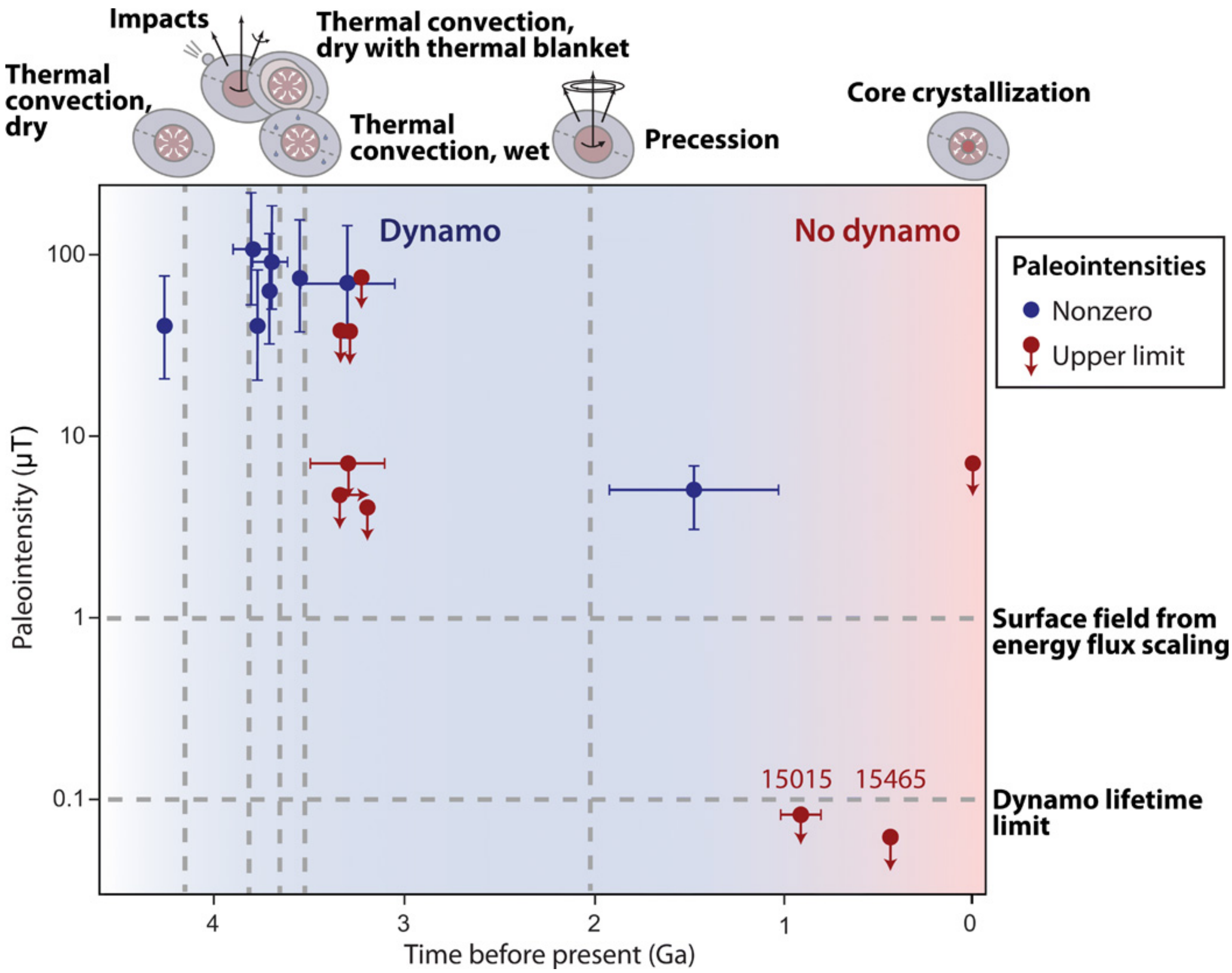

Figure 2. Modern paleointensity measurements from lunar samples. Red points represent upper limits on field intensities while blue points represent detections of a nonzero paleofield intensities.The blue and red shaded regions show the inferred eras in which the lunar dynamo is active or inactive, respectively, and lifetimes in which proposed dynamo mechanisms may be active are shown with vertical dashed lines. This figure is reproduced from Mighani et al. (2020).

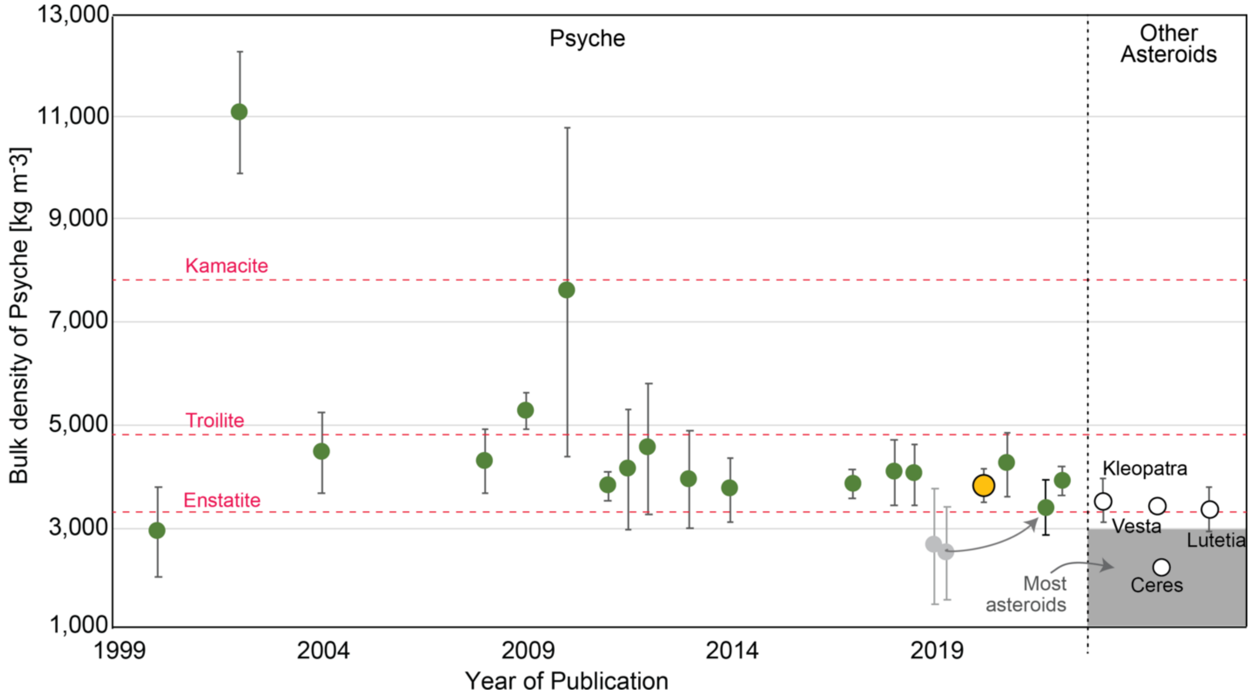

Figure 3. Evolution of the value of Psyche's inferred bulk density as reported over time. The average bulk density of Psyche assumed by the Psyche spacecraft team is shown in the yellow circle ($3{,}780 \pm 340$ kg m^{-3}; Elkins-Tanton et al., 2020) and compiled data from other works are shown as green circles (Elkins-Tanton et al., 2022 and references therein). The gray values have been revised in 2021 to the green circles indicated by the gray arrow (Siltala & Granvik, 2021). For comparison density estimates of several relevant minerals and asteroids are indicated by red dashed lines and white circles, respectively. This figure has been reproduced from Elkins-Tanton et al. (2022).

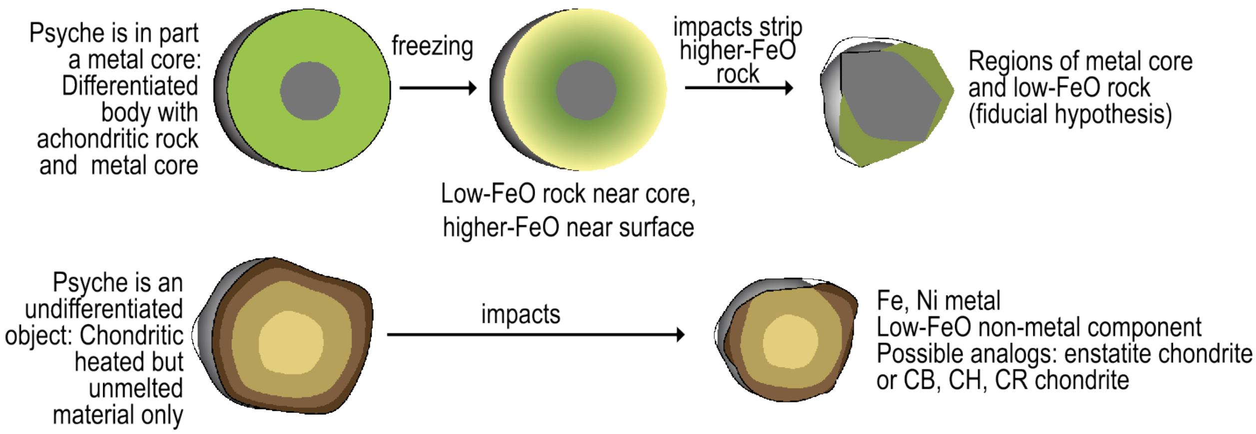

Figure 4. Two formation mechanisms that may be consistent with current observations of asteroid Psyche. This figure has been reproduced from Elkins-Tanton et al. (2022).

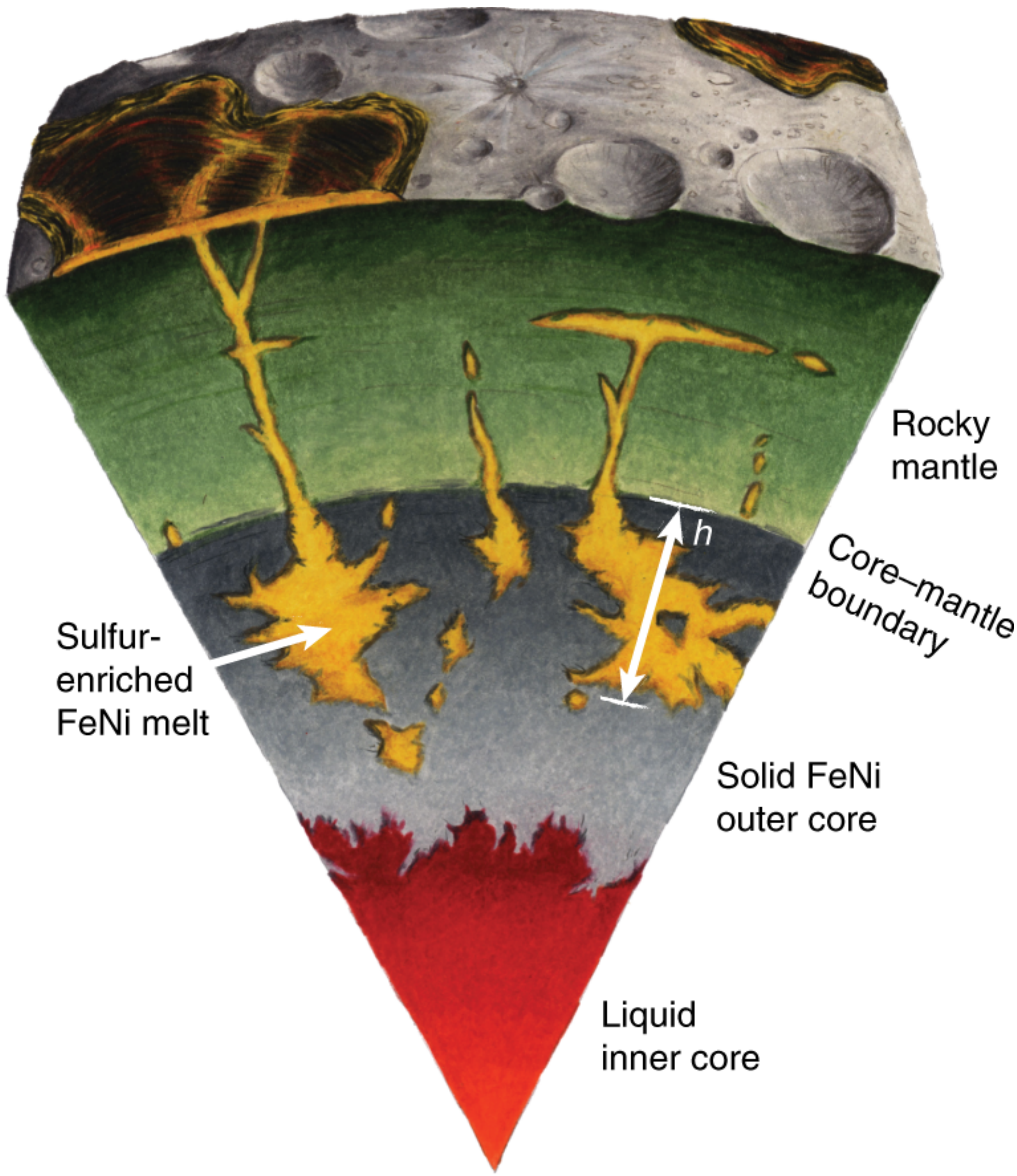

Figure 5. Illustration by James Tuttle Keane illustrating the process of ferrovolcanism on a body with a rocky mantle and a core solidifying dendritically inward. This figure has been reproduced from Johnson et al. (2020).

Chapter 2: The Influence of Cool Impactor Accretion on the Early Lunar Paleomagnetic Record

Fiona Nichols-Fleming[1], Alexander J. Evans[1], Brandon C. Johnson[2,3], and Sonia M. Tikoo[4]

[1]Department of Earth, Environmental and Planetary Sciences, Brown University, Providence, RI

[2]Department of Earth, Atmospheric, and Planetary Sciences, Purdue University, West Lafayette, IN

[3]Department of Physics and Astronomy, Purdue University, West Lafayette, IN

[4]Department of Geophysics, Stanford University, Stanford, CA

Abstract

The recorded lunar magnetic field paleointensities from Apollo samples indicate a period of high intensities ranging from 20 to 120 μT between ~4.3 and ~3.6 Ga Conventional convection models have been unable to replicate the high intensities and variability recorded in this era in addition to the inferred persistence of a subsequent longer-lived, lower intensity paleofield. This could suggest that the early lunar field (prior to 3.6 Ga) may have been sustained by a different dynamo mechanism than what may have operated later. Here we explore the possibility that accretion of cold impactor material can temporarily increase heat flow from the core and produce short-lived, high intensity lunar magnetic fields during the era of lunar basin formation ($\gtrsim$ 3.7 Ga). When conditions are maximized, we find that relatively cold cores of differentiated impactors (diameters $\gtrsim$ 40 km) can reach the hot lunar core-mantle boundary and enhance an existing dynamo enough to produce maximum field strengths of 20 – 97 μT. Additionally, field strengths $\gtrsim$ 40 μT can be supported for a maximum of 21 days – 14 months and moderate enhanced field strengths ($\gtrsim$ 5 μT) can be supported for much longer periods of time, between 40 days and 9,700 years. Overall, the accretion of cool impactor material could theoretically explain high paleointensities from some, but not all, samples from the high intensity era prior to 3.7 Ga and should be considered along with other intermittently high intensity mechanisms for the early history of the lunar dynamo.

Plain Language Summary

About four billion years ago the Moon had a magnetic field that was, at least intermittently, around the same strength as Earth's current magnetic field. This is unexpected because the Moon is much smaller than the Earth and doesn't seem to have enough energy to power such a strong

magnetic field. In this work we investigate impacts as a potential way to enhance the strength of the early lunar magnetic field. We find that the accretion of cool impactor cores could produce brief periods (~21 days – 14 months) of high magnetic field intensities that are similar in value to ancient lunar field strengths inferred from measuring Apollo samples. While it is theoretically possible for surface material to preserve a record of these short-lived fields, a combination of this process with other intermittently high-intensity mechanisms would provide a more complete coverage of the period of high lunar magnetic field intensity.

1 Introduction

The interior structure of the Moon and the existence of a lunar dynamo have been subjects of debate for decades (e.g., Cisowski et al., 1983; Matsuyama et al., 2016; Tarduno et al., 2021; Tikoo & Evans, 2022; Weiss & Tikoo, 2014; Wieczorek, 2006; Wieczorek et al., 2022). For the generation of a core dynamo, a differentiated interior and a partially liquid, convecting core are crucial requirements (e.g., Roberts & Glatzmaier, 2000) and thus understanding the Moon's interior evolution and structure is key to understanding lunar dynamo evolution. Additionally, study of the lunar dynamo itself can provide information about the differentiation state and thermal history of the ancient lunar interior that would otherwise be lost to time. Overall, even under the interpretation that the lunar paleomagnetic record is the result of a dynamo, the exact origin, intensity, and lifetime of that dynamo are highly debated (e.g., Evans et al., 2014, 2018; Evans & Tikoo, 2022; Konrad & Spohn, 1997; Laneuville et al., 2014; Scheinberg et al., 2015, 2018; Stegman et al., 2003; Zhang et al., 2013).

The lunar paleointensity record presents a mystery in the early strength, longevity, and variability of the lunar dynamo. Analyses of returned lunar samples have produced an inferred lunar paleointensity record with two distinct eras. If the Moon generated a long-lived dynamo, paleointensity results suggest there was early dynamo era with high surface field intensities sometimes reaching 20 to 120 μT between at least 4.3 and 3.6 Ga followed by a second era of weak field intensities on the order of a few μT that persisted at least intermittently through ~1.5 Ga (Buz et al., 2015; Cournède et al., 2012; Garrick-Bethell et al., 2009; Garrick-Bethell et al., 2017; Lawrence et al., 2008; Mighani et al., 2020; Nichols et al., 2021; Shea et al., 2012; Strauss et al., 2021; Suavet et al., 2013; Tikoo et al., 2014, 2017; Weiss & Tikoo, 2014). Efforts to infer lunar paleofield intensities from orbital data are also consistent with an early, high field intensity era (Garrick-Bethell & Kelley, 2019; Kelley & Garrick-Bethell, 2020; Wakita et al., 2021). The dynamo is thought to have ceased before 1 Ga (Mighani et al., 2020). Although the significant variability in the measured paleointensities prior to ~3.5 Ga from Apollo-era analysis is met with a level of uncertainty (e.g., Weiss & Tikoo, 2014; Wieczorek, 2006), this variability may reflect true variations in the strength of the lunar dynamo as suggested by Jung et al. (2021) in addition to the inherent factor of $\sim 2-5$ uncertainty associated with the non-thermal paleointensity methods utilized in most lunar paleomagnetic studies (e.g., Gattacceca & Rochette, 2004; Stephenson & Collinson, 1974; Y. Yu, 2010). For example, there exist several measurements of lunar samples that preserved paleointensities indistinguishable from zero between 3.2 – 3.9 Ga, overlapping with the early era of high field intensities (Tarduno et al., 2021). Additional samples older than 3.2 Ga have upper limits on their recorded field intensities of < 10 μT with modern, high-fidelity analysis (Lawrence et al., 2008; Tikoo et al., 2014). These low-to-null intensity samples may indicate true variability of the intensity of the lunar magnetic field. Lunar crustal magnetization detected by the Lunar Prospector and Kaguya missions have provided additional support for a lunar dynamo operating, at least intermittently, into the Imbrian period (Hood, 2011; Hood, Torres, et al., 2021; Hood & Spudis, 2016; Mitchell et al., 2008). Even with a maximized energy budget for the Moon, the >50 μT magnetic field intensities preserved in Apollo samples cannot be supported for longer than 28 Myr by stable core convection (Evans, Tikoo, et al., 2018), much shorter than the ~500 Myr period inferred for the high intensity era. Ultimately, the recorded history of the lunar magnetic field poses a unique problem that long-lived, stable lunar core convection models (e.g., Evans et al., 2014, 2018; Konrad & Spohn, 1997; Laneuville et al., 2014; Scheinberg et al., 2015; Stegman et al., 2003; Zhang et al., 2013) have been unable to reproduce (Evans et al., 2018), potentially indicating the need for unconventional energy sources and mechanisms (e.g., Evans & Tikoo, 2022; Scheinberg et al., 2018).

Alternatives to long-lived, stable core convection have been investigated to determine possible lunar magnetic field evolution scenarios that match the inferred paleointensity record, such as mechanical stirring driven by differential rotation of the mantle and core due to large impacts (Le Bars et al., 2011) and mechanical stirring due to precession at the core-mantle or inner core boundaries (Cébron et al., 2019; Dwyer et al., 2011; Stanley et al., 2017; Stys & Dumberry, 2020). Unlike the field strengths on the order of a few μT that stable core convection models are able to support for billions of years (Evans et al., 2014, 2018; Scheinberg et al., 2015; Stegman et al., 2003), mechanical stirring of the lunar core potentially allows for magnetic fields of up to ~10 μT. However, in each case, early field strengths greater than 40 μT still could not be produced. A non-core mechanism could also be helpful in explaining the early, high intensity magnetic field for portions of the paleomagnetic record. Scheinberg et al. (2018) studied the effects of a basal magma ocean (BMO) on the early lunar dynamo and found that high intensity fields can be produced, however they require an unexpectedly large electrical conductivity for the magma ocean. A BMO will also influence the behavior of an existing lunar core dynamo, and recent work has shown that a coupled BMO-core dynamo can match the timing of the lunar paleomagnetic record and produce field intensities $\lesssim 7\ \mu T$ without any electrical conductivity in the BMO, with possible higher intensities with an electrically conductive BMO (Hamid et al., 2023). Nevertheless, this conductive BMO hypothesis may provide additional energy to power an early lunar dynamo.

Importantly, with few exceptions (e.g., Evans & Tikoo, 2022), the variability of the early paleointensity record is not readily considered within models that attempt to examine the nature of a lunar dynamo. For our work, we consider the possibility that the variability in the lunar paleomagnetic record is reflective of true variability in the field intensity of the early lunar dynamo as suggested by Jung et al. (2021). As the period of lunar history with the most frequent occurrence of large-scale impact events (> 3.7 Ga; Morbidelli et al., 2018) overlaps with some of the high intensity and large variability era of the lunar paleomagnetic record (4.25 – 3.56 Ga; Cournède et al., 2012; Garrick-Bethell et al., 2009; Garrick-Bethell et al., 2017; Shea et al., 2012; Suavet et al., 2013), we examine and determine the influence of impactor material accretion in introducing early, large-scale variability in the lunar interior. Throughout this work we make generous assumptions to allow our model the best chance of success and to constrain the maximum efficacy of impactor material enhancing the lunar magnetic field. In this mechanism, cold, dense impactor material reaches the lunar core-mantle boundary (CMB) causing more vigorous thermochemical convection within the lunar core and therefore producing temporarily higher magnetic field strengths.

2 Theoretical Framework

In this section we outline the theoretical 1-D spherical framework required to determine the maximum influence of impactor material on the ancient lunar dynamo and under which conditions short-lived, high-intensity fields can be sustained. We singularly consider the scenario (see Figure 1), in which material from a differentiated impactor's core sinks through the lunar mantle but remains below the temperature and density of the lunar core. In this scenario, when the relatively cold impactor material reaches the CMB, a period of higher heat flux from the lunar core is sustained. The increased heat flux promotes more vigorous convection within the lunar core, thereby producing greater field intensities for as long as the layer induces an increased CMB heat flux.

If impactor material can sink to the lunar CMB, the accretion of this material may be an efficient mechanism to modify the CMB heat flux and thus the strength of the lunar core dynamo. To produce an enhanced magnetic field (i.e., a magnetic field of higher intensity), impactor material colder than the lunar core must reach the lunar CMB in sufficiently large quantities to increase the average heat flux across the lunar CMB. Additionally, to produce a core dynamo two conditions must be met: (1) the magnetic Reynolds number must be greater than ~ 50, indicating that magnetic induction is more efficient than magnetic diffusion (Christensen & Aubert, 2006), and (2) the heat flux across the CMB must exceed the core adiabatic heat flux. However, here we are interested in investigating the ability of impactor material to enhance an existing lunar dynamo, and therefore both conditions are inherently met.

Impactor material will sink to the lunar CMB if the material is denser than the lunar mantle and gravitational forces dominate over surface tension forces. Furthermore, the mass of impactor material will remain intact if the descent is within the Stokes flow regime. We can approximate the sinking core materials as spheres which is commonly done for the ascent of magma and other processes within solid mantles (e.g. Turcotte & Schubert, 2002). For these spheres, the Bond number $Bo = \frac{\Delta\rho g L^2}{\gamma}$ represents the ratio of gravitational to surface tension forces and materials will be expected to sink for values greater than one. Using surface tension values of $\gamma = 1.735 - 2.16$ N/m, those appropriate for fluid iron at temperatures up to 2,400 K (Fraser et al., 1971), the critical size above which sinking is expected is approximately 3 cm, and thus all core fragments considered in this work will sink through the lunar mantle. Typical lunar mantle reference viscosities range between 10^{18} and 10^{21} Pa s (e.g., Yu et al., 2019), representing those consistent with a weak, hydrated mantle (10^{18} Pa s; Hirth & Kohlstedt, 2003; Yu et al., 2019) up to that of dry peridotite (10^{21} Pa s; e.g., Hirth & Kohlstedt, 2003). The Reynolds numbers associated with these reference viscosities and the densities and radii appropriate for impactor cores are much smaller than one and thus the descent of spheres of impactor material is dominated by viscous forces, also known as the Stokes flow regime (e.g., Lamb, 1945). The Reynolds numbers for the sinking of full impactor cores are between 8×10^{-24} and 5×10^{-15} and for smaller core fragments these values will decrease further. In this regime, deformation on the surface of the sphere will be small even in the absence of surface tension, therefore the impactor core material will not breakup any further post-impact, remaining intact throughout the descent to the lunar CMB. This is discussed in the case of a magma ocean in Samuel (2012), but holds for a higher viscosity, solid mantle as well.

Upon impact, much of the impactor's kinetic energy is converted to internal energy in the impactor and target. Nevertheless, impactor material must also be at a cooler temperature than the early lunar core (1,700 – 2,400 K; Evans et al., 2018; Le Bars et al., 2011) to increase the CMB heat flux and produce increased magnetic field intensities (Roberts & Glatzmaier, 2000).

Therefore, for impactor core material to promote more vigorous convection within the lunar core, the temperature of the impactor core material must be lower than that of the lunar core after considering heat transfer from the impact event and the lunar mantle. Hence, we define our models with respect to the final temperature of the impactor material upon reaching the lunar CMB, subsequently referred to as the emplacement temperature. Using the ANEOS equation of state for iron (Thompson, 1990) and the planar impact approximation (e.g., Melosh, 1989), we convert impact energies to post-impact temperatures and find that the post-impact temperatures for the impactor material remain below 1,700 and 2,400 K when the vertical component of the impact velocity is lower than 7.3 and 8.6 km/s, respectively. We therefore limit vertical impact velocities in this work to $\leq$ 7.3 km/s. This constraint corresponds to approximately 30% of lunar impacts, where the median and maximum simulated vertical impact velocities are 15.9 and ~50 km/s, respectively (Yue et al., 2013). Further discussion of the plausibility of cool emplacement temperatures can be found in Section 5.

In our theoretical scenario, impactor material must remain atop the lunar CMB and therefore must be less dense than the lunar core. Accordingly, we use a maximum impactor core density of 6,193 kg/m^3, which is the best estimate for the density of the lunar core (Matsuyama et al., 2016). This density is lower than that of pure iron and, for our impactors, is assumed to be caused either by the inclusion of a silicate component or ~18 wt% sulfur based on the density and equation of state of Morard et al. (2018). While this is a higher estimated sulfur content than inferred by Apollo seismic velocity measurements (Weber et al., 2011), the two values are consistent within the large errors on the outer core density from Matsuyama et al. (2016). For the full range of plausible lunar core densities ($6{,}193^{+1{,}443}_{-486}$ kg/m^3), required sulfur contents for the impactor cores may range from 0 to 24.5 wt%. As the impactor material increases in temperature, the material will expand and decrease in density by up to 200 kg/m^3. This thermal expansion will aid in the impactor material's buoyancy, further increasing the plausibility of impactor material remaining atop the lunar CMB.

The impact events we consider are limited to those with differentiated impactors as we assume that sinking material is mostly from impactor cores. Therefore, the smallest diameter considered is ~40 kilometers (Hevey & Sanders, 2006) and the largest impactor diameter considered corresponds to the largest known lunar impact basin, South-Pole Aitken (SPA). This range of impactor sizes represent those that could have produced the 29 largest observed lunar basins (Neumann et al., 2015). Using the scaling law from Johnson, et al. (2016b) with an impact angle of 45° and a vertical impact velocity of 7.3 km/s, the maximum allowed impactor diameter is 320 km.

Observed lunar basins provide constraints for impactor sizes, but the influence of the impactor material on the lunar dynamo is controlled by the amount of core material that reaches the lunar CMB. Following Marchi et al. (2018), the impactor size is related to the core size by assuming that 30 wt% of the impactor is in its core. The maximum impactor core and mantle densities of 6,193 kg/m^3 and 3,350 kg/m^3, respectively, along with the constraints on impactor diameters (40 – 320 km) indicate permissible impactor core diameters are between 22 and 180 km. The volumetric fraction of the core that sinks can be expressed with an efficiency factor, f_{sink}. This efficiency factor represents the level of breakup experienced by the impactor core due to the impact event where the sinking sphere is the largest resulting fragment. Based on the hydrocode models of Kendall & Melosh (2016), f_{sink} may be as small as 0.03, however smoothed-particle hydrodynamic models found efficiency factors between 0.2 and 0.9 (Marchi et al., 2018). The exact value will depend highly on impact conditions and we therefore consider sizes generally in terms of the efficiency factor along with specific values of $f_{sink} = 0.03, 0.3,$ and 1.0. It has been hypothesized that the temperature of the lunar nearside crust and mantle is warmer than the farside during the era of basin formation and that this could lead to nearside impact basins that are up to twice as large as those from similar impacts on the farside (Miljković et al., 2013). While this would reduce our allowed sizes of nearside impactors by half and thus reduce their predicted field strengths and lifetimes, the true thermal structure of the lunar nearside during basin formation is unknown and therefore this uncertainty is included in our range of allowed efficiency factors. The allowed diameters of spheres of sinking material are thus $22f_{sink}^{1/3} - 180f_{sink}^{1/3}$ km.

3 Methodology

The behavior of the magnetic field strength is controlled by the heat flux across the lunar CMB and therefore by the emplacement temperature of the impactor core material. For non-convecting impactor core material, we describe this temperature evolution by finding an analytical solution to the one-dimensional, radial heat equation for a spherical shell of uniform composition and emplacement temperature. Calculations of the thermal equilibrium via energy conservation of the impactor material and lunar mantle indicate that the temperature of the lunar mantle would be reduced by less than 0.1% of the initial mantle temperature. Similarly, the thermal equilibrium of the impactor material and lunar core indicate that the lunar core temperature would be reduced by less than 2% of the initial core temperature from a single event. Therefore, the temperature of impactor material atop the lunar core at time *t* after emplacement can be represented by a spherical shell with fixed boundary conditions, such that:

$$T(x,t) = T_{core} - \sum_{n=1}^{\infty} \frac{4\Delta T_0}{(2n-1)\pi} \sin\left[\frac{(2n-1)\pi\, x}{2L}\right] \exp\left[-\alpha\left(\frac{(2n-1)\pi}{2L}\right)^2 t\right] \quad (1)$$

Here, ΔT_0 is the difference between the temperature of emplacement $T(x,0)$ and the lunar core T_{core}, x is the vertical height within the impactor material layer referenced to its base, and L is the thickness of the shell such that the integrated volume of the shell is equivalent to the total volume of foundered impactor core material. Values used for our calculations of enhanced lunar magnetic fields are listed in Table 1.

To determine the evolution of the super-adiabatic CMB heat flux q_{CMB}, we apply Fourier's law to Equation 1 at the CMB ($x = 0$) less the adiabatic heat flux, such that

$$q_{CMB}(t) = \sum_{n=1}^{\infty} \frac{2k\Delta T_0}{L} \exp\left[-\alpha\left(\frac{(2n-1)\pi}{2L}\right)^2 t\right] - q_{ad} \quad (2)$$

where k is the thermal conductivity of iron and q_{ad} is the adiabatic heat flux as defined in Turcotte & Schubert (2002).

The surface magnetic field intensity for the Moon is described by the scaling relation

$$B_s \simeq 2.2 \times 10^{-5} f_{dip} (q_{CMB})^{1/3} \quad (3)$$

(Evans et al., 2018) where $f_{dip} = 1/7$ is the fraction of the lunar field that is dipolar (Christensen et al., 2009) and q_{CMB} is the average super-adiabatic heat flux across the lunar CMB. This scaling law is based on observations of the magnetic fields of planetary bodies and rapidly rotating stars along with fundamental electrodynamical relations (Christensen et al., 2009).

By combining the super-adiabatic CMB heat flux (Equation 2) and the magnetic field scaling law (Equation 3), we find the following expression for surface magnetic field strength:

$$B_s(t) \simeq 2.2 \times 10^{-5} f_{dip} \left(\sum_{n=1}^{\infty} \frac{2k\Delta T_0}{L} \exp\left[-\alpha \left(\frac{(2n-1)\pi}{2L} \right)^2 t \right] - q_{ad} \right)^{1/3} \quad (4)$$

$B_s(t)$ only depends on the impactor size via the thickness of the spherical shell, L, and the temperature difference between the impactor material and lunar core, ΔT_0.

4 Results

The enhanced magnetic field intensities produced by impactor material can affect the lunar paleofield intensity record in two distinct ways. First, early in lunar evolution, the field intensities generated can be as high as those measured in the high-intensity era samples (> 40 μT). Secondly, as the impactor material is heated by the lunar core and the enhanced field intensities decay, there will also be a period in which field strengths are lower than the high-intensity samples, but higher than the weak ($\lesssim$ 5 μT) dynamo inferred for the period after ~3.6 Ga.

4.1 Short-Lived, High Intensity Magnetic Fields

Based on Equation 4 and the generous assumption that the lunar dynamo responds instantaneously to the changed heat flux, the peak magnetic field intensity is attained immediately after emplacement of impactor material atop the lunar CMB. While the core's advective timescale may be more appropriate to estimate the response time of the magnetic field to a change in CMB heat flux, the speed of convection within the Moon's core through time is highly uncertain and an instantaneous response serves as a lower limit to this timescale. Further discussion of this timescale can be found in Section 5.1. Rather than considering the immediate magnetic field strength change upon emplacement of impactor core material, it is more useful to define maximum field strengths at the minimum time surface samples could record intensities. This cooling timescale for mare basalts is between a few hours and a couple days (Shea et al., 2012; Tikoo et al., 2014), therefore we consider the maximum field strengths at two days post-emplacement of impactor material. Within these first two days, only the material closest ($\lesssim$2 m) to the CMB is conductively heated by the underlying core as the conductive timescale for a length of 2 m is ~4.5 days. Therefore, the full shell thickness does not play a significant role in the heat flux out of the lunar core in the first couple days as long as that thickness is greater than 2 m (see Supplemental Figure 2 for an example model of the early thermal evolution of an emplaced layer). Thus, at two days post-emplacement, all impactor sizes considered in this work (for $f_{sink} \gtrsim 0.6$) produce the same field strength for a given temperature difference between the impactor and lunar cores. For smaller efficiency factors, for example $f_{sink} = 0.3$ and 0.03, impactor diameters larger than 60 and 130 km, respectively will produce layers thicker than 2 m and follow this same trend. Hence, the peak magnetic field strengths attained with this mechanism are primarily controlled by the temperature difference between impactor material and the lunar core rather than the impactor size.

The induced magnetic field strength as a function of the temperature difference between emplacement temperature and lunar core temperature is shown in Figure 2. The temperature difference of 1,000 K represents the largest difference between a hot lunar core at ~2,400 K and the coolest temperature at which differentiation of impactors begins, around the onset of silicate melting, at ~1,400 K (Takahashi, 1983). Although it is possible for differentiated impactors to cool significantly and therefore increase this temperature difference by the end of the era when large lunar impacts occurred (~3.7 Ga; Bottke & Norman, 2017), the lunar core may also be at cooler temperatures and thus 1,000 K serves as a conservative upper limit. Figure 2 demonstrates that field strengths greater than 20 μT may be sustainable during the first two days for small initial temperature differences (~10 K cooler than the lunar core) between the core and impactor material. For larger temperature differences between 150 and 1,000 K, maximum field strengths could be as high as 50–97 μT. Hence for temperature differences between the core and impactor material above ~70 K, all differentiated impactors theoretically can produce short-lived fields with strengths between 40 and 100 μT at the two-day-field threshold. Ultimately, our results suggest that even the smallest differentiated impactors (diameters $\gtrsim 40 f_{sink}^{-1/3}$ km) could sufficiently cool the lunar core to induce strong, short-lived fields when conditions are maximized. Therefore, some of the impacts that produced the 29 lunar basins with diameters greater than 385 km (Neumann et al., 2015) could have theoretically produced enhanced dynamo field intensities matching the inferred paleointensities for the period 3.9-3.6 Ga, if their impact velocities were sufficiently slow.

Across the range of impact sizes considered, we also examine the maximum time that enhanced fields can theoretically remain above 40 μT for efficiency factors of $f_{sink} = 0.03, 0.3,$ and 1.0. We determine this timescale by considering the case with the maximum temperature difference between lunar core and emplacement temperature of 1,000 K. The relationship between impactor size and maximum time in the high intensity regime is shown in Figure 3. Panel a shows the general behavior of the time in the high intensity regime where the efficiency factor is left as a variable, while panel b explicitly shows how the length of time in the high intensity regime depends on the efficiency factor for our range of f_{sink} values. For ΔT_0=1000 K and $f_{sink} = 1.0$, all differentiated impactors and therefore the corresponding 29 largest lunar basins can theoretically sustain field intensities above 40 μT for more than 21 days. At lower efficiency factors of 0.3 and 0.03, larger impactor diameters of ~60 and ~135 km, respectively, are required to support these high field for the same amount of time. The time in the high-intensity regime (>40 μT) increases with impactor diameter up to a limit of $100 f_{sink}^{-1/3}$ km, after which all larger impactor diameters have field intensities in the high-intensity regime for 416 days. This and all future limits on impactor diameters are proportional to $f_{sink}^{-1/3}$ because smaller efficiency factors require larger impactor diameters to allow for the same volume of impactor core material to reach the lunar CMB. Equivalently, assuming a full impactor core reaches the lunar CMB ($f_{sink} = 1$), all basin diameters larger than ~865 km could theoretically support magnetic field intensities above 40 uT for 416 days. Similar to the thermal evolution of the layers of impactor material within the first two days post-emplacement, after 416 days the material more than ~ 37 m above the CMB has not been heated. Therefore, layers thicker than 37 m have the same behavior within the first 416 days and their maximum time above 40 μT becomes constant. The largest eight lunar basins, those with diameters greater than 865 km

(Neumann et al., 2015) and ages spanning 3.7 to ≳4.3 Ga (Bottke & Norman, 2017; Evans et al., 2018), therefore could all theoretically produce enhanced magnetic field intensities for 14 months if full impactor cores are able to reach the lunar CMB and associated impact velocities were sufficiently low. If we maximize the energy available to the lunar dynamo from the impactor material by assuming each impactor core fully sinks and remains 1,000 K cooler than the lunar core, the maximum total aggregated time the 29 largest lunar basins could have enhanced field strengths in the high intensity regime is ~18 years. If we only consider ~30% of these 29 impacts to represent the expected fraction of impacts with vertical impact velocities below 7.3 km/s (Yue et al., 2013), this aggregated time in the high intensity regime may only be ~6 years. Additionally, if we assume our lower limit on the efficiency factor of $f_{sink} = 0.03$, this time could be further reduced to only $\sim 4 - 5$ weeks.

4.2 Moderate Intensity Magnetic Fields

After the magnetic field intensities drop below 40 μT, there is a longer timescale across which moderate field intensities (5 – 40 μT) may still be possible. The time above 5, 10, 20, and 30 μT for impactors with the maximum temperature difference of 1,000 K are shown in Figure 4. Below 20 μT, timescales increase with impactor size because larger impactors require increasingly more energy to reach thermal equilibrium with the lunar core and therefore can drive high CMB heat fluxes for longer periods of time. However, for field intensities above 20 μT, timescales increase with increasing impactor size but eventually plateau. For field intensities of 20 and 30 μT and efficiency factors $f_{sink} = 1$, these timescales plateau at ~83 and 7.2 years, corresponding to impactor diameters of 200 and 130 km, respectively. For the lower efficiency factors of 0.3 and 0.03 (see Supplemental Figure 3), these plateau diameters become 298 and 195 km and 644 and 418 km, respectively. The large, required size of impactors in the lowest efficiency factor case means that, if this is truly the expected core fragment size, known impactor sizes are smaller than required to reach this plateau and the maximum timescale known impactor events could enhance field strengths above 20 and 30 μT are ~5.5 and ~2 years, respectively. The field intensities associated with our smallest differentiated impactor decays rapidly and drops below 5 μT in ~2 months for efficiency factors of $f_{sink} = 1$. For smaller core fragments ($f_{sink} = 0.03$), impactors below ~80 km only sustain field strengths above 5 μT for a few days. Our largest impactors ($\gtrsim 135 f_{sink}^{-1/3}$ km in diameter), however, can support moderate field intensities (5 – 30 μT) for a wider range of timescales (~7 – 9,700 years for $f_{sink} = 1$). For $f_{sink} = 0.03$, this scale of impactor sizes in not known to exist based on observed lunar basins, and the maximum allowed impactor size can support these moderate field intensities for a smaller range of timescales from ~3 – 10 years.

We illustrate the progression of these fields by comparing the temporal evolution of field strength for impactor sizes appropriate to those which formed the Korolev, Orientale, Imbrium, and SPA basins. For this comparison, we use the maximum temperature difference between the impactor material and the lunar core (1,000 K) and assume $f_{sink} = 1$ (Figure 5). Impactor sizes for these events were determined with basin diameters from Neumann et al. (2015) and the basin scaling law of Johnson, et al. (2016b) assuming an impact angle of 45° and a vertical impact velocity of 7.3 km/s. The resulting impactor diameters for these four basins are 44, 110, 160, and 320 km, respectively, which correspond to core diameters of 12, 31, 45, and 90 km, respectively. Figure 5 illustrates that high field strengths (> 40 μT) can be supported for between 21 days and 14 months for this range of impactor sizes. With the exception of the Korelev impactor, whose field decays the quickest, the generated field intensities for varying impactor sizes diverge after the fields drop below 40 μT. As the impactor cores shown in Figure 5 all begin with the same temperature difference between impactor and lunar core material, this behavior illustrates that the size of the impactor is the dominant factor in the overall lifetime of the field. Changes in temperature will also influence the lifetime of the enhanced field, but to a lesser extent than impactor size. Importantly, field strengths above a few μT can be supported for hundreds to thousands of years for the largest known lunar impactors and maximized core fragment sizes, with the SPA impactor producing an enhanced field for 9,700 years. For efficiency factors of $f_{sink} = 0.3$ and 0.03, surface field strengths decay more rapidly (see Supplemental Figure 4) with the SPA impactor producing an enhanced field for ~200 and 30 years, respectively. In both cases, the Orientale, Imbrium, and SPA basins are expected to have associated enhanced surface field strengths in the high intensity regime (> 40 μT), but the Korolev basin only has enough core material reach the lunar CMB to produce high intensity fields for efficiency factors $f_{sink} \gtrsim 0.25$ and moderate intensity, enhanced fields (> 5 μT) for efficiency factors $f_{sink} \gtrsim 0.13$.

The results of this work are dependent on the choices of both core density and efficiency factor since both values determine the volume of impactor core material that reaches the lunar CMB. There are large error bars on the derived lunar core density (Matsuyama et al., 2016) with the one sigma error range between 5,707 and 7,636 kg/m^3. For this range of core densities, the volume of the impactor cores changes by ~5 – 10% when maintaining a ratio of 30 to 70 wt% in the impactor core and mantle, respectively. Similarly, as discussed throughout the results section, smaller efficiency factors can greatly reduce the amount of time for which enhanced field strengths can be supported. However, values for the efficiency factor depend on the viscosity of the lunar mantle and impact conditions and are not currently well constrained by models. In the cases of both core density and efficiency factor, the changes to the volume of impactor material at the CMB will modify the decay rate of the enhanced magnetic fields with smaller volumes decaying faster than the presented results and larger volumes decaying slower (see Supplemental Figure 5). Maximum field strengths are not affected as long as the shell of impactor material atop the lunar CMB remains thicker than 2 m, the thickness of material that is heated within the first few days.

5 Discussion

Our results demonstrate that the lunar dynamo could have been enhanced by emplacement of cool impactor material atop the CMB. Per Figure 5, it is shown that not only can the enhanced magnetic fields associated with the foundering of differentiated impactors of any size reach high intensities early in the evolution of their associated magnetic fields, but the enhanced fields from the largest scale impact events can remain at moderate surface intensities for up to thousands of years. Moreover, the enhanced fields, both of moderate (5 – 40 μT) and high intensities (≥ 40 μT), are consistent with those fields preserved within the early lunar paleointensity record under the assumption that these samples record dynamo activity. While our mechanism for producing enhanced fields is similar to that of Evans & Tikoo (2022), the volume of impactor cores is much smaller than the volume of Ti-rich cumulates they consider. Thus, the maximum length of time over which known lunar impactor events could produce high surface field strengths (≥ 40 μT for 18 years) is much smaller than the 400 kyr over which the Ti-rich cumulates could produce strengths > 50 μT (Evans & Tikoo, 2022). Nevertheless, the theoretical framework upon which this work relies invokes simplifying assumptions that likely impact both the duration and the intensity of the enhanced fields discussed in Section 4. Below, we examine the effect of these assumptions on our results.

5.1 Key Assumptions of the Model

We have previously presumed that impactor core emplacement temperatures could be cooler than the lunar core temperature. To better understand why impactor material reaching the CMB with a temperature cooler than the lunar core is feasible, we consider two endmember thermal cases: (1) a low viscosity lunar mantle where the only significant heating is from the impact, and (2) a high viscosity lunar mantle where impact heating is lost to the mantle. In both cases, the difference in the temperature of impactor material is due to the difference in the speed of descent through the mantle relative to the conductive timescale of the sphere of impactor material (see Supplement for details). If little heat is exchanged between impactor material and the lunar mantle, as in the first case where sinking times ranging between 5.8 and $370 f_{sink}^{-2/3}$ kyrs are lower than the conductive timescale, the heating of impactor material can be constrained based on the impactor energy (i.e., impact velocity). As mentioned in Section 2, post-impact temperatures for the impactor material remain below 1,700 and 2,400 K when the vertical component of the impact velocity is lower than 7.3 and 8.6 km/s, respectively. These impact velocities correspond to approximately 29 and 39% of all lunar impacts, respectively (Yue et al., 2013). For high lunar mantle viscosities ($\gtrsim 10^{20}$ Pa s), sinking velocities are sufficiently low such that sinking times are up to 5.8 – $370 f_{sink}^{-2/3}$ Myrs, much longer than the conductive timescale, and thus the impactor material is in thermal equilibrium with the lunar mantle. If the lunar mantle is convecting during the descent of impactor material, the mantle temperature structure can be approximated as a thin thermal boundary layer (TBL) above the CMB where the temperature transitions between that of the core and the nearly isothermal central region of the convective cell. In the case where the full mantle is convecting, the sinking impactor material is expected to have the same temperature as the isothermal central region, which by symmetry must be the average of the temperature at the base of the crust and the temperature of the core (Turcotte & Schubert, 2002). Therefore, as the impactor material reaches the lunar CMB, it would displace the TBL material and the resulting temperature difference at the CMB would be greater than zero. If we assume the base of the lunar crust is ~1,100 K and the lunar core is ~1,700 K, then the impactor material in thermal equilibrium with the isothermal central region would have an emplacement temperature of ~1,400 K and could produce a maximum enhanced field strength of ~60 μT. This shows that temperature differences between impactor material and the lunar core would be expected for any impact conditions if the lunar mantle has a high viscosity. For the moderate allowed lunar mantle reference viscosities, both impact velocity and heat transfer with the mantle will matter, although higher vertical impact velocities will be allowed as some of the heat could be lost to the lunar mantle. Additionally, in cases where convection occurs within the sphere of impactor material itself, the timescale required to reach thermal equilibrium with the isothermal central region will be reduced and thus even more heat from high impact velocities could be lost to the lunar mantle. However, if a partial melt layer or a basal magma ocean exists above the lunar core with a viscosity $\lesssim 10^{13}$ Pa s, the descent of the impactor core material will change flow regimes and breakup will occur on a timescale much smaller than the time to reach the CMB (Samuel, 2012). In this case the impactor core material will not be able to produce a change in the lunar dynamo strength for any impact or mantle conditions.

Additionally, our model treats the response of the magnetic field to the change in CMB heat flux due to the impact material as instantaneous. However, the true response time is not well known and may instead be on the order of the advective timescale of the core, in which case the maximum recordable field strengths from this mechanism could be greatly reduced. Convective velocities vary with field strength, rotation rate, and material properties of the core approximately via the scaling law from Davidson (2013). We couple the velocity calculations to our model of CMB heat flux and determine appropriate advective timescales. To accurately capture the variation of lunar rotation rates appropriate for ancient Earth-Moon separations of ~20 – 40 Earth radii (Le Bars et al., 2011; Zahnle et al., 2015), we consider rotation periods of 4 and 24 days. These rotation periods produce advective timescales of 77 – 140 days and 28 – 50 days for impactors with emplacement temperatures 100 and 1,000 K cooler than the lunar core, respectively. These timescales assume that the entire lunar core is convecting, and therefore convection solely within an outer (liquid) lunar core would lead to even shorter advective timescales and the uncertainty of the size of the fluid portion of the core at any given time makes the determination of this timescale more challenging. Additional uncertainties in core properties could further decrease the advective timescales and allowing an instantaneous response in our models serves as an absolute lower limit to this timescale. Future dynamo simulations will be crucial for accurately determining the true response timescale of the lunar dynamo to a change in CMB heat flux. Nevertheless, after 28 days, high intensity fields are still likely for impactor diameters larger than ~$55f_{sink}^{-1/3}$ km (see Figure 6a). For impactor diameters $\gtrsim 55f_{sink}^{-1/3}$ km, the field intensities at 28 days post-emplacement are not sensitive to impactor diameter and are solely determined by the temperature difference between impactor and lunar core material. Maximum field intensities up to 65 μT are possible for emplacement temperatures 1,000 K cooler than the lunar core if the response time of the magnetic field is 28 days. After the longer advective timescale of 140 days, maximum field strengths up to 50 μT are possible for impactor diameters larger than $60f_{sink}^{-1/3}$ km (see Figure 6b). Overall, although field strengths may not reach 90 μT when the magnetic field's response is on the order of the advective timescale, field strengths within the high intensity regime (≥ 40 μT) are still possible for impactor diameters larger than $\sim 55 - 65 f_{sink}^{-1/3}$ km when emplacement temperatures remain 300 – 600 K cooler than the lunar core. As the lunar core cools, these large differences between emplacement and lunar core temperatures and therefore the high-intensity field strengths, will become more plausible. Additionally, a delayed response of the lunar dynamo to the emplacement of impactor material will increase the variability of the maximum field strengths, in particular for impactors smaller than $\sim 55 - 65 f_{sink}^{-1/3}$ km in diameter. If a delay in the response of the lunar dynamo instead spreads the change in CMB heat flux such that the recorded surface field strength is due to an average heat flux across that timescale, higher field strengths than those shown in Figure 6 will be expected. In the maximized case where efficiency factors $f_{sink} = 1$ and the temperature difference between impactor core and lunar core material are 1,000 K, high intensity field strengths (≥ 40 μT) are expected for delay timescales of up to 8 – 15 years for the impactor sizes considered here. In this case, a delay on the order of the advective timescale less than 8 years would not prevent any high intensity field strengths.

5.2 Beyond Our Theoretical Framework

The scaling law for magnetic field strength used in this work requires an average heat flux across the CMB (Christensen et al., 2009) and to maximize the heat flux increase we have required impactor material to spread uniformly across the CMB. However, the impactor material takes time to spread laterally, and therefore a more realistic scenario may result in an asymmetric distribution of impactor material. We approximate the time required for impactor cores to form a uniform layer with the following equation modified from Huppert (1982) by Evans & Tikoo (2022).

$$t_s \sim \frac{3\pi^8 R_C^8 \eta \rho_m}{\Delta\rho g_{CMB} V^3} \tag{5}$$

where η is the viscosity of the impactor core material, R_C is the lunar core radius, V is the volume of impactor core material, and g_{CMB} is the gravitational acceleration at the lunar CMB. Spreading times are ~30 Myr for the largest core fragments at the lowest solid viscosities ($\eta \sim 10^{12} - 10^{16}$ Pa s) and quickly reach times much greater than the age of the universe as viscosity is increased or impactor core volume is decreased. However, upon melting of ~40 vol% of the impactor material, the viscosities decrease significantly to $\lesssim 10^4$ Pa s (Dufek & Bergantz, 2005), and thus spreading times decrease dramatically as well. For the range of impactor sizes considered in this work, spreading times after reaching 40 vol% melt are between 0.3 years and 40 Myr, with times below 1 year for core fragments with radii larger than 40 km. The large spreading times for small impactor core fragments relative to the enhanced field lifetimes (40 days – 9,700 years) suggest that there will be some cases in which an asymmetric layer of impactor material does not spread uniformly at the CMB, which could change the evolution of magnetic field intensity with time. For the larger impactor sizes that can spread laterally after melting, the CMB heat flux prior to melting will still be affected by the asymmetric distribution of material. Generally, for an impactor of a constant size and emplacement temperature, an asymmetric distribution would result in a lower increase in average heat flux across the lunar CMB as well as a thicker layer of impactor material than the uniform case. In this situation, the asymmetric layer would produce a field with a lower initial intensity, but a longer lifetime as a thicker layer would take longer to heat. Additionally, it is thought that the subduction of cold slabs to the Earth's CMB could trigger rapid magnetic reversals that would manifest as a decrease in average paleointensity rather than an enhanced field strength (e.g., Biggin et al., 2012; Hounslow et al., 2018), and a similar behavior may be expected from an asymmetric distribution of impactor material on the lunar CMB. Alternatively, an asymmetric distribution of material on the lunar CMB could also produce localized high paleointensities even greater than those calculated in this work as seen in three dimensional dynamo models for the Earth (Glatzmaier et al., 1999). Given that there is uncertainty about whether an asymmetric CMB heat flux will increase or decrease local field intensities and here we are investigating the response of the global field to the accretion of impactor material, further consideration of the effects of an asymmetric distribution of impactor material is left to future work.

It is also possible that an impactor core could break into multiple fragments during the impact event. These smaller fragments of impactor core material will sink through the lunar mantle as described in Sections 2 and 3. If the fragments are different sizes, they will reach the lunar CMB at different times with smaller fragments taking longer timescales to sink. Individually, the divided impactor core fragments will support enhanced magnetic fields for shorter timescales. However, the delay between fragments reaching the lunar CMB could prolong the time in which the lunar dynamo is enhanced by a particular impact. Furthermore, a scenario in which one impact could produce multiple periods of enhanced magnetic field strength would lead to another source of variability in the early lunar paleointensity record.

Additionally, any mixing of the lunar and impactor core material has not been included in our models as we aim to understand the maximum influence of impactor material on the lunar dynamo. When the impactor core material is heated up by the lunar core, light elements will melt first and result in an increased density for the layer of impactor material. Once this density is larger than that of the lunar core, the impactor material will sink into and mix with the lunar core. This partial melting will begin at the FeS eutectic temperature of ~1300 K and continue up to the liquidus at ~1800 – 2000 K, depending on the sulfur content of the impactor core (Buono & Walker, 2011). We do not expect this to affect our high intensity results because the early stages of the enhanced magnetic field are controlled by the thermal evolution of the lowest portion of the impactor melt. At these times, only a small fraction of the impactor material has been heated and therefore there can only be a minor change in density. However, this density change is a more important consideration for the moderate field strengths where the full layer of impactor material has been conductively heated. Detailed modeling of this process is left to future work as there is not currently a tight constraint on lunar core density or sulfur content of impactor core material, but in general we overestimate moderate field lifetimes by ignoring this process.

Upon melting of the layer of impactor core material, convection will likely become the dominant mode of heat transport within the layer of impactor core material since the Rayleigh number will become much greater than 1,000 at low viscosities. At this time, the super-adiabatic CMB heat flux will increase and therefore surface field strengths will increase as well. This is because convection transports heat faster than conduction in systems with large Rayleigh numbers. However, an additional result of this fast transport of heat, the impactor material will be heated to the lunar core temperature in a shorter period of time, and therefore the lifetimes of these short-lived enhanced fields will be reduced. This additional consideration is unlikely to affect the maximum intensities caused by foundering impactor material because the timescale for melting the full layer of impactor material is longer than the two-day threshold for the maximum intensities. Convection within the impactor core material instead will likely produce an instantaneous increase in surface field intensity at the onset of convection and reduce the overall lifetime of the enhanced field. Ignoring the effects of convection within the impactor material therefore leads to an overestimate of moderate field lifetimes.

5.3 The Surface Record of Enhanced Fields

An important factor for understanding the influence of impactor core accretion on the lunar magnetic field is whether there could be material on the Moon's surface cooling through its Curie temperature at the right time to record the enhanced field strengths. Additionally, the rapid variations in field strength must not be shielded from rocks on the surface by the lunar mantle. Electrical conductivity of Earth’s mantle has been hypothesized to shield field strength changes that occur on timescales below a few months (Jault, 2015), however this shielding timescale is expected to be much lower for the lunar mantle due to its lower electrical conductivity (e.g., Figure 7 of Khan et al., 2014) and the Moon’s smaller size and thus should not interfere with the high intensities and variability seen in this work. As discussed in detail in the Supplement, the sinking times for impactor material in this work vary significantly with both impactor size and lunar mantle viscosity and, for an efficiency factor $f_{sink} = 1$, were between 5 kyrs and 370 Myrs. Most antipodal impact ejecta is expected to have arrival times within a few days (Hood & Artemieva, 2008; Wakita et al., 2021). Melted ejecta would be made up of small particles that would cool through their Curie temperature much too quickly to record any enhanced field strengths at the antipode expected from impactor material at the lunar CMB. However, larger solid ejecta will take longer to cool and can therefore reach the antipode at temperatures above the Curie temperature (Wakita et al., 2021). Using ~700 m as the representative thickness of an antipodal ejecta deposit following Wakita et al. (2021), the conductive timescale of the deposit is

~15 kyr and therefore regions of the ejecta may be able to record the enhanced fields in the case of lower lunar mantle viscosities.

In addition to ejecta, basin size impacts can also produce large volumes of melt within their basins (Abramov et al., 2012; Cintala & Grieve, 1998; Collins et al., 2002; Grieve & Cintala, 1992; Ivanov, 2005; Vaughan et al., 2013) which could take long periods of time to fully cool due to their expected differentiation (Grieve et al., 1991; Vaughan et al., 2013). For the basin-sized impact events considered in this work, melt pools are expected to have depths on the order of 10 km (Cintala & Grieve, 1998; Vaughan et al., 2013) resulting in solidification timescales on the order of 100 kyrs (Vaughan et al., 2013). For lower lunar mantle viscosities (10^{18} Pa s), the time for the material to reach the CMB is shorter than or on the same order as this solidification timescale (5.8 – $370 f_{sink}^{-2/3}$ kyrs) and therefore portions of the melt sheet may cool through their Curie temperature at the right time to record these short-lived fields. However, the melt sheets would not be expected to provide a pervasive record of the transient fields. Furthermore, the cooling rates of melt sheets that contain the iron-nickel minerals kamacite and martensite are complicated by their initial fraction of melt, with cold clasts reducing the cooling timescale (Onorato et al., 1978), and their magnetic recording temperatures can vary with nickel content, with the magnetic recording temperature decreasing with increasing nickel content (e.g., Swartzendruber et al., 1991). Thus, there is further uncertainty in their ability to record short-lived changes in magnetic field intensity. For higher lunar mantle viscosities, the impactor material would reach the CMB after the solidification of its associated melt sheet and cooling of its ejecta and therefore samples able to record the short-lived field would need to be unrelated to the impact event. Assuming the low lunar mantle viscosity of 10^{18} Pa s, impactor diameters $\gtrsim 80 f_{sink}^{-1/3}$ km have sinking and dynamo delay times less than 100 kyr and thus, portions of their associated impact melt sheets could theoretically record the enhanced field strengths due to the accretion of impactor core material. One alternative process that would be able to produce surface materials above their Curie temperatures is ongoing lunar volcanism. Mare basalts are widespread across the lunar surface, primarily on the lunar nearside (e.g., Head, 1976), and their modeled ages suggest that volcanism was active from ~4 to ~1.2 Ga (Hiesinger et al., 2003, 2011). The cooling of these basalts in the early era of lunar volcanic activity could record the short-lived fields produced by our mechanism if an eruption occurs within the time an enhanced dynamo is operating.

The theoretical ability of these fields to be recorded in slow cooling melt sheets and some mare basalts in addition to their short-lived nature could help explain the variability observed in samples from the early lunar paleointensity record. Recent work has found two localized magnetic anomalies with unique paleopole orientations within the Crisium basin (Baek et al., 2019). While this presents a challenge for many lunar dynamo models, the modification of an existing lunar dynamo by accretion of impactor material could lead to a change in paleopole orientation and intensity during the cooling period of a single melt sheet. Additionally, there exists significant and as yet unexplained variability in the presence of central magnetic anomalies for basins of similar ages and sizes across the lunar surface where 18 of 25, or 72% of the impact basins that have ages upper preNectarian and younger have mapped internal anomalies (e.g. Hood, 2011; Hood et al., 2014; Hood, Oliveira, et al., 2021; Hood & Spudis, 2016). Five of these basins, or 20%, have the most confident observations of central anomalies that originated at the times of basin formation (Hood, Oliveira, et al., 2021). Variability in the early lunar dynamo intensity due to the accretion of impactor cores could be an important factor in explaining which lunar basins have central anomalies. This variability is increased when the allowed impact conditions (e.g., impact angle and velocity) are considered, limiting the fraction of impact events that could influence the dynamo to ~30 – 40%. The exact relationship between a lunar dynamo enhanced by impactor core material and central magnetic anomalies in lunar basins is further complicated by the exact way in which the impactor core material is split between the ejecta, the melt sheet, and the sinking portion, and therefore, determining this relationship is beyond the scope of this work.

The influence of impactor material on the lunar core dynamo is likely to have been limited to the period in which large basins formed on the Moon. Based on the age of Orientale, the youngest of large lunar basins (Wilhelms et al., 1987), the latest time for which the accretion of impactor material could enhance the lunar magnetic field is likely ~3.7 Ga (Bottke & Norman, 2017). Since the foundering of impactor material is not possible for the full length of the high-intensity era, the influence of impactors would only be able to explain a subset of the high intensity samples from early lunar history. If impactors do indeed play a role in the lunar paleomagnetic record, we would expect to find samples with variable magnetic field intensities within the era prior to 3.7 Ga. The Apollo-era analysis of lunar samples showed a large spread in measured paleointensities within this high-intensity era (e.g., Weiss & Tikoo, 2014; Wieczorek, 2006) which could support the idea of high field strengths being caused by short-lived fields. Although this spread is seen in Apollo-era analysis and recent work has shown this could be due to true variations of the lunar dynamo (Jung et al., 2021), the higher fidelity modern analysis of more lunar samples from this period could serve to strengthen the evidence for this variability and any analysis resulting in low or zero measured field strengths will be as important as those with high field intensities. Since impacts are a pervasive process throughout the inner Solar System, we could expect a similar process to occur on other bodies as well. Any signatures of impact related magnetic fields in the paleointensity records of the Moon or other inner Solar System bodies could be used to inform the bombardment history of the early Solar System.

6 Conclusions

Previous models of long-lived, stable core convection processes have been unable to individually reproduce the longevity and high intensities of the lunar magnetic paleointensity record prior to 3.7 Ga, making a separate mechanism for producing early high field intensities an enticing prospect (Weiss & Tikoo, 2014). In this work, we evaluate a new mechanism for producing short-lived magnetic fields via accretion of cool impactor material and determine its maximum efficacy. We find that the smallest expected differentiated impactors can produce dynamo intensities on the order of those measured within the high intensity era for long enough timescales to potentially be recorded by samples on the surface when the conditions are maximized. Although these high field strengths decay quickly, field strengths above the magnitude of the long-lived lunar field ($\gtrsim 5$ μT) can be supported for up to 9,700 years.

From the models of magnetic field evolution contained in this work, we make the following conclusions:

- The maximum possible field strengths that could be produced by the accretion of cold impactor core material are solely dependent on emplacement temperature and range between 20 and 97 μT. If we include a dynamo response time equivalent to an advective timescale of 28 – 140 days, the corresponding maximum field strength would be ~20 – 65 μT.

- To have maximum field strengths in the high intensity regime (> 40 μT), emplacement temperatures must remain at least 70 K cooler than the lunar core.
- Emplacement temperatures depend on the impact conditions and the sinking velocity of the impactor material. Conservatively, to ensure emplacement temperatures below the temperature of the lunar core, vertical impact velocities must remain below 7.3 km/s, approximately 29% of all lunar impacts.
- Even the smallest differentiated impactors could support a field intensity > 40 μT for 21 days. The largest basins can produce field intensities > 40 μT for 14 months. Additionally, the maximum time differentiated impactors can have moderate field strengths (> 5 μT) are between 40 days and 9,700 years.
- Slow cooling impact melt sheets that are produced by impactor diameters $\gtrsim 80 f_{sink}^{-1/3}$ km could record the enhancement of the lunar dynamo caused by the accretion of their impactor's core material.
- Generally, our theoretical framework overestimates the lifetimes of the enhanced fields due to our assumption of conduction within the impactor material and lack of mixing between the impactor and lunar core materials. Thus, these models can provide upper limits for the influence of impactor material accretion on the early lunar dynamo.

The conclusions above suggest that some large impacts may have a detectable signature in the lunar paleomagnetic record before 3.7 Ga. However, the maximum length of time estimated to be covered by these enhanced field strengths (~18 years) is still much shorter than the inferred length of the high intensity era (~500 Myr). Overall, accretion of cool impactor material has the potential to explain some, but not all, of the unexpectedly high field intensities found in the early lunar paleomagnetic record and may also produce more moderate field intensity signatures. The combination of this mechanism with other hypothesized sources of intermittently high field intensities (e.g., Evans & Tikoo, 2022; Le Bars et al., 2011) could improve the fraction of the inferred high intensity era that is covered by enhanced magnetic fields. Future work studying the remanent magnetization of more lunar samples from early lunar history could determine if there exists further variability in the high intensity period similar to what would be expected from this mechanism.

Acknowledgments: F. N. F., A. J. E., B. C. J., and S. M. T. were supported by NASA grant 80NSSC20K0861.

Data and materials availability: All data to reproduce the results of this study are provided in the references or are available at Harvard Dataverse via https://doi.org/10.7910/DVN/BGVQJU (Nichols-Fleming, 2022). The Jupyter Notebook to execute the analysis in this study can be found at GitHub via https://doi.org/10.5281/zenodo.5764960 (Nichols-Fleming, 2023).

References

Abramov, O., Wong, S. M., & Kring, D. A. (2012). Differential melt scaling for oblique impacts on terrestrial planets. *Icarus*, *218*(2), 906–916. https://doi.org/10.1016/j.icarus.2011.12.022

Baek, S.-M., Kim, K.-H., Garrick-Bethell, I., & Jin, H. (2019). Magnetic Anomalies Within the Crisium Basin: Magnetization Directions, Source Depths, and Ages. *Journal of Geophysical Research: Planets*, *124*(2), 223–242. https://doi.org/10.1029/2018JE005678

Biggin, A. J., Steinberger, B., Aubert, J., Suttie, N., Holme, R., Torsvik, T. H., et al. (2012). Possible links between long-term geomagnetic variations and whole-mantle convection processes. *Nature Geoscience*, *5*(8), 526–533. https://doi.org/10.1038/ngeo1521

Bottke, W. F., & Norman, M. D. (2017). The Late Heavy Bombardment. *Annual Review of Earth and Planetary Sciences*, *45*(1), 619–647. https://doi.org/10.1146/annurev-earth-063016-020131

Buono, A. S., & Walker, D. (2011). The Fe-rich liquidus in the Fe–FeS system from 1bar to 10GPa. *Geochimica et Cosmochimica Acta*, *75*(8), 2072–2087. https://doi.org/10.1016/j.gca.2011.01.030

Buz, J., Weiss, B. P., Tikoo, S. M., Shuster, D. L., Gattacceca, J., & Grove, T. L. (2015). Magnetism of a very young lunar glass. *Journal of Geophysical Research (Planets)*, *120*(10), 1720–1735. https://doi.org/10.1002/2015JE004878

Carslaw, H. S., & Jaeger, J. C. (1959). Appendix VI. Thermal Properties of some Common Substances. In *Conduction of heat in solids* (2d ed, p. 382). Oxford: Clarendon Press.

Cébron, D., Laguerre, R., Noir, J., & Schaeffer, N. (2019). Precessing spherical shells: flows, dissipation, dynamo and the lunar core. *Geophysical Journal International*, *219*(Supplement_1), S34–S57. https://doi.org/10.1093/gji/ggz037

Christensen, U. R., & Aubert, J. (2006). Scaling properties of convection-driven dynamos in rotating spherical shells and application to planetary magnetic fields. *Geophysical Journal International*, *166*(1), 97–114. https://doi.org/10.1111/j.1365-246X.2006.03009.x

Christensen, U. R., Holzwarth, V., & Reiners, A. (2009). Energy flux determines magnetic field strength of planets and stars. *Nature*, *457*(7226), 167–169. https://doi.org/10.1038/nature07626

Cintala, M. J., & Grieve, R. A. F. (1998). Scaling impact-melt and crater dimensions: Implications for the lunar cratering record. *Meteoritics and Planetary Science*, *33*, 889–912. https://doi.org/10.1111/j.1945-5100.1998.tb01695.x

Cisowski, S. M., Collinson, D. W., Runcorn, S. K., Stephenson, A., & Fuller, M. (1983). A review of lunar paleointensity data and implications for the origin of lunar magnetism. *Journal of Geophysical Research: Solid Earth*, *88*(S02), A691–A704. https://doi.org/10.1029/JB088iS02p0A691

Collins, G. S., Melosh, H. J., Morgan, J. V., & Warner, M. R. (2002). Hydrocode Simulations of Chicxulub Crater Collapse and Peak-Ring Formation. *Icarus*, *157*(1), 24–33. https://doi.org/10.1006/icar.2002.6822

Cournède, C., Gattacceca, J., & Rochette, P. (2012). Magnetic study of large Apollo samples: Possible evidence for an ancient centered dipolar field on the Moon. *Earth and Planetary Science Letters*, *331*, 31–42. https://doi.org/10.1016/j.epsl.2012.03.004

Davidson, P. A. (2013). Scaling laws for planetary dynamos. *Geophysical Journal International*, *195*(1), 67–74. https://doi.org/10.1093/gji/ggt167

Dufek, J., & Bergantz, G. W. (2005). Lower Crustal Magma Genesis and Preservation: a Stochastic Framework for the Evaluation of Basalt–Crust Interaction. *Journal of Petrology*, *46*(11), 2167–2195. https://doi.org/10.1093/petrology/egi049

Dwyer, C. A., Stevenson, D. J., & Nimmo, F. (2011). A long-lived lunar dynamo driven by continuous mechanical stirring. *Nature*, *479*(7372), 212–214. https://doi.org/10.1038/nature10564

Evans, A. J., & Tikoo, S. M. (2022). An episodic high-intensity lunar core dynamo. *Nature Astronomy*, *6*(3), 325–330. https://doi.org/10.1038/s41550-021-01574-y

Evans, A. J., Zuber, M. T., Weiss, B. P., & Tikoo, S. M. (2014). A wet, heterogeneous lunar interior: Lower mantle and core dynamo evolution. *Journal of Geophysical Research (Planets)*, *119*(5), 1061–1077. https://doi.org/10.1002/2013JE004494

Evans, A. J., Andrews-Hanna, J. C., Head III, J. W., Soderblom, J. M., Solomon, S. C., & Zuber, M. T. (2018). Reexamination of Early Lunar Chronology With GRAIL Data: Terranes, Basins, and Impact Fluxes. *Journal of Geophysical Research: Planets*, *123*(7), 1596–1617. https://doi.org/10.1029/2017JE005421

Evans, A. J., Tikoo, S. M., & Andrews-Hanna, J. C. (2018). The Case Against an Early Lunar Dynamo Powered by Core Convection. *Geophysical Research Letters*, *45*(1), 98–107. https://doi.org/10.1002/2017GL075441

Fraser, M. E., Lu, W. K., Hamielec, A. E., & Murarka, R. (1971). Surface tension measurements on pure liquid iron and nickel by an oscillating drop technique. *Metallurgical Transactions*, *2*(3), 817–823. https://doi.org/10.1007/BF02662741

Garrick-Bethell, I., & Kelley, M. R. (2019). Reiner Gamma: A Magnetized Elliptical Disk on the Moon. *Geophysical Research Letters*, *46*(10), 5065–5074. https://doi.org/10.1029/2019GL082427

Garrick-Bethell, I., Weiss, B. P., Shuster, D. L., & Buz, J. (2009). Early Lunar Magnetism. *Science*, *323*(5912), 356–359. https://doi.org/10.1126/science.1166804

Garrick-Bethell, I., Weiss, B. P., Shuster, D. L., Tikoo, S. M., & Tremblay, M. M. (2017). Further evidence for early lunar magnetism from troctolite 76535. *Journal of Geophysical Research: Planets*, *122*(1), 76–93. https://doi.org/10.1002/2016JE005154

Gattacceca, J., & Rochette, P. (2004). Toward a robust normalized magnetic paleointensity method applied to meteorites. *Earth and Planetary Science Letters*, *227*(3), 377–393. https://doi.org/10.1016/j.epsl.2004.09.013

Glatzmaier, G. A., Coe, R. S., Hongre, L., & Roberts, P. H. (1999). The role of the Earth's mantle in controlling the frequency of geomagnetic reversals. *Nature*, *401*(6756), 885–890. https://doi.org/10.1038/44776

Grieve, R. A. F., & Cintala, M. J. (1992). An analysis of differential impact melt-crater scaling and implications for the terrestrial impact record. *Meteoritics*, *27*, 526–538. https://doi.org/10.1111/j.1945-5100.1992.tb01074.x

Grieve, Richard A. F., Stöffler, D., & Deutsch, A. (1991). The Sudbury structure: Controversial or misunderstood? *Journal of Geophysical Research: Planets*, *96*(E5), 22753–22764. https://doi.org/10.1029/91JE02513

Hamid, S. S., O'Rourke, J. G., & Soderlund, K. M. (2023). A Long-lived Lunar Magnetic Field Powered by Convection in the Core and a Basal Magma Ocean. *The Planetary Science Journal*, *4*(5), 88. https://doi.org/10.3847/PSJ/accb99

Head, J. W., III. (1976). Lunar volcanism in space and time. *Reviews of Geophysics and Space Physics*, *14*, 265–300. https://doi.org/10.1029/RG014i002p00265

Hevey, P. J., & Sanders, I. S. (2006). A model for planetesimal meltdown by $^{26\$}$Al and its implications for meteorite parent bodies. *Meteoritics and Planetary Science*, *41*(1), 95–106. https://doi.org/10.1111/j.1945-5100.2006.tb00195.x

Hiesinger, H., Head, J. W., Wolf, U., Jaumann, R., & Neukum, G. (2003). Ages and stratigraphy of mare basalts in Oceanus Procellarum, Mare Nubium, Mare Cognitum, and Mare Insularum. *Journal of Geophysical Research (Planets)*, *108*, 5065. https://doi.org/10.1029/2002JE001985

Hiesinger, H., Head, J. W., Wolf, U., Jaumann, R., & Neukum, G. (2011). Ages and stratigraphy of lunar mare basalts: A synthesis. https://doi.org/10.1130/2011.2477(01)

Hirth, G., & Kohlstedt, D. (2003). Rheology of the upper mantle and the mantle wedge: A view from the experimentalists. *Washington DC American Geophysical Union Geophysical Monograph Series*, *138*, 83–105. https://doi.org/10.1029/138GM06

Hood, L. L. (2011). Central magnetic anomalies of Nectarian-aged lunar impact basins: Probable evidence for an early core dynamo. *Icarus*, *211*(2), 1109–1128. https://doi.org/10.1016/j.icarus.2010.08.012

Hood, L. L., & Artemieva, N. A. (2008). Antipodal effects of lunar basin-forming impacts: Initial 3D simulations and comparisons with observations. *Icarus*, *193*, 485–502. https://doi.org/10.1016/j.icarus.2007.08.023

Hood, L. L., & Spudis, P. D. (2016). Magnetic anomalies in the Imbrium and Schrödinger impact basins: Orbital evidence for persistence of the lunar core dynamo into the Imbrian epoch. *Journal of Geophysical Research: Planets*, *121*(11), 2268–2281. https://doi.org/10.1002/2016JE005166

Hood, L. L., Tsunakawa, H., & Spudis, P. D. (2014). Central Magnetic Anomalies in Old Lunar Impact Basins: New Constraints on the Earliest History of the Former Core Dynamo, 1482. Presented at the 45th Annual Lunar and Planetary Science Conference.

Hood, L. L., Torres, C. B., Oliveira, J. S., Wieczorek, M. A., & Stewart, S. T. (2021). A New Large-Scale Map of the Lunar Crustal Magnetic Field and Its Interpretation. *Journal of Geophysical Research: Planets*, *126*(2), e2020JE006667. https://doi.org/10.1029/2020JE006667

Hood, L. L., Oliveira, J. S., Andrews-Hanna, J., Wieczorek, M. A., & Stewart, S. T. (2021). Magnetic Anomalies in Five Lunar Impact Basins: Implications for Impactor Trajectories and Inverse Modeling. *Journal of Geophysical Research: Planets*, *126*(2), e2020JE006668. https://doi.org/10.1029/2020JE006668

Hounslow, M. W., Domeier, M., & Biggin, A. J. (2018). Subduction flux modulates the geomagnetic polarity reversal rate. *Tectonophysics*, *742–743*, 34–49. https://doi.org/10.1016/j.tecto.2018.05.018

Huppert, H. E. (1982). The propagation of two-dimensional and axisymmetric viscous gravity currents over a rigid horizontal surface. *Journal of Fluid Mechanics*, *121*, 43–58. https://doi.org/10.1017/S0022112082001797

Ivanov, B. A. (2005). Numerical Modeling of the Largest Terrestrial Meteorite Craters. *Solar System Research*, *39*(5), 381–409. https://doi.org/10.1007/s11208-005-0051-0

Jault, D. (2015). Illuminating the electrical conductivity of the lowermost mantle from below. *Geophysical Journal International*, *202*(1), 482–496. https://doi.org/10.1093/gji/ggv152

Johnson, B. C., Collins, G. S., Minton, D. A., Bowling, T. J., Simonson, B. M., & Zuber, M. T. (2016). Spherule layers, crater scaling laws, and the population of ancient terrestrial impactors. *Icarus*, *271*, 350–359. https://doi.org/10.1016/j.icarus.2016.02.023

Jung, J., Tikoo, S. M., Gattacceca, J., & Lepaulard, C. (2021). Shock Demagnetization Does Not Fully Explain Variations in the Lunar Paleointensity Record, 2388. Presented at the 52nd Lunar and Planetary Science Conference.

Kelley, M. R., & Garrick-Bethell, I. (2020). Gravity constraints on the age and formation of the Moon's Reiner Gamma magnetic anomaly. *Icarus*, *338*, 113465. https://doi.org/10.1016/j.icarus.2019.113465

Kendall, J. D., & Melosh, H. J. (2016). Differentiated planetesimal impacts into a terrestrial magma ocean: Fate of the iron core. *Earth and Planetary Science Letters*, *448*, 24–33. https://doi.org/10.1016/j.epsl.2016.05.012

Khan, A., Connolly, J. a. D., Pommier, A., & Noir, J. (2014). Geophysical evidence for melt in the deep lunar interior and implications for lunar evolution. *Journal of Geophysical Research: Planets*, *119*(10), 2197–2221. https://doi.org/10.1002/2014JE004661

Konrad, W., & Spohn, T. (1997). Thermal history of the Moon: implications for an early core dynamo and post-accretional magmatism. *Advances in Space Research*, *19*(10), 1511–1521. https://doi.org/10.1016/S0273-1177(97)00364-5

Lamb, S. H. (1945). *Hydrodynamics (Dover Books on Physics)*. Dover Publications. Retrieved from https://www.xarg.org/ref/a/0486602567/

Laneuville, M., Wieczorek, M. A., Breuer, D., Aubert, J., Morard, G., & Rückriemen, T. (2014). A long-lived lunar dynamo powered by core crystallization. *Earth and Planetary Science Letters*, *401*, 251–260. https://doi.org/10.1016/j.epsl.2014.05.057

Lawrence, K., Johnson, C., Tauxe, L., & Gee, J. (2008). Lunar paleointensity measurements: Implications for lunar magnetic evolution. *Physics of the Earth and Planetary Interiors*, *168*(1–2), 71–87. https://doi.org/10.1016/j.pepi.2008.05.007

Le Bars, M., Wieczorek, M. A., Karatekin, Ö., Cébron, D., & Laneuville, M. (2011). An impact-driven dynamo for the early Moon. *Nature*, *479*(7372), 215–218. https://doi.org/10.1038/nature10565

Marchi, S., Canup, R. M., & Walker, R. J. (2018). Heterogeneous delivery of silicate and metal to the Earth by large planetesimals. *Nature Geoscience*, *11*(1), 77–81. https://doi.org/10.1038/s41561-017-0022-3

Matsuyama, I., Nimmo, F., Keane, J. T., Chan, N. H., Taylor, G. J., Wieczorek, M. A., et al. (2016). GRAIL, LLR, and LOLA constraints on the interior structure of the Moon. *Geophysical Research Letters*, *43*(16), 8365–8375. https://doi.org/10.1002/2016GL069952

Melosh, H. J. (1989). Impact cratering: A geologic process. *Research Supported by NASA. New York, Oxford University Press (Oxford Monographs on Geology and Geophysics, No. 11), 1989, 253 p.* Retrieved from http://adsabs.harvard.edu/abs/1989icgp.book.....M

Mighani, S., Wang, H., Shuster, D. L., Borlina, C. S., Nichols, C. I. O., & Weiss, B. P. (2020). The end of the lunar dynamo. *Science Advances*, *6*(1), eaax0883. https://doi.org/10.1126/sciadv.aax0883

Miljković, K., Wieczorek, M. A., Collins, G. S., Laneuville, M., Neumann, G. A., Melosh, H. J., et al. (2013). Asymmetric Distribution of Lunar Impact Basins Caused by Variations in Target Properties. *Science*, *342*(6159), 724–726. https://doi.org/10.1126/science.1243224

Mitchell, D. L., Halekas, J. S., Lin, R. P., Frey, S., Hood, L. L., Acuña, M. H., & Binder, A. (2008). Global mapping of lunar crustal magnetic fields by Lunar Prospector. *Icarus*, *194*(2), 401–409. https://doi.org/10.1016/j.icarus.2007.10.027

Morard, G., Bouchet, J., Rivoldini, A., Antonangeli, D., Roberge, M., Boulard, E., et al. (2018). Liquid properties in the Fe-FeS system under moderate pressure: Tool box to model small planetary cores. *American Mineralogist*, *103*. https://doi.org/10.2138/am-2018-6405

Morbidelli, A., Nesvorny, D., Laurenz, V., Marchi, S., Rubie, D. C., Elkins-Tanton, L., et al. (2018). The timeline of the lunar bombardment: Revisited. *Icarus*, *305*, 262–276. https://doi.org/10.1016/j.icarus.2017.12.046

Neumann, G. A., Zuber, M. T., Wieczorek, M. A., Head, J. W., Baker, D. M. H., Solomon, S. C., et al. (2015). Lunar impact basins revealed by Gravity Recovery and Interior Laboratory measurements. *Science Advances*, *1*(9), e1500852–e1500852. https://doi.org/10.1126/sciadv.1500852

Nichols, C. I. O., Weiss, B. P., Getzin, B. L., Schmitt, H. H., Béguin, A., Rae, A. S. P., & Shah, J. (2021). The palaeoinclination of the ancient lunar magnetic field from an Apollo 17 basalt. *Nature Astronomy*, *5*(12), 1216–1223. https://doi.org/10.1038/s41550-021-01469-y

Nichols-Fleming, F. (2022). Replication Data for: The Influence of Cool Impactor Accretion on the Early Lunar Paleomagnetic Record. Harvard Dataverse. Retrieved from https://doi.org/10.7910/DVN/BGVQJU

Nichols-Fleming, F. (2023). Jupyter Notebook: Lunar Dynamo Model (Version 1.0.0). GitHub. Retrieved from https://doi.org/10.5281/zenodo.5764960

Onorato, P. I. K., Uhlmann, D. R., & Simonds, C. H. (1978). The thermal history of the Manicouagan Impact Melt Sheet, Quebec. *Journal of Geophysical Research: Solid Earth*, *83*(B6), 2789–2798. https://doi.org/10.1029/JB083iB06p02789

Roberts, P. H., & Glatzmaier, G. A. (2000). Geodynamo theory and simulations. *Reviews of Modern Physics*, *72*, 1081–1123. https://doi.org/10.1103/RevModPhys.72.1081

Samuel, H. (2012). A re-evaluation of metal diapir breakup and equilibration in terrestrial magma oceans. *Earth and Planetary Science Letters*, *313*, 105–114. https://doi.org/10.1016/j.epsl.2011.11.001

Scheinberg, A., Soderlund, K. M., & Schubert, G. (2015). Magnetic field generation in the lunar core: The role of inner core growth. *Icarus*, *254*, 62–71. https://doi.org/10.1016/j.icarus.2015.03.013

Scheinberg, A., Soderlund, K. M., & Elkins-Tanton, L. T. (2018). A basal magma ocean dynamo to explain the early lunar magnetic field. *Earth and Planetary Science Letters*, *492*, 144–151. https://doi.org/10.1016/j.epsl.2018.04.015

Shea, E. K., Weiss, B. P., Cassata, W. S., Shuster, D. L., Tikoo, S. M., Gattacceca, J., et al. (2012). A Long-Lived Lunar Core Dynamo. *Science*, *335*(6067), 453. https://doi.org/10.1126/science.1215359

Stanley, S., Tian, B. Y., Weiss, B. P., & Tikoo, S. M. (2017). The Ancient Lunar Dynamo: How to Resolve the Intensity and Duration Conundrums. In *Lunar and Planetary Science Conference* (p. 1462).

Stegman, D. R., Jellinek, A. M., Zatman, S. A., Baumgardner, J. R., & Richards, M. A. (2003). An early lunar core dynamo driven by thermochemical mantle convection. *Nature*, *421*(6919), 143–146. https://doi.org/10.1038/nature01267

Stephenson, A., & Collinson, D. W. (1974). Lunar magnetic field palaeointensities determined by an anhysteretic remanent magnetization method. *Earth and Planetary Science Letters*, *23*(2), 220–228. https://doi.org/10.1016/0012-821X(74)90196-4

Strauss, B. E., Tikoo, S. M., Gross, J., Setera, J. B., & Turrin, B. (2021). Constraining the Decline of the Lunar Dynamo Field at ≈3.1 Ga Through Paleomagnetic Analyses of Apollo 12 Mare Basalts. *Journal of Geophysical Research: Planets*, *126*(3), e2020JE006715. https://doi.org/10.1029/2020JE006715

Stys, C., & Dumberry, M. (2020). A Past Lunar Dynamo Thermally Driven by the Precession of Its Inner Core. *Journal of Geophysical Research: Planets*, *125*(7), e2020JE006396. https://doi.org/10.1029/2020JE006396

Suavet, C., Weiss, B. P., Cassata, W. S., Shuster, D. L., Gattacceca, J., Chan, L., et al. (2013). Persistence and origin of the lunar core dynamo. *Proceedings of the National Academy of Science*, *110*(21), 8453–8458. https://doi.org/10.1073/pnas.1300341110

Swartzendruber, L. J., Itkin, V. P., & Alcock, C. B. (1991). The Fe-Ni (iron-nickel) system. *Journal of Phase Equilibria*, *12*(3), 288–312. https://doi.org/10.1007/BF02649918

Takahashi, E. (1983). Melting of a Yamato L3 chondorite (Y-74191) up to 30 kbar. *National Institute Polar Research Memoirs*, *30*, 168–180.

Tarduno, J. A., Cottrell, R. D., Lawrence, K., Bono, R. K., Huang, W., Johnson, C. L., et al. (2021). Absence of a long-lived lunar paleomagnetosphere. *Science Advances*, *7*(32), eabi7647. https://doi.org/10.1126/sciadv.abi7647

Thompson, S. L. (1990). ANEOS analytic equations of state for shock physics codes input manual. https://doi.org/10.2172/6939284

Tikoo, S. M., & Evans, A. J. (2022). Dynamos in the Inner Solar System. *Annual Review of Earth and Planetary Sciences*, *50*(1), 99–122. https://doi.org/10.1146/annurev-earth-032320-102418

Tikoo, S. M., Weiss, B. P., Cassata, W. S., Shuster, D. L., Gattacceca, J., Lima, E. A., et al. (2014). Decline of the lunar core dynamo. *Earth and Planetary Science Letters*, *404*, 89–97. https://doi.org/10.1016/j.epsl.2014.07.010

Tikoo, S. M., Weiss, B. P., Shuster, D. L., Suavet, C., Wang, H., & Grove, T. L. (2017). A two-billion-year history for the lunar dynamo. *Science Advances*, *3*(8), e1700207. https://doi.org/10.1126/sciadv.1700207

Turcotte, D. L., & Schubert, G. (2002). Geodynamics - 2nd Edition. *Geodynamics - 2nd Edition, by Donald L. Turcotte and Gerald Schubert, Pp. 472. Cambridge University Press, April 2002. ISBN-10: 0521661862. ISBN-13: 9780521661867. LCCN: QE501 .T83 2002*. https://doi.org/10.2277/0521661862

Vaughan, W. M., Head, J. W., Wilson, L., & Hess, P. C. (2013). Geology and petrology of enormous volumes of impact melt on the Moon: A case study of the Orientale basin impact melt sea. *Icarus*, *223*(2), 749–765. https://doi.org/10.1016/j.icarus.2013.01.017

Wakita, S., Johnson, B. C., Garrick-Bethell, I., Kelley, M. R., Maxwell, R. E., & Davison, T. M. (2021). Impactor material records the ancient lunar magnetic field in antipodal anomalies. *Nature Communications*, *12*(1), 6543. https://doi.org/10.1038/s41467-021-26860-1

Weber, R. C., Lin, P.-Y., Garnero, E. J., Williams, Q., & Lognonné, P. (2011). Seismic Detection of the Lunar Core. *Science*, *331*(6015), 309–312. https://doi.org/10.1126/science.1199375

Weiss, B. P., & Tikoo, S. M. (2014). The lunar dynamo. *Science*, *346*(6214), 1198. https://doi.org/10.1126/science.1246753

Wieczorek, M. A. (2006). The Constitution and Structure of the Lunar Interior. *Reviews in Mineralogy and Geochemistry*, *60*(1), 221–364. https://doi.org/10.2138/rmg.2006.60.3

Wieczorek, M. A., Weiss, B. P., Breuer, D., Cébron, D., Fuller, M., Garrick-Bethell, I., et al. (2022, January). *Lunar magnetism*. Retrieved from https://hal.archives-ouvertes.fr/hal-03524536

Wilhelms, D. E., with sections by McCauley, J. F., & Trask, N. J. (1987). *The geologic history of the Moon* (USGS Numbered Series No. 1348). *The geologic history of the Moon* (Vol. 1348). https://doi.org/10.3133/pp1348

Yu, S., Tosi, N., Schwinger, S., Maurice, M., Breuer, D., & Xiao, L. (2019). Overturn of Ilmenite-Bearing Cumulates in a Rheologically Weak Lunar Mantle. *Journal of Geophysical Research: Planets*, *124*(2), 418–436. https://doi.org/10.1029/2018JE005739

Yu, Y. (2010). Paleointensity determination using anhysteretic remanence and saturation isothermal remanence. *Geochemistry, Geophysics, Geosystems*, *11*(2). https://doi.org/10.1029/2009GC002804

Yue, Z., Johnson, B. C., Minton, D. A., Melosh, H. J., Di, K., Hu, W., & Liu, Y. (2013). Projectile remnants in central peaks of lunar impact craters. *Nature Geoscience*, *6*(6), 435–437. https://doi.org/10.1038/ngeo1828

Zahnle, K. J., Lupu, R., Dobrovolskis, A., & Sleep, N. H. (2015). The tethered Moon. *Earth and Planetary Science Letters*, *427*, 74–82. https://doi.org/10.1016/j.epsl.2015.06.058

Zhang, N., Parmentier, E. M., & Liang, Y. (2013). A 3-D numerical study of the thermal evolution of the Moon after cumulate mantle overturn: The importance of rheology and core solidification. *Journal of Geophysical Research (Planets)*, *118*(9), 1789–1804. https://doi.org/10.1002/jgre.20121

Tables

Parameter	Description	Value
$\boldsymbol{\alpha}$	Thermal Diffusivity of Iron[a]	$\sim 10^{-5}$ m²/s
$\boldsymbol{\eta_0}$	Lunar Mantle Reference Viscosity[b,c]	$10^{18} - 10^{21}$ Pa s
$\boldsymbol{\rho_m}$	Mantle Density[d]	3,350 kg/m³
$\boldsymbol{\rho_c}$	Core Density[d]	6,193 kg/m³
$\boldsymbol{T_{core}}$	Lunar Core Temperature[e,f]	$1{,}700 - 2{,}400$ K
$\boldsymbol{D_{imp}}$	Impactor Diameter	$40 - 320$ km

[a]Carslaw & Jaeger (1959). [b]Hirth & Kohlstedt (2003). [c]Yu et al. (2019). [d]Matsuyama et al. (2016). [e]Evans et al. (2018). [f]Le Bars et al. (2011)

Table 1. Parameter values used for enhanced lunar dynamo calculations.

Figures

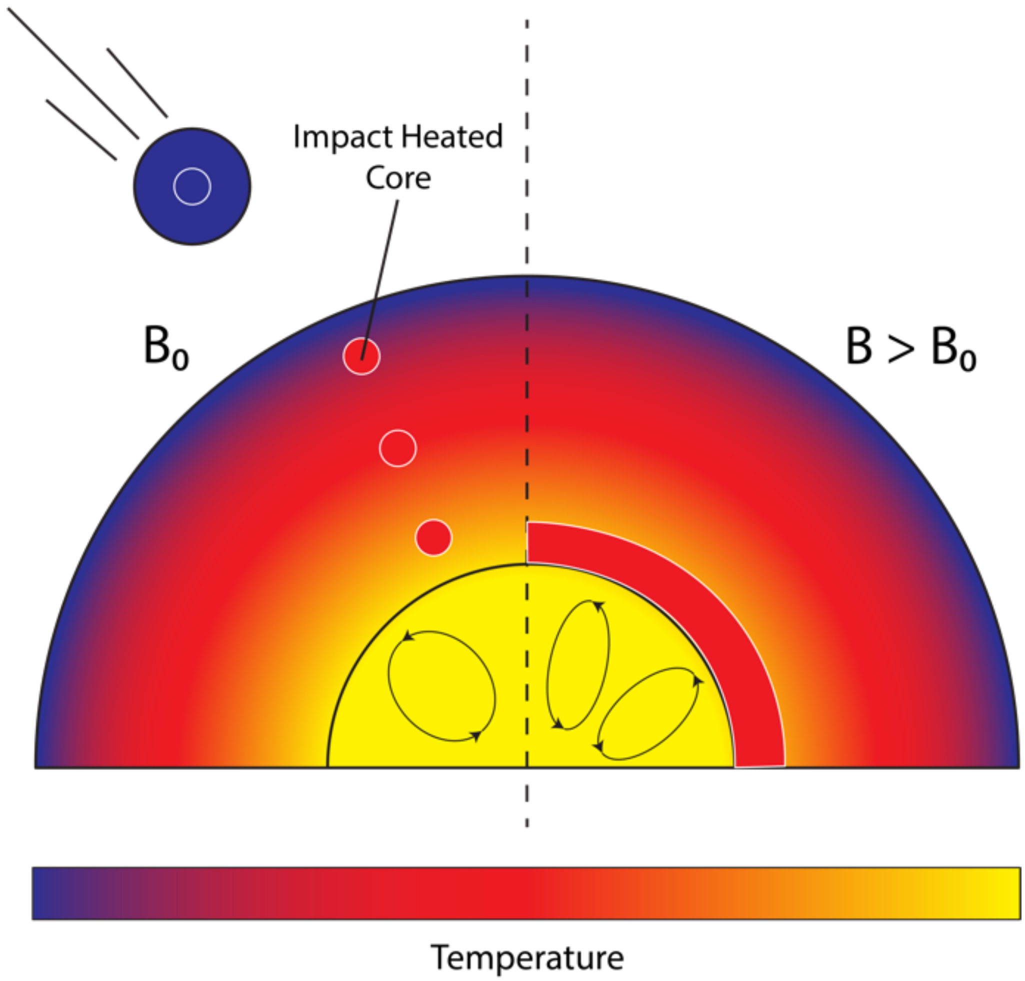

Figure 1. Schematic illustrating a pre-impact (left) and post-impact (right) temperature profile of the Moon. The impact-heated core material from the impactor descends through the lunar mantle (left). Upon reaching the CMB, the impactor core material spreads laterally across the core (right). As the cold impactor material remains above the lunar core (right), more vigorous thermochemical convection within the core is driven by the large temperature difference and higher heat flow at the CMB resulting in a greater magnetic field intensity. Convection cells inside the lunar core are shown.

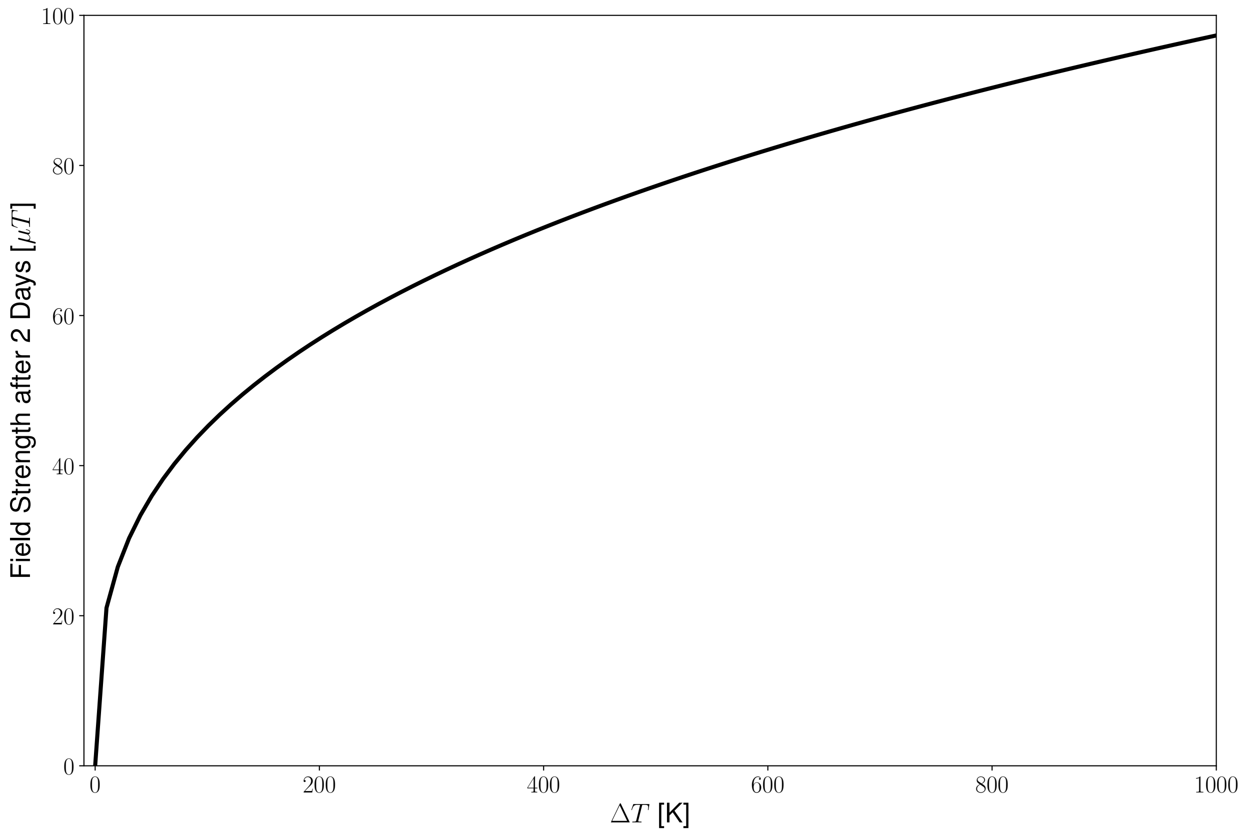

Figure 2. Modeled surface magnetic field intensities (μT) at two days post-emplacement as a function of the initial temperature difference between the lunar core and impactor material. At a model time of two days, the initial impactor size has a negligible influence on the field strength, therefore all initial impactors have approximately the same field strength after two days for each temperature difference as shown here.

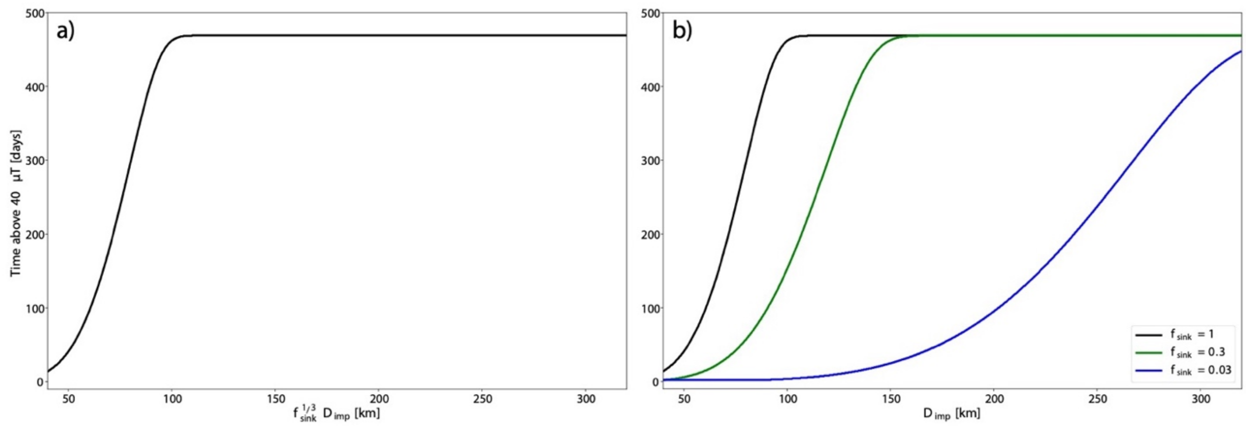

Figure 3. Time in days for which the associated enhanced magnetic field remain above a surface field intensity of 40 μT versus the product of impactor size and the cube root of the efficiency factor (a) or the impactor size with included efficiency factors of $f_{sink} = 0.03, 0.3, and\ 1$ (b) for a temperature difference between impactor and lunar core material of 1,000 K, and impactor diameters between 40 and 320 km. The efficiency factor represents the volumetric fraction of the impactor core that sinks to the lunar CMB.

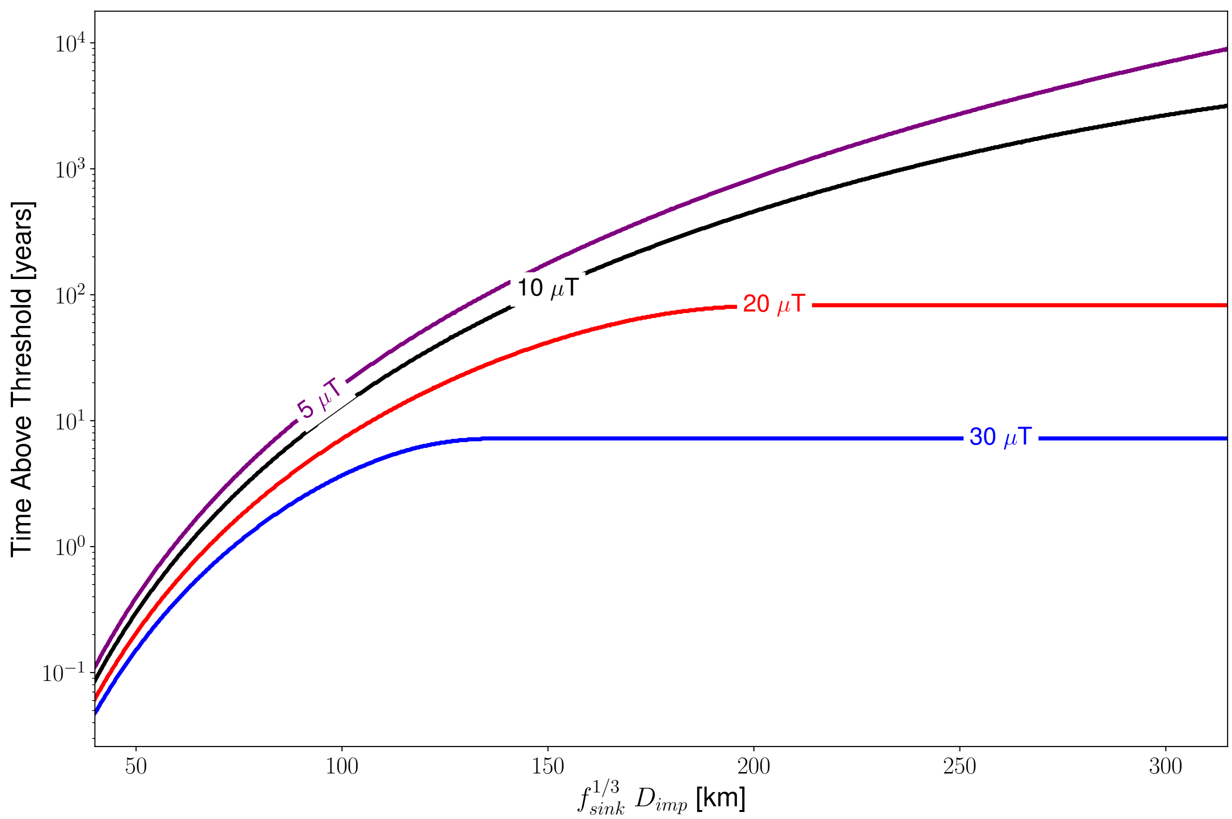

Figure 4. Time in years for which the associated enhanced magnetic field remain above specific magnetic field surface intensities (μT) versus the product of impactor size and the cube root of the efficiency factor for thresholds of 5, 10, 20, and 30 μT, a temperature difference between impactor and lunar core material of 1,000 K, and impactor diameters between 40 and 320 km. The field thresholds are shown as black, red, and blue lines, respectively, and the efficiency factor represents the volumetric fraction of the impactor core that sinks to the lunar CMB.

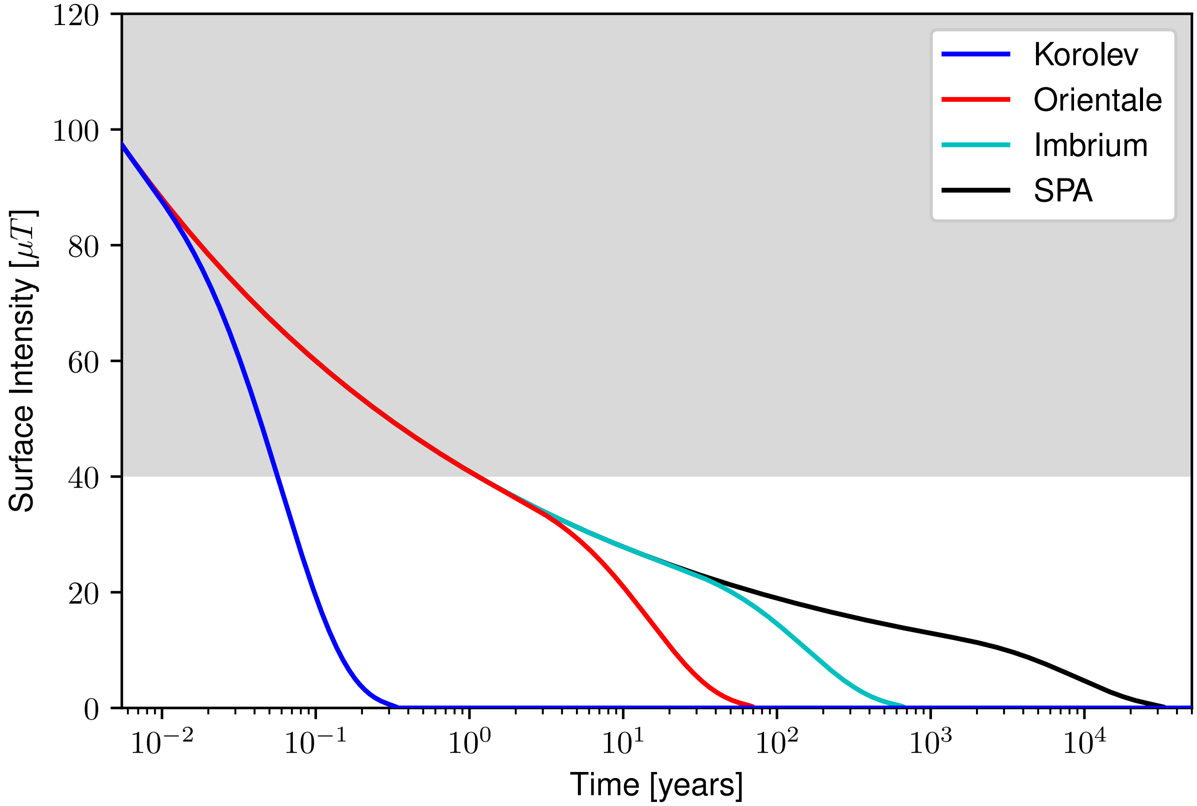

Figure 5. Surface magnetic field intensities (μT) versus time (years) for impactor sizes comparable to those producing the Korolev (blue), Orientale (red), Imbrium (cyan), and SPA (black) basins with efficiency factors $f_{sink} = 1$. In each case, the initial temperature difference between the impactor material and lunar core is 1,000 K. The impactor sizes were determined using the basin scaling law of Johnson, et al. (2016b) with basin sizes from Neumann et al. (2015) assuming a 45° impact angle and a vertical impact velocity of 7.3 km/s. The grey rectangle illustrates the high intensity field strength regime which ranges between 40 and 120 μT.

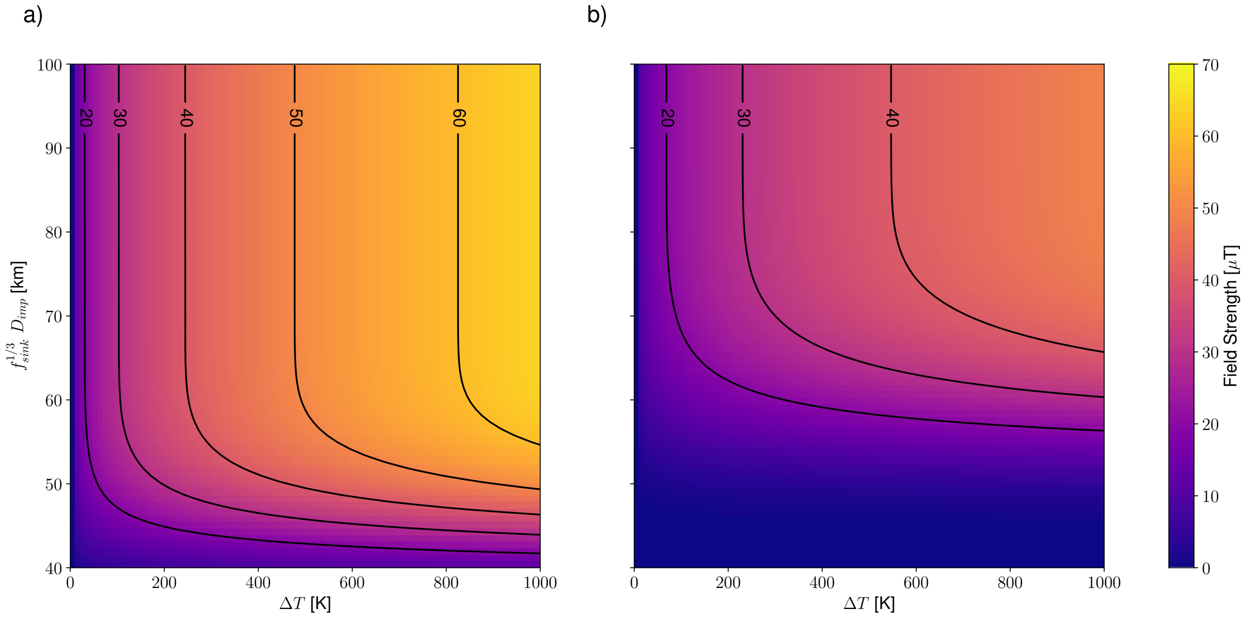

Figure 6. Surface magnetic field intensities (μT) at 28 days (a) and 140 days (b) for impactor diameters between 40 and 100 km times the cube root of the efficiency factor and initial temperature differences between the core and the impactor material ranging from 0 to 1,000 K. Field strengths are shown with the color bar. Contours for field intensities between 20 and 60 μT in increments of 10 μT are shown (solid black lines).

Supplemental Material

The time required to reach the lunar CMB for a fluid or solid sphere of impactor core material is governed by the flow regime of the descent. As the descent through the lunar mantle is in the Stokes regime, the sinking velocity for a sphere will be the terminal velocity, given by

$$v_s = \beta \frac{(\rho_m - \rho_s) g R^2}{\eta} \tag{S1}$$

where $\beta = 2/9$ for a rigid sphere (Lamb, 1945), $\beta = 1/3$ (Hadamard, 1911; Rybczyński, 1911) for a fluid sphere, g is the gravitational acceleration, ρ_m is the density of the sinking impactor material, ρ_s is the density of the surrounding lunar mantle, R is the radius of the sphere of sinking impactor material, and η is the viscosity of the lunar mantle. Values for the parameters used for these calculations can be found in Table 1 of the main text. The distance required to accelerate to this velocity is $\lesssim$ 2x the radius of the sphere of sinking material (Samuel, 2012), which is very small compared to the full distance to the lunar CMB. Therefore, we can ignore the small amount of acceleration experienced by the material and treat the sinking velocity as constant. Sinking times for the impactor material sizes considered in this work are thus found by dividing the distance to the lunar CMB (~1,357 km; Williams et al., 2014) by the sinking velocity. The sinking timescales of rigid spheres are between $5.8 f_{sink}^{-2/3}$ and $370 f_{sink}^{-2/3}$ kyr for the lowest mantle reference viscosity of 10^{18} Pa s and significantly longer at $5.8 f_{sink}^{-2/3} - 370 f_{sink}^{-2/3}$ Myr for the highest reference viscosity of 10^{21} Pa s. The sinking velocities of a fluid sphere are 1.5x faster than those of a rigid sphere, therefore sinking times of fluid spheres are 2/3 the descent times of a rigid sphere. In all cases, these timescales are smaller than the ~500 Myr inferred length of the high intensity era, making the effects of impactors relevant to the lunar paleorecord.

The values of conductive timescales for spheres of impactor material as mentioned in Section 5 of the main text are calculated via

$$\tau = \frac{R^2}{\alpha} \tag{S2}$$

where α is the thermal diffusivity of iron and R is the radius of the sphere of impactor material. The values used in these calculations can be found in Table 1 of the main text. Figure S1 shows the ratio of the conductive timescale to the sinking timescale of the impactor material for impactor diameters between 40 and $320f^{1/3}$ km and lunar mantle reference viscosities of 10^{18} and 10^{21} Pa s. For the smallest considered mantle reference viscosity, sinking times are smaller than the conductive timescale and therefore heat is not efficiently transferred from the lunar mantle to the impactor core material. In the highest reference viscosity case, the conductive timescale is much shorter than the sinking time and therefore heat from the mantle is expected to be significant.

Supplemental References

Hadamard, J. (1911). Mouvement permanent lent d'une sphère liquide et visqueuse dans un liquide visqueux. *C.R. Acad. Sci.*, *152*, 1735–1738.

Johnson, B. C., Collins, G. S., Minton, D. A., Bowling, T. J., Simonson, B. M., & Zuber, M. T. (2016). Spherule layers, crater scaling laws, and the population of ancient terrestrial impactors. *Icarus*, *271*, 350–359. https://doi.org/10.1016/j.icarus.2016.02.023

Lamb, S. H. (1945). *Hydrodynamics (Dover Books on Physics)*. Dover Publications. Retrieved from https://www.xarg.org/ref/a/0486602567/

Matsuyama, I., Nimmo, F., Keane, J. T., Chan, N. H., Taylor, G. J., Wieczorek, M. A., et al. (2016). GRAIL, LLR, and LOLA constraints on the interior structure of the Moon. *Geophysical Research Letters*, *43*(16), 8365–8375. https://doi.org/10.1002/2016GL069952

Neumann, G. A., Zuber, M. T., Wieczorek, M. A., Head, J. W., Baker, D. M. H., Solomon, S. C., et al. (2015). Lunar impact basins revealed by Gravity Recovery and Interior Laboratory measurements. *Science Advances*, *1*(9), e1500852–e1500852. https://doi.org/10.1126/sciadv.1500852

Rybczyński, W. (1911). *Über die fortschreitende Bewegung einer flüssigen Kugel in einen zähen Medium*. Akademia Umiejętności.

Samuel, H. (2012). A re-evaluation of metal diapir breakup and equilibration in terrestrial magma oceans. *Earth and Planetary Science Letters*, *313*, 105–114. https://doi.org/10.1016/j.epsl.2011.11.001

Williams, J. G., Konopliv, A. S., Boggs, D. H., Park, R. S., Yuan, D.-N., Lemoine, F. G., et al. (2014). Lunar interior properties from the GRAIL mission. *Journal of Geophysical Research: Planets*, *119*(7), 1546–1578. https://doi.org/10.1002/2013JE004559

Supplemental Figures

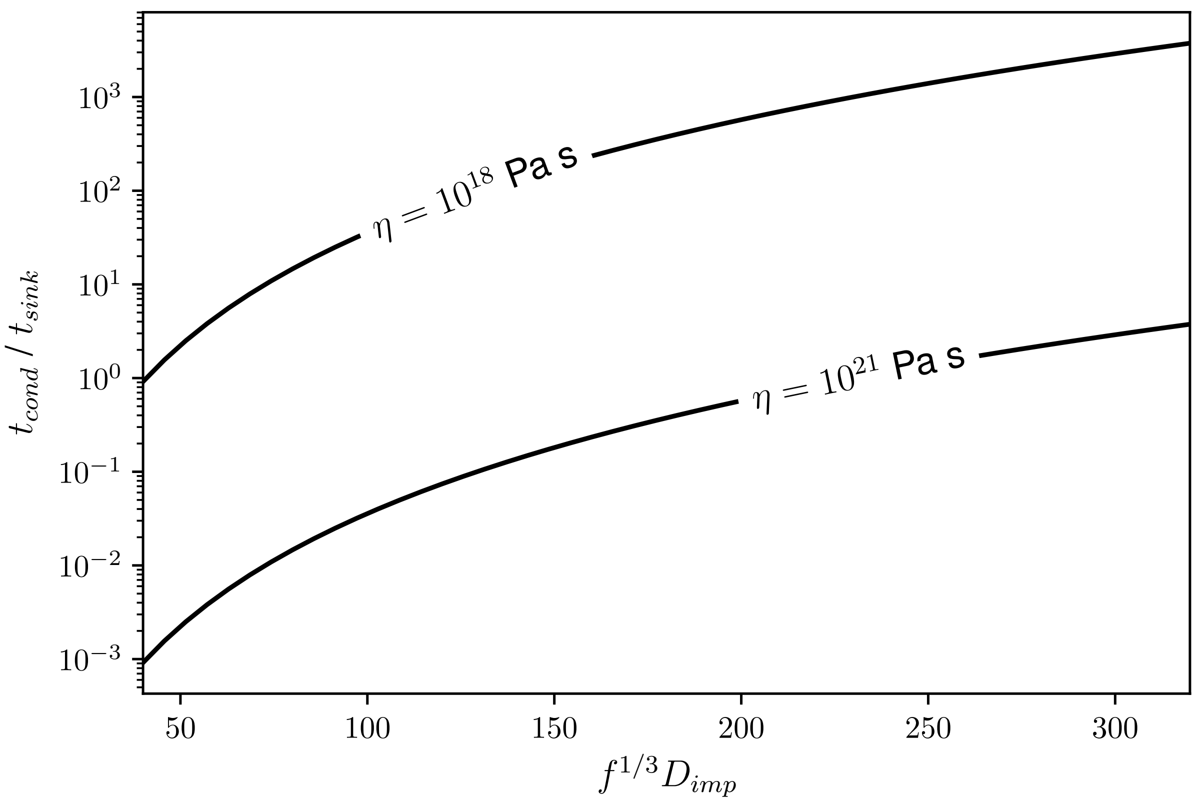

Figure S1. Ratios of conductive timescales to sinking timescales for impactor diameters $40 - 320f^{1/3}$ km and lunar mantle reference viscosities of 10^{18} and 10^{21} Pa s.

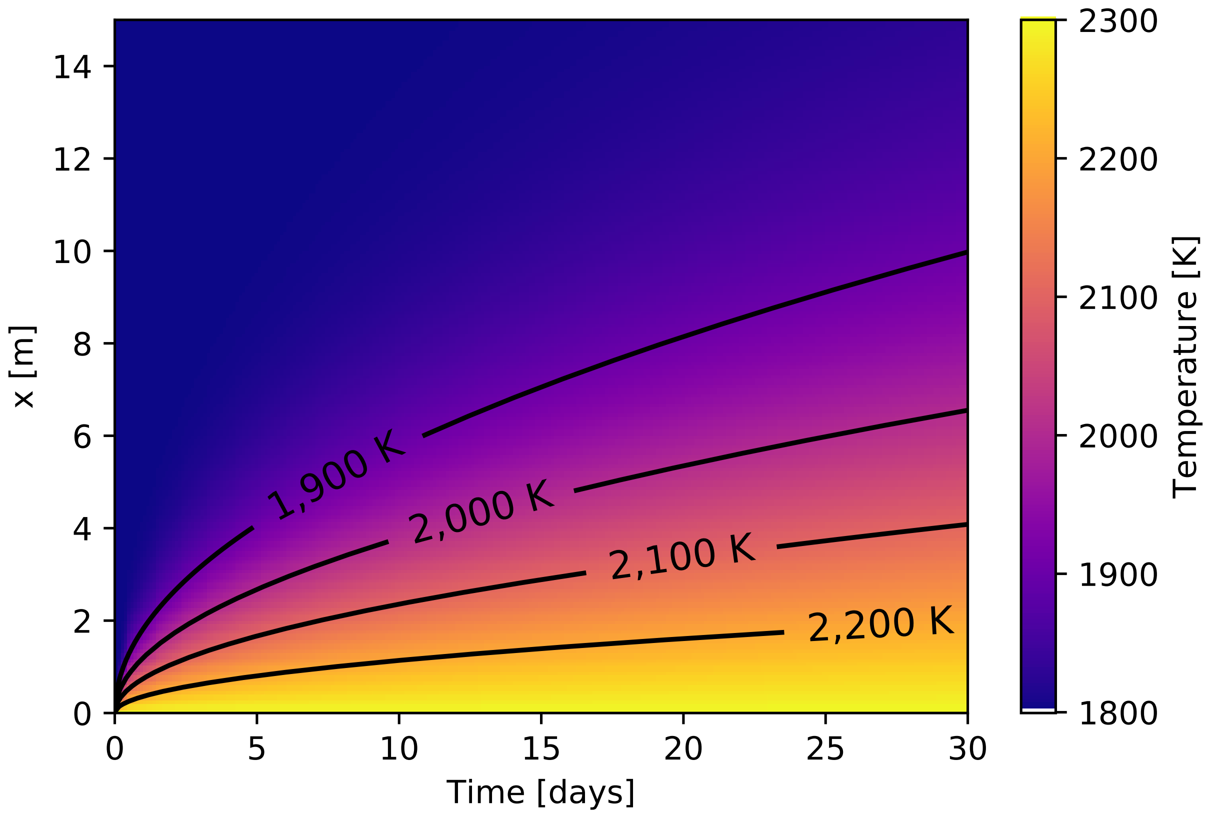

Figure S2. Thermal evolution of the uniform layer of impactor material assuming the full core of a 320 km diameter impactor reaches the lunar CMB and is initially 500 K cooler than the lunar core. After two days, only the lowest ~2 m of the layer has increased in temperature.

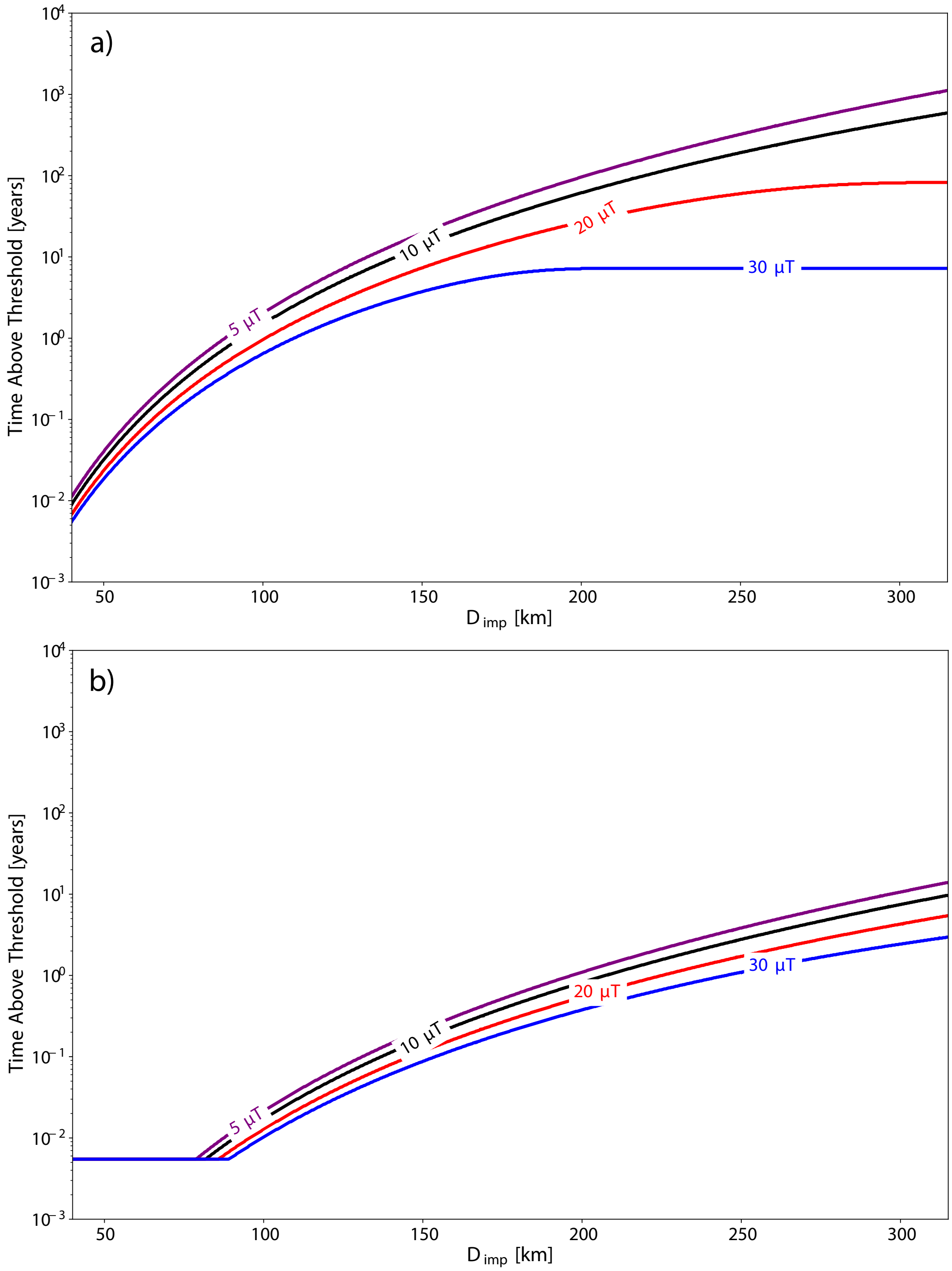

Figure S3. Time in years for which the associated enhanced magnetic field remain above specific magnetic field surface intensities (μT) versus the impactor size for thresholds of 5, 10, 20, and 30 μT, a temperature difference between impactor and lunar core material of 1,000 K, impactor diameters between 40 and 320 km, and efficiency factors of 0.3 (a) and 0.03 (b). The field thresholds are shown as black, red, and blue lines, respectively, and the efficiency factor represents the volumetric fraction of the impactor core that sinks to the lunar CMB.

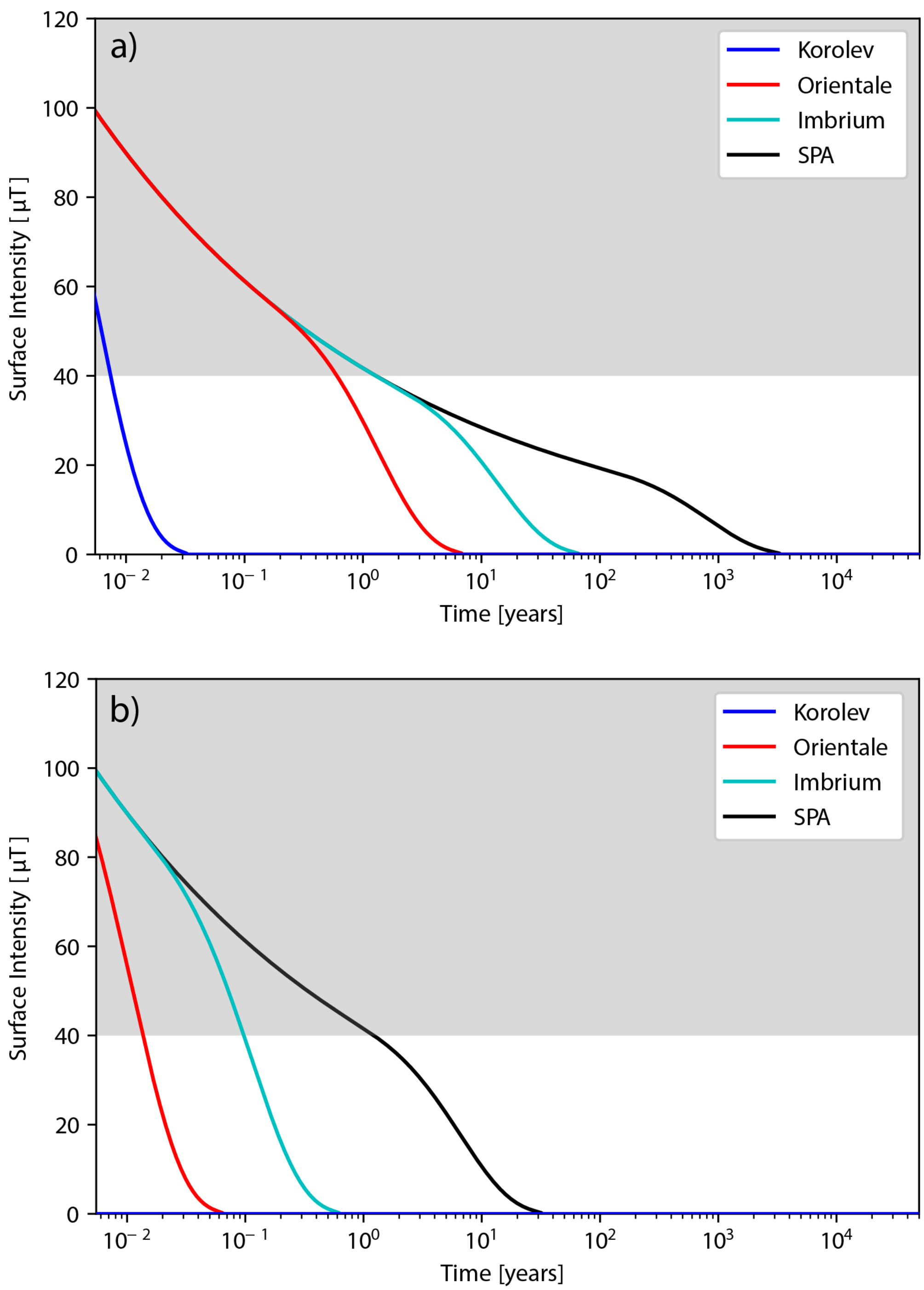

Figure S4. Surface magnetic field intensities (μT) versus time (years) for impactor sizes comparable to those producing the Korolev (blue), Orientale (red), Imbrium (cyan), and SPA (black) basins with efficiency factors $f_{sink} = 0.3$ (a) and 0.03 (b). In each case, the initial temperature difference between the impactor material and lunar core is 1,000 K. The impactor sizes were determined using the basin scaling law of Johnson, et al. (2016b) with basin sizes from Neumann et al. (2015) assuming a 45° impact angle and a vertical impact velocity of 7.3 km/s. The grey rectangle illustrates the high intensity field strength regime which ranges between 40 and 120 μT.

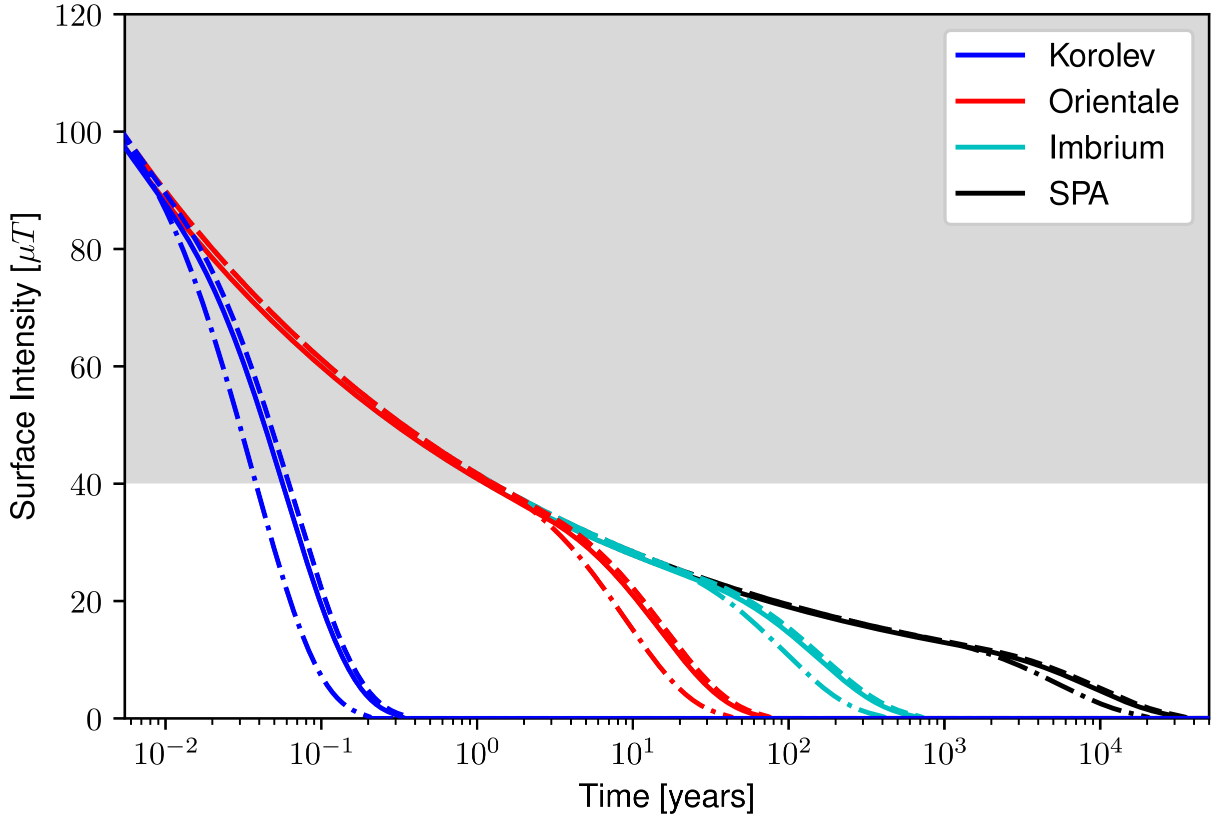

Figure S5. Surface magnetic field intensities (μT) versus time (years) for impactor sizes comparable to those producing the Korolev (blue), Orientale (red), Imbrium (cyan), and SPA (black) basins with efficiency factors $f_{sink} = 1$. In each case, the initial temperature difference between the impactor material and lunar core is 1,000 K. The impactor sizes were determined using the basin scaling law of Johnson et al. (2016) with basin sizes from Neumann et al. (2015) assuming a 45° impact angle and a vertical impact velocity of 7.3 km/s. The grey rectangle illustrates the high intensity field strength regime which ranges between 40 and 120 μT. Solid lines match the densities used in the main text while the dashed and dash-dotted lines represent core densities of 5,707 and 7,636 kg/m^3, respectively. The differences in intensities between magnetic field models with different densities are solely due to the differences in time required to heat different volumes of material as the specific heat capacity and thermal conductivity of the impactor core material is unchanged.

Chapter 3: Porosity Evolution in Metallic Asteroids: Implications for the Origin and Thermal History of Asteroid 16 Psyche

Fiona Nichols-Fleming[1], Alexander J. Evans[1], Brandon C. Johnson[2,3], and Michael M. Sori[2]

[1]Department of Earth, Environmental and Planetary Sciences, Brown University, Providence, RI

[2]Department of Earth, Atmospheric, and Planetary Sciences, Purdue University, West Lafayette, IN

[3]Department of Physics and Astronomy, Purdue University, West Lafayette, IN

This work is published in *JGR: Planets*

Nichols-Fleming, F., Evans, A. J., Johnson, B. C., & Sori, M. M. (2022). Porosity evolution in metallic asteroids: Implications for the origin and thermal history of asteroid 16 Psyche. *Journal of Geophysical Research: Planets*, *127*, e2021JE007063. https://doi.org/10.1029/2021JE007063

Short form: Nichols-Fleming et al., *JGR: Planets*, *127*, e2021JE007063 (2022).

Abstract

Some M-type asteroids have measured bulk densities much lower than expected based on their metal-rich surfaces. In particular, the density of the largest M-type asteroid 16 Psyche would require a bulk porosity of ~52 vol% if it has a pure iron composition. We determine that a pure iron Psyche must have cooled to and remained below 800 K to maintain sufficient porosity for that porosity to persist until present. Iron bodies smaller than Psyche could preserve long-lived high porosities (>40%), yet even the smallest M-type asteroids would require temperatures below 925 K. Our results indicate that all iron asteroids must cool to and remain at low temperatures prior to a porosity-adding event in order to retain porosity on timescales longer than a few million years. Accordingly, a pure iron Psyche would not have sufficiently cooled to retain high porosities when large porosity adding events are most likely to have occurred in the early solar system. Hence, Psyche is not likely to be a pure iron exposed core. However, this structure may be more viable for M-type asteroids smaller than Psyche which cool more quickly.

Plain Language Summary

Observations of an asteroid group indicate that they may have metal-rich surfaces, but those asteroids with measured densities are about half as dense as expected for a metal body. These low densities require either that the asteroids either have such high porosities that half of their volume is empty space or that the asteroids are a mix of metal and other lower density materials, such as silicate rock. Psyche, the largest of this asteroid group, is of particular interest due to its recent selection for study by a dedicated NASA mission. To understand if indeed a high porosity metal body is possible, we model the removal of porosity over time for a range of temperatures, initial porosities, and masses of the body. We find that an iron body must cool

below 800 – 925 K before gaining the high porosity required to match the observed low densities of metal-rich asteroids. Since large bodies like Psyche take a long time to cool to low temperatures, their formation as highly porous iron bodies may be difficult to reconcile with our current understanding of the solar system.

1 Introduction

Throughout the asteroid belt, a class of objects that may be the remnants of exposed planetesimal cores have been observed. These M-type asteroids, of which 16 Psyche is the largest (Shepard et al., 2017), are generally characterized by their relatively featureless spectra in the visible and near-infrared (Bus & Binzel, 2002; DeMeo et al., 2009; Tholen, 1984) and high radar albedos (Shepard et al., 2008, 2010, 2015, 2017), which may indicate metal-rich surfaces. The masses and bulk densities of many of these bodies remain largely unconstrained, but a few have bulk densities determined to be much lower than that of iron, requiring either a high porosity or the inclusion of a substantial low-density component, like silicate rock. The bulk densities of M-type asteroids 16 Psyche, 21 Lutetia, 22 Kalliope, and 216 Kleopatra are $3{,}780 \pm 340$, $3{,}400 \pm 300$, $3{,}350 \pm 330$, and $3{,}380 \pm 500$ kg/m^3, respectively (Descamps et al., 2008; Elkins-Tanton et al., 2020; Marchis et al., 2021; Pätzold et al., 2011; Sierks et al., 2011). Notably, the estimate for the bulk density of Psyche is lower than the uncompressed densities of Mercury, Venus, and Earth and would require Psyche to be a rubble pile with a bulk porosity, defined as the average porosity of the entire body, of ~52 vol% if purely composed of iron metal (Elkins-Tanton et al., 2020).

Although generally considered to be the parent bodies for iron meteorites (Cloutis et al., 1990; Magri et al., 1999), this taxonomic group of M-type asteroids appears to have a variety of surface compositions based on their wide range of radar albedos (Shepard et al., 2008, 2010, 2015) and variable appearance and depth of 3 μm hydration features (Rivkin et al., 1995, 2000; Takir et al., 2016). Many magmatic iron meteorites show evidence for fractional crystallization indicative of differentiated parent bodies (Scott & Wasson, 1975) and their cooling rates imply a lack of an overlying insulating mantle (Yang et al., 2007, 2008, 2010). Therefore, a commonly invoked formation hypothesis for Psyche and other M-type asteroids is that these bodies are remanent stripped cores of differentiated bodies (Yang et al., 2007). For a Psyche-sized body, stripped cores could be produced by one or more hit-and-run collisions within the ~1.5 Myr years of the Solar System after which the newly exposed cores would continue to cool and could be further fractured by later impacts (Asphaug et al., 2006; Asphaug & Reufer, 2014, Yang et al., 2007). Several Psyche formation mechanisms have largely been motivated by this hypothesis and the unique possibility of an extant exposed planetesimal core in the solar system would provide unparalleled insight into the formation and evolution of planetary cores (Elkins-Tanton et al., 2016, 2020).

Current mass estimates of a handful of M-type asteroids imply low bulk densities in contrast to their high radar albedos (Shepard et al., 2008, 2010, 2015, 2017). These densities are sufficiently low to require bulk porosities in excess of 40 vol% for an iron body. Porosities this large are generally observed exclusively in rocky, rubble pile asteroids, typically between 200 m and 10 km in diameter (Walsh, 2018) while Psyche has a volume equivalent diameter of $222 -1/+4$ km (Shepard et al., 2021). Here, we identify the temperature limits for maintaining highly porous (>40 vol%) pure iron bodies with masses between 10^{17} and 2.29×10^{19} kg by considering the effects of self-gravity and viscous closure of pore space. We show that high porosities can only be supported in an iron body that has previously cooled for a period of at least ~10 Myr before disruption and reaccumulation as a rubble pile. In particular**,** a pure iron Psyche must have cooled below 800 K to retain a sufficiently high porosity to match its current bulk density.

2 Thermal Evolution Model

To determine the temperatures at which high porosities could be maintained in an iron body, we use a one-dimensional forward time, central space finite difference model of thermal conduction coupled with porosity evolution for a spherical geometry. The initial temperatures of these models represent the conditions at the time of the event which adds porosity to the iron body. We assume an isothermal initial condition which is a reasonable approximation for the thermal state of a body that was fully disrupted and reaccumulated thereafter. Each model has a constant surface temperature of 137 K, the average surface temperature of Psyche (Sori et al., 2017), and a zero flux central boundary condition. All models use the density of kamacite (7,780 kg/m^3; Smyth & Mccormick, 1995) for the metallic iron component following Elkins-Tanton et al. (2020) and begin with a uniform initial porosity φ_0.

Although porosity, in general can be removed via plastic failure and/or viscous pore space closure, for a pure iron Psyche, the central pressure will be below 70 MPa which is not high enough to remove any substantial amount of porosity via plastic failure given the yield stress of iron is ~175 MPa (G. R. Johnson & Cook, 1983). Any less massive iron bodies would have even lower central pressures, further reducing the possibility of pore closure by plastic failure. Therefore, in the absence of plastic failure, the final porosity structure will depend primarily on the thermal evolution of the body. The change in porosity is included as a function of pressure (P) and viscosity (η)

$$\frac{d\varphi}{dt} = -\varphi \frac{P}{\eta(T)} \tag{1}$$

following Fowler (1985). The viscosity of iron is assumed to be Newtonian and vary via

$$\eta(T) = \eta_0 \exp\left(\frac{Q}{RT} - \frac{Q}{RT_0}\right) \tag{2}$$

where the activation energy $Q = 2.5 \times 10^5$ J/mol (Frost & Ashby, 1982) and the reference viscosity $\eta_0 = 10^{11}$ Pa s at a reference temperature $T_0 = 1800$ K following Abrahams & Nimmo (2019). This reference viscosity is obtained by Frost & Ashby (1982) assuming diffusion creep and a grain size of 0.1 mm. As the true grain size is unknown, models with reference viscosities of 10^9 and 10^{13} Pa s are also explored (see Supplemental Information). For a sufficiently high range of stresses within a Psyche-mass body ($\gtrsim 3$ MPa), the deformation of iron may lie in the power-law creep regime (Frost & Ashby, 1982). Hence, with the assumption of Newtonian rheology, we may potentially underestimate the strain-rate at higher pressures where power-law creep is appropriate, which would lead to the removal of less porosity than a more realistic scenario. This underestimation of the compaction rate and noting that the compaction viscosity is not identical to the shear viscosity (Cooper, 1990) suggest our results are upper limits for the temperatures at which porosities can be retained. This conservative estimate for maximum temperatures adds to the robustness of our results.

As the bodies cool, their viscosity increases exponentially following Equation 2. The rate of change of porosity is inversely proportional to the viscosity (Equation 1) and temperatures in our simulations monotonically decrease with time, so porosity evolution effectively ceases when a sufficiently low temperatures are reached, rather than simply becoming very slow. We therefore end models when the rate of change in porosity is less than 0.1% across a one-million-year period. We quantify further loss of porosity to be on the order of 10^{-3} vol% and consequently the additional loss of porosity does not affect our results. Cratering events could add or remove porosity as well, however, these effects would likely be localized near craters and hence unlikely to produce the high bulk porosities of $\gtrsim 40$ vol% that have been inferred from observations (Elkins-Tanton et al., 2020). Accordingly, we do not consider the effects of cratering events on porosity in this model.

Following Bierson et al. (2018), the thermal conductivity varies with porosity and is calculated at each grid point and timestep according to

$$k(\varphi) = k_{Fe}(1 - \varphi) \quad (3)$$

which uses a parallel combination of the two conductivities assuming the heat transfer through the pore space is very inefficient and a constant thermal conductivity of iron $k_{Fe} = 79.5$ W/m K (Carslaw & Jaeger, 1959). This expression for thermal conductivity represents an upper limit of effective conductivities as the true value depends on pore geometry and can decrease more rapidly with porosity than indicated here (Henke et al., 2012). Overestimating the thermal conductivity results in more rapid cooling and enhanced preservation of pore space. Thus, our limits on the initial temperature required for the retention of porosity represent upper limits. Mass is conserved in our model as described in detail in Bierson et al. (2018) such that each grid point responds instantaneously to the contraction of any underlying grid point.

The numerical stability of the model requires that the length of each timestep, Δt, must be less than the Courant number, C (Courant et al., 1967). Using Fourier stability analysis, this stability limit for our model is determined to be $C = (\Delta r)^2/2\kappa$ where Δr is the grid size and κ is the thermal diffusivity. To remain below this limit, Δt is set as one tenth of the minimum Courant number and recalculated after each step, such that

$$\Delta t = \frac{1}{10}\left[\frac{(\Delta r)^2}{2\kappa}\right]. \quad (4)$$

3 Results

Using the mass estimate of Psyche from Elkins-Tanton et al. (2020), we model a pure iron Psyche with uniform initial temperatures of 600, 650, 700, 750, 800, 850, and 900 and initial porosities of 50, 60, 70 and 80 vol%. The initial temperatures and porosities are chosen to produce models with final porosities ranging from a few vol%, where most of the initial porosity is lost, up to within 1 vol% of the initial porosity. Initial porosities greater than ~50 vol% are higher than typically expected, but their use here is meant to demonstrate that cool temperatures are required to produce a final bulk porosity of 52 vol% even when the initial porosities are unrealistically high. Generally, we find that for temperatures greater than 800 K, a pure iron Psyche cannot maintain the high bulk porosities required to match Psyche mass and density estimates. At temperatures greater than 800 K, porosity is annealed on the timescale of millions of years. As an example, the temporal evolution of bulk porosity for a pure iron Psyche with initial temperatures ranging between 600 and 850 K and an initial porosity of 70 vol% is shown in Figure 1. The models with initial temperatures of 600 and 700 K lose less than 2 vol% porosity, while models with the higher initial temperatures of 750, 800 and 850 K lose 10, 31 and 49 vol% porosity, respectively. Between 750 and 800 K, the ratio of internal pressures to the viscosity of iron becomes large enough to remove a substantial amount of the initial porosity.

Figure 2 shows the radial evolution of porosity for the pure iron Psyche models with initial porosities of 70 vol% and initial temperatures of 700, 750, 800, and 850 K. For initial temperatures below 700 K, the initial porosity structure remains largely unchanged (<2 vol%) due to negligible amounts of viscous pore space closure (see for example Figure 2a). For warmer temperatures (Figs. 2b–d), porosity is preferentially removed from the interior of the body where pressures are higher, and for temperatures of 800 and 850 K this results in a final structure where porosity is primarily limited to a porous surface layer of ~12% and ~6% of the radius, respectively (see Figure 2c and 2d).

The final bulk porosities for all of our pure iron Psyche models are shown in Figure 3 with a bilinear interpolation applied between model results. Initial bulk porosities are retained within 2 vol% for temperatures of 700 K and below, while warmer temperatures have final bulk porosities over 10 – 70 vol% below their initial porosities. We therefore find that for the estimated density of a pure iron Psyche to be explained by porosity alone, Psyche must have had a temperature below 800 K at the time porosity was added. The sharp corners in the contour line for 52 vol% porosity shown in Figure 3 are due to the rapid change in amount of porosity lost between models with initial temperatures of 700 and 800 K: as seen in Figure 1, minimal porosity is lost for models with initial temperatures of 700 K and cooler, while the models with an initial temperature of 800 K rapidly lose a large amount of porosity. In general, models which have higher initial porosities retain less of the initial bulk porosity at a given temperature and models with higher temperatures lose porosity on shorter timescales. Final bulk porosities of the models with reference viscosities of 10^9 and 10^{13} Pa s can be seen in Supplemental Figures 1 and 2. In these cases a pure iron Psyche must have cooled below 700 and 900 K, respectively, to retain 52 vol% bulk porosity.

For comparison, we ran similar models for Psyche-mass rocky bodies using the density and thermal conductivity parameters for silicates from Bierson & Nimmo (2019) and viscosity parameters determined for diffusion creep in dry olivine from Karato & Wu (1993). From these models we found that rocky bodies are able to retain high porosity at much greater temperatures, losing less than 1 vol% for temperatures up to the onset of partial melt at ~1300 K for the range of initial porosities considered. Thus, layers composed primarily of rock should be able to retain substantial porosity at Psyche.

Iron bodies less massive than Psyche will have lower internal pressures and therefore would experience the removal of porosity to a lesser extent than a pure iron Psyche at similar temperatures. Using masses of 10^{17}, 5×10^{17}, 10^{18}, and 5×10^{18} kg, we model smaller iron bodies with uniform initial temperatures of 750, 800, 850, 900 and 950 K and initial porosities of 70 vol% to compare with our pure iron Psyche models. Assuming these less massive bodies have the same bulk density as Psyche results in radii of 18.5, 31.6, 39.8, and 68.1 km, respectively. These masses were chosen to cover the effective diameter range of known M-type asteroids, which range from 32 ± 3 km for Asteroid 413 Edburga (Shepard et al., 2015) up to $222\ -1/+4$ km for Psyche (Shepard et al., 2021), when a high bulk porosity is assumed. There exists a bias in known masses towards larger bodies since their gravitational effects on passing asteroids are easier to observe, but for comparison, the estimated masses of 16 Psyche, 21 Lutetia, 22 Kalliope, and 216 Kleopatra are $2.287 \pm 0.07 \times 10^{19}$ (Baer & Chesley, 2017; Elkins-Tanton et al., 2020), $1.700 \pm 0.017 \times 10^{18}$ (Pätzold et al., 2011), $8.16 \pm 0.26 \times 10^{18}$ (Descamps et al., 2008), and $4.64 \pm 0.02 \times 10^{18}$ kg (Descamps et al., 2011), respectively. The final bulk porosities of these models are shown in Figure 4 along with the pure iron Psyche models with the same initial porosity and temperatures and a bilinear interpolation between modeled results.

Although high porosities (>40 vol%) can be maintained for temperatures up to 925 K for the least massive case considered, all of the modeled iron bodies must have had temperatures below 925 K before introduction of pore space to retain high amounts of porosity.

4 Implications for M-type Asteroid Formation

Our models provide insights into formation of M-type asteroids composed of pure iron with a high bulk porosity. First, any surface remanent magnetization produced by an internal core dynamo on these bodies must predate their porosity structure. This relationship occurs because our models show an iron body must cool to at least 925 K to retain high porosities and the Curie temperature, the critical point below which a magnetic field can be recorded, for iron is 1043 K (Garrick-Bethell & Weiss, 2010). The amount of cooling that iron bodies undergo to reach temperatures below 925 K serves as a lower limit since some disrupting impacts, potential sources of porosity for these bodies, could add heat in addition to adding porosity.

Additionally, the location of the magnetic pole produced by an internal dynamo may not be well preserved for a highly porous iron body since the event that added porosity would have had to occur after the body cooled through its Curie temperature. If a disrupting impact was the source of porosity, the impact may have caused reorientation of magnetized materials and may obscure locations of paleopoles. Although in some cases a disruptive impact could heat materials above the Curie temperature, minimal heat is lost during the process of disruption and reaccretion (Ren et al., 2021) and therefore many of these cases would be too warm to retain any of the gained porosity. However, if disruption was incomplete, the body would likely have higher temperatures at the center of the body accompanying a lower initial porosity near the center of the body than assumed here. In such a scenario, our isothermal models serve as upper limits for porosity retention in these bodies. For iron bodies that have been able to retain high porosity, impact heating would need to be highly localized with global temperatures remaining less than 800 – 925 K. In these cases remanent magnetization could remain largely intact, but magnetization within the region of highly localized heating could be lost.

Finally, as our models require disruption to occur after the body has cooled substantially, a highly porous iron body is expected to have fewer contractional tectonic features than an undisrupted body. Our models show < 2 km of radial contraction in the models with temperatures below 700 K in comparison to 10 – 50 km of radial contraction in equivalent warmer models (most of this contraction is from removal of pore space instead of thermal contraction alone). The observed magnitude of radial contraction on a porous iron body could provide insights into both the temperature at the time porosity was added and the amount of porosity initially added to the body. More careful consideration of this relationship is left for future work.

5 Implications for the Formation of Psyche

For an intact differentiated planetesimal with a core of the same mass as Psyche, the timescale to cool below 800 K would be on the order of 100s of Myrs (Bryson et al., 2015; Tarduno et al., 2012). If the core was stripped of its overlying mantle, the timescale of cooling to below 750 K may be as short as ~10 Myr (Scheinberg et al., 2016). The hit-and-run collisions described by Asphaug et al. (2006) occur during the accretion phase of planetary formation, which lasts until approximately 1.5 Myr post-CAI formation (Yang et al., 2007). Alternatively, the catastrophic impacts that disrupted parent bodies of ordinary chondrites occur at or near-peak temperatures for the bodies (Lucas et al., 2020), which are expected to be reached prior to 10

Myr post-CAI formation (Bouvier et al., 2007). As the cooling timescale required by a pure iron Psyche to retain a bulk porosity of ~52 vol.% extends beyond the hit-and-run collision and catastrophic impact epochs of the early solar system, a collision scenario for the formation of a highly porous, pure iron Psyche is not likely. Hence, a pure iron Psyche is not readily explained by a porous metal composition even if it had been previously stripped of its mantle. However, M-type asteroids smaller than Psyche would conceivably cool on timescales much shorter than 100s of Myrs, potentially permitting these small asteroids to be more readily explained as a porous metal bodies. Furthermore, the existence of small M-type asteroids composed of porous metal bodies would be consistent with the observation that these small M-type asteroids are less likely to have the 3 $\boldsymbol{\mu}$m spectral features indicative of hydrated minerals (Rivkin et al., 2000), which are difficult to reconcile with that of a pure metal body. Smaller M-type asteroids such as 216 Kleopatra ($4.64 \pm 0.02 \times 10^{18}$ kg; Descamps et al., 2011) could be remnants of stripped cores while larger bodies like 16 Psyche are more likely to be mixtures of silicates and metal.

If Psyche is a mixture of metal and silicates, it could resemble 21 Lutetia which was observed by the Rosetta mission in 2010 (Coradini et al., 2011; Pätzold et al., 2011; Sierks et al., 2011). Lutetia is an M type asteroid like Psyche, but in some IR observations a weak 1 μm feature is observed that could be consistent with a chondritic surface composition (Birlan et al., 2006). It is notable, however, that this feature was absent from the VIRTIS (Visible and Infrared Thermal Imaging Spectrometer) spectra from Rosetta (Coradini et al., 2011). The bulk composition of Lutetia is still generally thought to be metal-rich with CB, CH, CR and enstatite chondrites as potential meteorite analogs of the surface (Coradini et al., 2011). Although Psyche is also thought have a metal-rich composition, the thermal inertia and radar albedo of Psyche (de Kleer et al., 2021; Shepard et al., 2021) are greater than those of Lutetia (Coradini et al., 2011;

Shepard et al., 2010), which could indicate a higher surface metal content for Psyche. If Psyche and Lutetia are observed to have similar structures and compositions, Psyche may therefore have a greater fraction of metal in its metal-silicate mixture than Lutetia.

Overall, our models show that a pure iron body must maintain a temperature of 925 K or below to retain the substantial porosity until present day. Small M-type asteroids could have cooled quickly enough to retain high porosity (>40 vol%). For such high porosities to be possible for a pure iron Psyche, the event which adds porosity must occur at least 10 Myr and 100s of Myrs after CAI formation for a stripped core and an intact planetesimal, respectively, which is difficult to reconcile with our current understanding of solar system evolution. If Psyche is observed to be pure iron, our models can provide predictions for the relative timing of observed near-surface magnetization. In the limiting case of an event adding porosity of 80 vol%, remanent magnetization by an internally-generated core dynamo within the top ~20 km of Psyche would have likely been emplaced prior to the porosity-adding event, even if Psyche was not fully disrupted. The depth to which remanent magnetization likely predates the porosity adding event increases when initial porosities less than 80% are considered.

The combination of metal and silicates could allow Psyche to have a relatively high metal content (~40 vol%) and a lower bulk density (see Figure 3 in Elkins-Tanton et al., 2020) since rock can support high porosities for warmer temperatures and is an additional low density component. If Psyche is not observed to be purely iron, the existence of some metallic material at the surface in addition to the required lower density component may be the most direct explanation for the high radar reflectivity observed on regions of Psyche's surface (Shepard et al., 2017). Two structures that have been proposed to explain this are that Psyche is a mesosiderite-like body with both silicates and metal exposed on the surface (Viikinkoski et al.,

2018) or that Psyche is a differentiated body with a thin rocky mantle that has experienced ferrovolcanic surface eruptions of iron (Johnson et al., 2020).

Acknowledgements: The authors thank the editors and reviewers for their thoughtful consideration and remarks on this manuscript which have helped to improve its overall quality.

Data Availability: All data to reproduce the results of this study are provided in the references, or are available at Harvard Dataverse via https://doi.org/10.7910/DVN/YFR479 (Nichols-Fleming, 2021b). The Jupyter Notebook to execute the analysis in this study can be found at GitHub via https://doi.org/10.5281/zenodo.5764960 (Nichols-Fleming, 2021a).

References

Abrahams, J. N. H., & Nimmo, F. (2019). Ferrovolcanism: Iron Volcanism on Metallic Asteroids. *Geophysical Research Letters*, *46*, 5055–5064. https://doi.org/10.1029/2019GL082542

Asphaug, E., & Reufer, A. (2014). Mercury and other iron-rich planetary bodies as relics of inefficient accretion. *Nature Geoscience*, *7*, 564–568. https://doi.org/10.1038/ngeo2189

Asphaug, E., Agnor, C. B., & Williams, Q. (2006). Hit-and-run planetary collisions. *Nature*, *439*, 155–160. https://doi.org/10.1038/nature04311

Baer, J., & Chesley, S. R. (2017). Simultaneous Mass Determination for Gravitationally Coupled Asteroids. *The Astronomical Journal*, *154*(2), 76. https://doi.org/10.3847/1538-3881/aa7de8

Bierson, C. J., & Nimmo, F. (2019). Using the density of Kuiper Belt Objects to constrain their composition and formation history. *Icarus*, *326*, 10–17. https://doi.org/10.1016/j.icarus.2019.01.027

Bierson, C. J., Nimmo, F., & McKinnon, W. B. (2018). Implications of the observed Pluto-Charon density contrast. *Icarus*, *309*, 207–219. https://doi.org/10.1016/j.icarus.2018.03.007

Birlan, M., Vernazza, P., Fulchignoni, M., Barucci, M. A., Descamps, P., Binzel, R. P., & Bus, S. J. (2006). Near infra-red spectroscopy of the asteroid 21 Lutetia - I. New results of long-term campaign. *Astronomy & Astrophysics*, *454*(2), 677–681. https://doi.org/10.1051/0004-6361:20054460

Bouvier, A., Blichert-Toft, J., Moynier, F., Vervoort, J. D., & Albarède, F. (2007). Pb–Pb dating constraints on the accretion and cooling history of chondrites. *Geochimica et Cosmochimica Acta*, *71*(6), 1583–1604. https://doi.org/10.1016/j.gca.2006.12.005

Bryson, J. F. J., Nichols, C. I. O., Herrero-Albillos, J., Kronast, F., Kasama, T., Alimadadi, H., et al. (2015). Long-lived magnetism from solidification-driven convection on the pallasite parent body. *Nature*, *517*(7535), 472–475. https://doi.org/10.1038/nature14114

Bus, S. J., & Binzel, R. P. (2002). Phase II of the Small Main-Belt Asteroid Spectroscopic Survey: A Feature-Based Taxonomy. *Icarus*, *158*(1), 146–177. https://doi.org/10.1006/icar.2002.6856

Carslaw, H. S., & Jaeger, J. C. (1959). In *Conduction of heat in solids* (2d ed, p. 497). Oxford: Clarendon Press.

Cloutis, E. A., Gaffey, M. J., Smith, D. G. W., & Lambert, R. St. J. (1990). Reflectance spectra of "featureless" materials and the surface mineralogies of M- and E-class asteroids.

Journal of Geophysical Research, *95*, 281–293. https://doi.org/10.1029/JB095iB01p00281

Cooper, R. F. (1990). Differential stress-induced melt migration: An experimental approach. *Journal of Geophysical Research: Solid Earth*, *95*(B5), 6979–6992. https://doi.org/10.1029/JB095iB05p06979

Coradini, A., Capaccioni, F., Erard, S., Arnold, G., De Sanctis, M. C., Filacchione, G., et al. (2011). The Surface Composition and Temperature of Asteroid 21 Lutetia As Observed by Rosetta/VIRTIS. *Science*, *334*(6055), 492–494. https://doi.org/10.1126/science.1204062

Courant, R., Friedrichs, K., & Lewy, H. (1967). On the Partial Difference Equations of Mathematical Physics. *IBM Journal of Research and Development*, *11*, 215–234. https://doi.org/10.1147/rd.112.0215

DeMeo, F. E., Binzel, R. P., Slivan, S. M., & Bus, S. J. (2009). An extension of the Bus asteroid taxonomy into the near-infrared. *Icarus*, *202*(1), 160–180. https://doi.org/10.1016/j.icarus.2009.02.005

Descamps, P., Marchis, F., Pollock, J., Berthier, J., Vachier, F., Birlan, M., et al. (2008). New determination of the size and bulk density of the binary Asteroid 22 Kalliope from observations of mutual eclipses. *Icarus*, *196*(2), 578–600. https://doi.org/10.1016/j.icarus.2008.03.014

Descamps, P., Marchis, F., Berthier, J., Emery, J. P., Duchêne, G., de Pater, I., et al. (2011). Triplicity and physical characteristics of Asteroid (216) Kleopatra. *Icarus*, *211*(2), 1022–1033. https://doi.org/10.1016/j.icarus.2010.11.016

Elkins-Tanton, L. T., Asphaug, E., Bell, J., Bercovici, D., Bills, B. G., Binzel, R. P., et al. (2016). Asteroid (16) Psyche: The Science of Visiting a Metal World, 1631. Presented at the Lunar and Planetary Science Conference.

Elkins-Tanton, L. T., Asphaug, E., Bell, J. F., Bercovici, H., Bills, B., Binzel, R., et al. (2020). Observations, Meteorites, and Models: A Preflight Assessment of the Composition and Formation of (16) Psyche. *Journal of Geophysical Research (Planets)*, *125*, e06296. https://doi.org/10.1029/2019JE006296

Fowler, A. C. (1985). A mathematical model of magma transport in the asthenosphere. *Geophysical & Astrophysical Fluid Dynamics*, *33*(1–4), 63–96. https://doi.org/10.1080/03091928508245423

Frost, H. J., & Ashby, M. F. (1982). *Deformation-mechanism maps: the plasticity and creep of metals and ceramics* (1st ed). Oxford [Oxfordshire] ; New York: Pergamon Press.

Garrick-Bethell, I., & Weiss, B. P. (2010). Kamacite blocking temperatures and applications to lunar magnetism. *Earth and Planetary Science Letters*, *294*(1), 1–7. https://doi.org/10.1016/j.epsl.2010.02.013

Henke, S., Gail, H.-P., Trieloff, M., Schwarz, W. H., & Kleine, T. (2012). Thermal evolution and sintering of chondritic planetesimals. *Astronomy & Astrophysics*, *537*, A45. https://doi.org/10.1051/0004-6361/201117177

Johnson, B. C., Sori, M. M., & Evans, A. J. (2020). Ferrovolcanism on metal worlds and the origin of pallasites. *Nature Astronomy*, *4*(1), 41–44. https://doi.org/10.1038/s41550-019-0885-x

Johnson, G. R., & Cook, W. H. (1983). A constitutive model and data for materials subjected to large strains, high strain rates, and high temperatures. *Proceedings of the Seventh International Symposium on Ballistics*, 7.

Karato, S., & Wu, P. (1993). Rheology of the Upper Mantle: A Synthesis. *Science*, *260*(5109), 771–778. https://doi.org/10.1126/science.260.5109.771

de Kleer, K., Cambioni, S., & Shepard, M. (2021). The Surface of (16) Psyche from Thermal Emission and Polarization Mapping. *The Planetary Science Journal*, *2*(4), 149. https://doi.org/10.3847/PSJ/ac01ec

Lucas, M. P., Dygert, N., Ren, J., Hesse, M. A., Miller, N. R., & McSween, H. Y. (2020). Evidence for early fragmentation-reassembly of ordinary chondrite (H, L, and LL) parent bodies from REE-in-two-pyroxene thermometry. *Geochimica et Cosmochimica Acta*, *290*, 366–390. https://doi.org/10.1016/j.gca.2020.09.010

Magri, C., Ostro, S. J., Rosema, K. D., Thomas, M. L., Mitchell, D. L., Campbell, D. B., et al. (1999). Mainbelt Asteroids: Results of Arecibo and Goldstone Radar Observations of 37 Objects during 1980–1995. *Icarus*, *140*(2), 379–407. https://doi.org/10.1006/icar.1999.6130

Marchis, F., Jorda, L., Vernazza, P., Brož, M., Hanuš, J., Ferrais, M., et al. (2021). (216) Kleopatra, a low density critically rotating M-type asteroid. *Astronomy & Astrophysics*, *653*, A57. https://doi.org/10.1051/0004-6361/202140874

Nichols-Fleming, F. (2021a). Jupyter Notebook Psyche Thermal Model (Version 1.0.0). GitHub. Retrieved from https://doi.org/https://doi.org/10.5281/zenodo.5764960

Nichols-Fleming, F. (2021b). Replication Data for: Porosity Evolution in Metallic Asteroids: Implications for the Origin and Thermal History of Asteroid 16 Psyche. Harvard Dataverse. Retrieved from https://doi.org/10.7910/DVN/YFR479

Pätzold, M., Andert, T. P., Asmar, S. W., Anderson, J. D., Barriot, J.-P., Bird, M. K., et al. (2011). Asteroid 21 Lutetia: Low Mass, High Density. *Science*, *334*(6055), 491–492. https://doi.org/10.1126/science.1209389

Ren, J., Hesse, M. A., Lucas, M. P., & Dygert, N. (2021). Asteroid Thermal Evolution with Fragmentation and Reassembly into a Rubble Pile, 2620. Presented at the Lunar and Planetary Science Conference.

Rivkin, A. S., Howell, E. S., Britt, D. T., Lebofsky, L. A., Nolan, M. C., & Branston, D. D. (1995). 3-µm Spectrophotometric Survey of M- and E-Class Asteroids. *Icarus*, *117*, 90–100. https://doi.org/10.1006/icar.1995.1144

Rivkin, A. S., Howell, E. S., Lebofsky, L. A., Clark, B. E., & Britt, D. T. (2000). The Nature of M-Class Asteroids from 3-µm Observations. *Icarus*, *145*(2), 351–368. https://doi.org/10.1006/icar.2000.6354

Scheinberg, A., Elkins-Tanton, L. T., Schubert, G., & Bercovici, D. (2016). Core solidification and dynamo evolution in a mantle-stripped planetesimal. *Journal of Geophysical Research (Planets)*, *121*, 2–20. https://doi.org/10.1002/2015JE004843

Scott, E. R. D., & Wasson, J. T. (1975). Classification and properties of iron meteorites. *Reviews of Geophysics*, *13*(4), 527–546. https://doi.org/10.1029/RG013i004p00527

Shepard, M. K., Clark, B. E., Nolan, M. C., Howell, E. S., Magri, C., Giorgini, J. D., et al. (2008). A radar survey of M- and X-class asteroids. *Icarus*, *195*(1), 184–205. https://doi.org/10.1016/j.icarus.2007.11.032

Shepard, M. K., Clark, B. E., Ockert-Bell, M., Nolan, M. C., Howell, E. S., Magri, C., et al. (2010). A radar survey of M- and X-class asteroids II. Summary and synthesis. *Icarus*, *208*(1), 221–237. https://doi.org/10.1016/j.icarus.2010.01.017

Shepard, M. K., Taylor, P. A., Nolan, M. C., Howell, E. S., Springmann, A., Giorgini, J. D., et al. (2015). A radar survey of M- and X-class asteroids. III. Insights into their composition, hydration state, & structure. *Icarus*, *245*, 38–55. https://doi.org/10.1016/j.icarus.2014.09.016

Shepard, M. K., Richardson, J., Taylor, P. A., Rodriguez-Ford, L. A., Conrad, A., de Pater, I., et al. (2017). Radar observations and shape model of asteroid 16 Psyche. *Icarus*, *281*, 388–403. https://doi.org/10.1016/j.icarus.2016.08.011

Shepard, M. K., de Kleer, K., Cambioni, S., Taylor, P. A., Virkki, A. K., Rívera-Valentin, E. G., et al. (2021). Asteroid 16 Psyche: Shape, Features, and Global Map. *The Planetary Science Journal*, *2*, 125. https://doi.org/10.3847/PSJ/abfdba

Sierks, H., Lamy, P., Barbieri, C., Koschny, D., Rickman, H., Rodrigo, R., et al. (2011). Images of Asteroid 21 Lutetia: A Remnant Planetesimal from the Early Solar System. *Science*, *334*(6055), 487–490. https://doi.org/10.1126/science.1207325

Smyth, J. R., & Mccormick, T. C. (1995). Crystallographic Data for Minerals. In *Mineral Physics & Crystallography* (pp. 1–17). American Geophysical Union (AGU). https://doi.org/10.1029/RF002p0001

Sori, M. M., Landis, M. E., Bapst, J., Bramson, A. M., Byrne, S., Reddy, V., & Shepard, M. K. (2017). Ice Stability on Psyche and Implications for the Planetary Core Hypothesis, *48*, 2550. Presented at the Lunar and Planetary Science Conference.

Takir, D., Reddy, V., Sanchez, J. A., Shepard, M. K., & Emery, J. P. (2016). DETECTION OF WATER AND/OR HYDROXYL ON ASTEROID (16) Psyche. *The Astronomical Journal*, *153*(1), 31. https://doi.org/10.3847/1538-3881/153/1/31

Tarduno, J. A., Cottrell, R. D., Nimmo, F., Hopkins, J., Voronov, J., Erickson, A., et al. (2012). Evidence for a Dynamo in the Main Group Pallasite Parent Body. *Science*, *338*(6109), 939–942. https://doi.org/10.1126/science.1223932

Tholen, D. J. (1984, September). *Asteroid Taxonomy from Cluster Analysis of Photometry.* (PhD Thesis). University of Arizona, Tucson.

Viikinkoski, M., Vernazza, P., Hanuš, J., Le Coroller, H., Tazhenova, K., Carry, B., et al. (2018). (16) Psyche: A mesosiderite-like asteroid? *Astronomy and Astrophysics*, *619*, L3. https://doi.org/10.1051/0004-6361/201834091

Walsh, K. J. (2018). Rubble Pile Asteroids. *Annual Review of Astronomy and Astrophysics*, *56*(1), 593–624. https://doi.org/10.1146/annurev-astro-081817-052013

Yang, J., Goldstein, J. I., & Scott, E. R. D. (2007). Iron meteorite evidence for early formation and catastrophic disruption of protoplanets. *Nature*, *446*, 888–891. https://doi.org/10.1038/nature05735

Yang, J., Goldstein, J. I., & Scott, E. R. D. (2008). Metallographic cooling rates and origin of IVA iron meteorites. *Geochimica et Cosmochimica Acta*, *72*(12), 3043–3061. https://doi.org/10.1016/j.gca.2008.04.009

Yang, J., Goldstein, J. I., Michael, J. R., Kotula, P. G., & Scott, E. R. D. (2010). Thermal history and origin of the IVB iron meteorites and their parent body. *Geochimica et Cosmochimica Acta*, *74*(15), 4493–4506. https://doi.org/10.1016/j.gca.2010.04.011

Figures

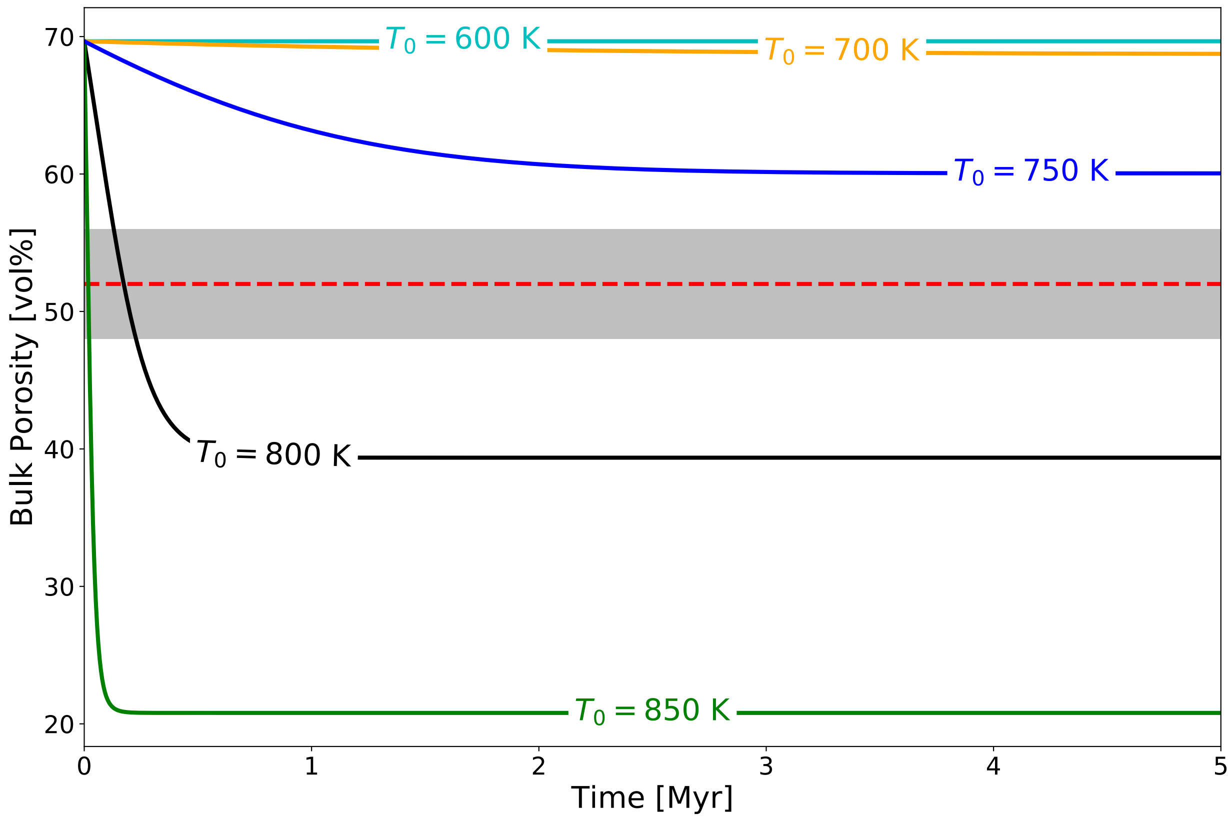

Figure 1. Temporal evolution of bulk porosity for a pure iron Psyche. Initial isothermal temperatures of 600 (cyan), 700 (orange), 750 (blue), 800 (black), and 850 K (green) are shown. The red line denotes the inferred bulk porosity required for a pure iron body to match the Psyche density estimate of 3,780 $\pm$ 340 kg/m^3 (Elkins-Tanton et al., 2020) and gray rectangle denotes the associated $\pm$1-σ error.

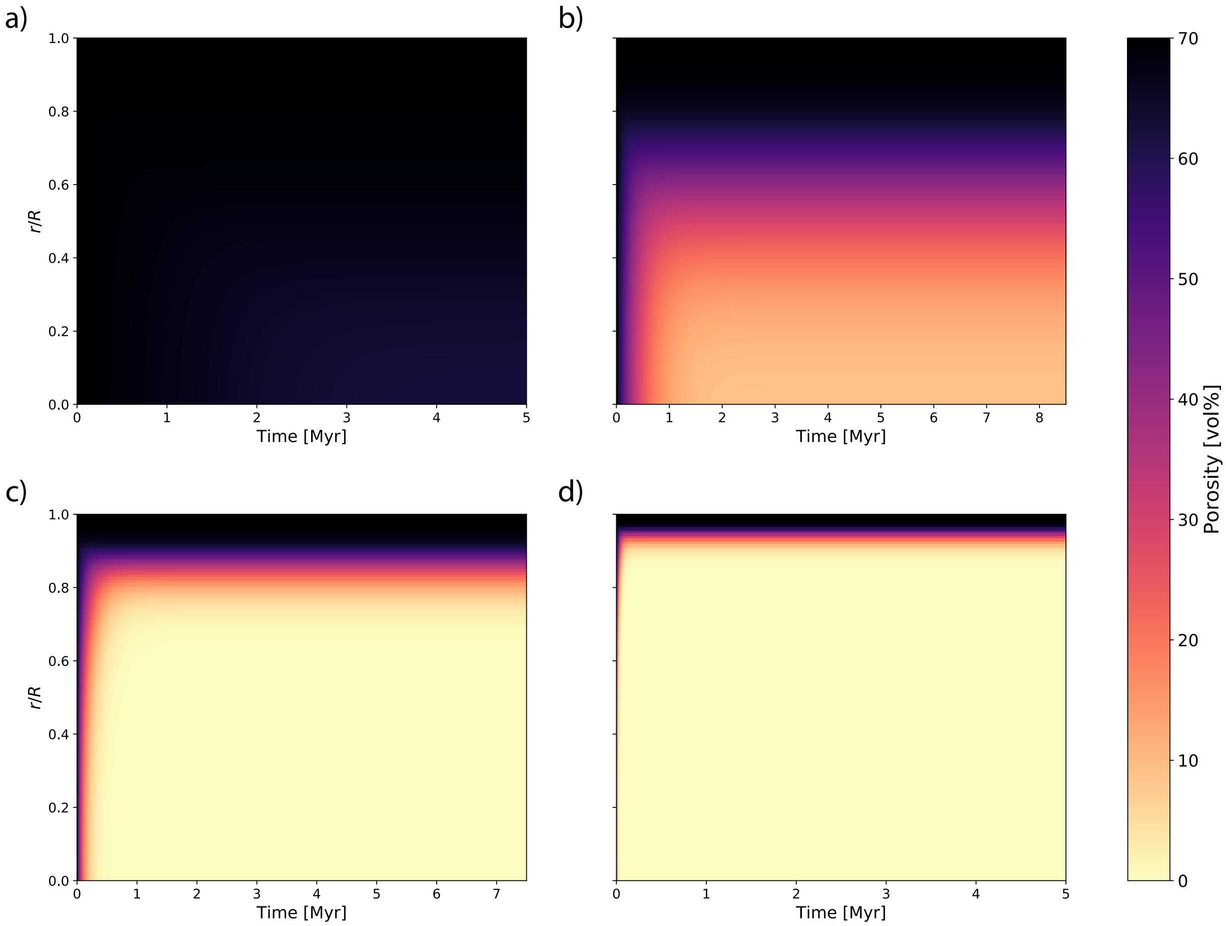

Figure 2. Temporal evolution of porosity with depth for a pure iron Psyche with an initially uniform porosity of 70 vol% and initial isothermal temperature of (a) 700 K, (b), 750 K, (c) 800 K, and (d) 850 K. Final bulk porosities for a,b,c, and d are 68.7, 60.0, 39.4, and 20.8 vol%, respectively.

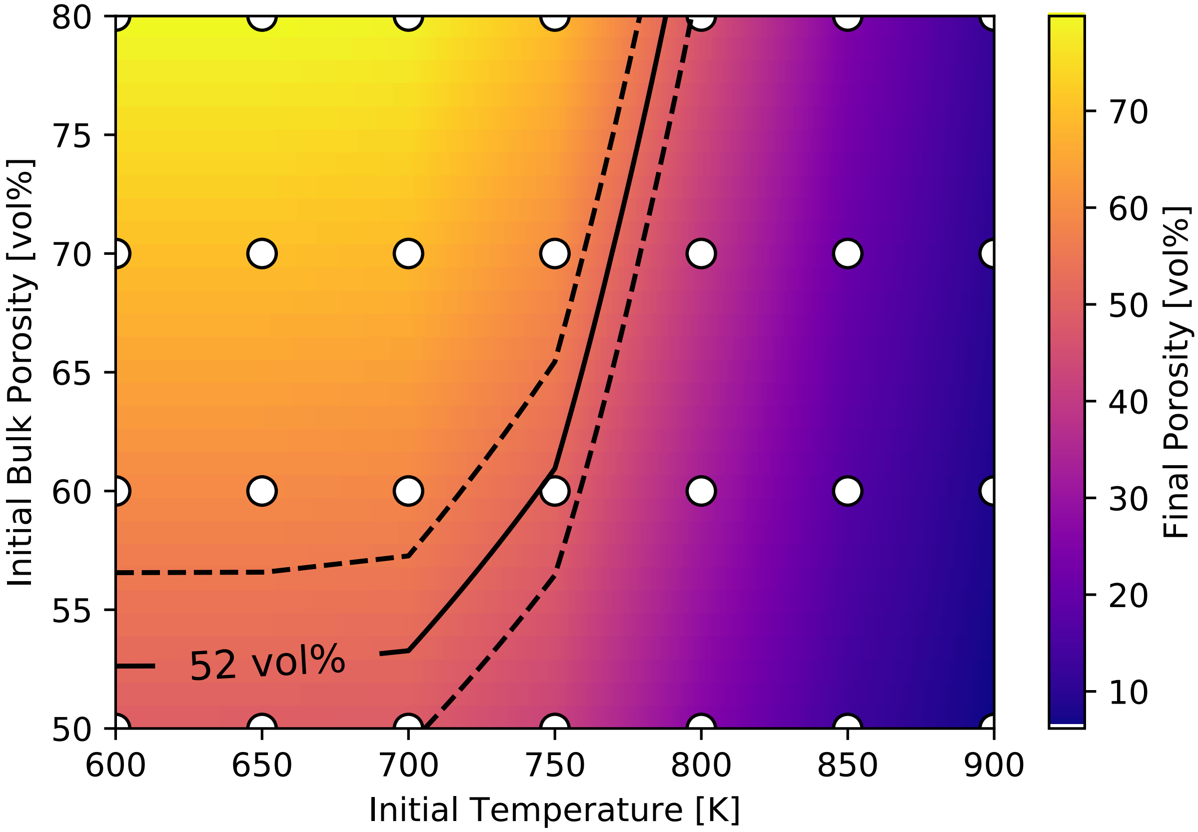

Figure 3. Final bulk porosities for pure iron Psyche models with initially uniform temperatures and porosity profiles. Locations of modeled runs are denoted by white circles. A bilinear interpolation was performed to fill the parameter space between models. The black line delineates the inferred bulk porosity for a pure iron Psyche of 52 vol% and the dashed lines indicate bulk porosities of 48 and 56 vol%, corresponding to the one sigma bounds for a pure iron Psyche based on the errors on Psyche bulk density as determined by Elkins-Tanton et al. (2020).

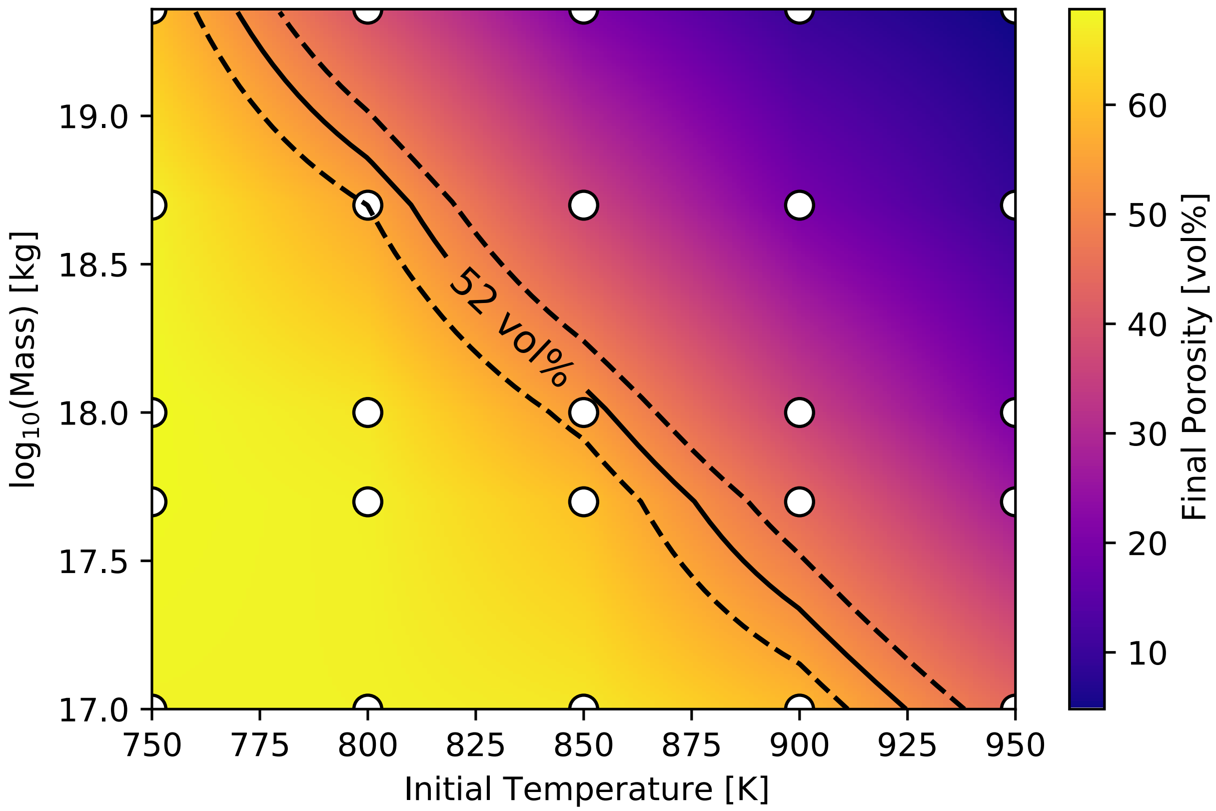

Figure 4. Final bulk porosities for iron bodies with initially uniform temperatures between 750 and 950 K and masses between $10^{17}$and 2×10^{19} kg. In each case the initial uniform porosity is 70 vol%. Symbols and lines are as denoted in Fig. 3.

Supplemental Material

The models of a pure-iron Psyche, as described in Section 2 of the main text, are run with reference viscosities of 10^9 and 10^{13} Pa s. These models are complementary to those with a reference viscosity of 10^{11} Pa s (shown in Figure 2 in the main text) and their range in viscosities is meant to demonstrate the influence of the uncertainty in grain size of the iron. The results of the models with lower and higher reference viscosities are shown in Figures S1 and S2, respectively. For a reference viscosity of 10^9 Pa s, a pure-iron Psyche must cool below ~700 K to retain 52 vol% bulk porosity. For a reference viscosity of 10^{11} Pa s, a higher critical temperature of ~900 K is allowed. As is the case for the models in the main text, these temperatures represent upper limits for the critical temperatures due to the use of Newtonian rheology and the simplified form of the relationship between thermal conductivity and porosity. These results show that changes in grain size that result in viscosity changes up to two orders of magnitude modify critical temperatures by up to 100 K. The discussion of the implications of these cool temperatures in Sections 4 and 5 of the main text holds for these additional models.

Supplemental Figures

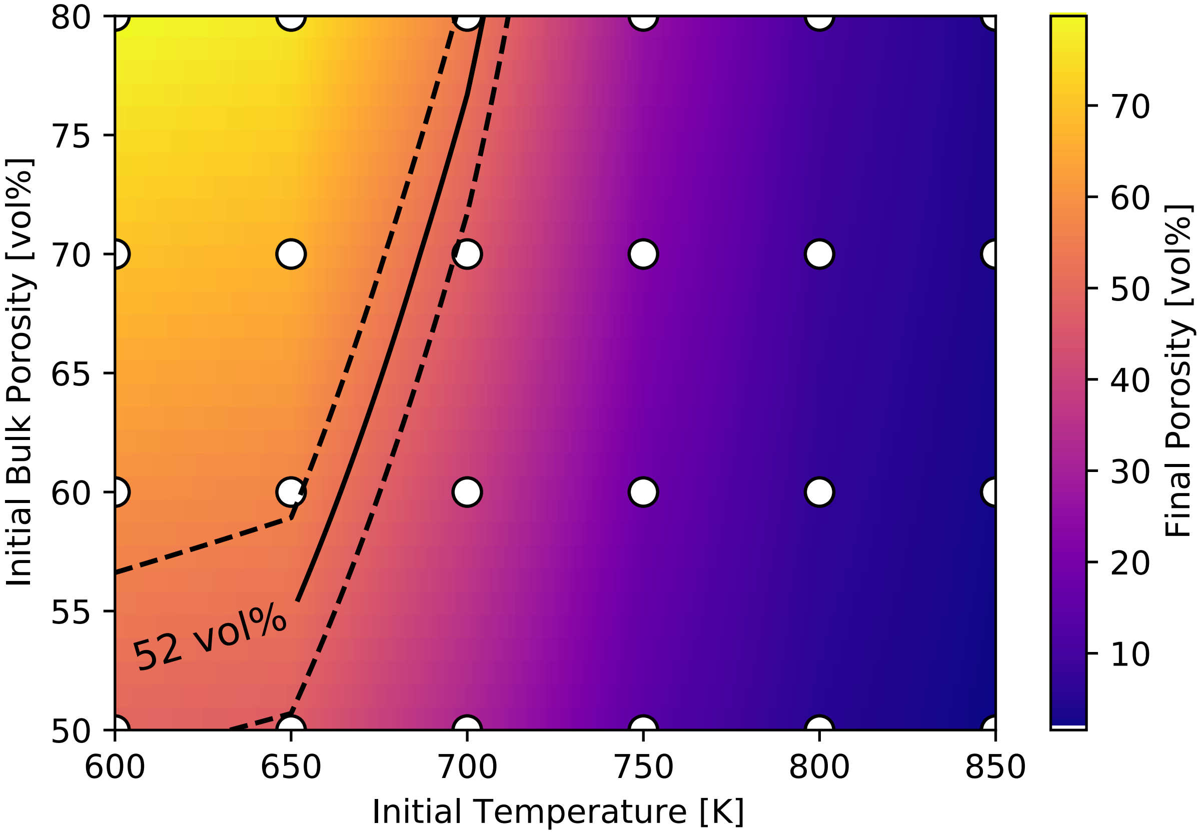

Figure S1. Final bulk porosities for pure iron Psyche models with initially uniform temperatures and porosity profiles and a reference viscosity of 10^9 Pa s. Locations of modeled runs are denoted by white circles. A linear interpolation was performed to fill the parameter space between models. The black line delineates the inferred bulk porosity for a pure iron Psyche of 52 vol% and the dashed lines indicate bulk porosities of 48 and 56 vol%, corresponding to the one sigma bounds for a pure iron Psyche based on the errors on Psyche bulk density as determined by Elkins-Tanton et al. (2020).

Figure S2.

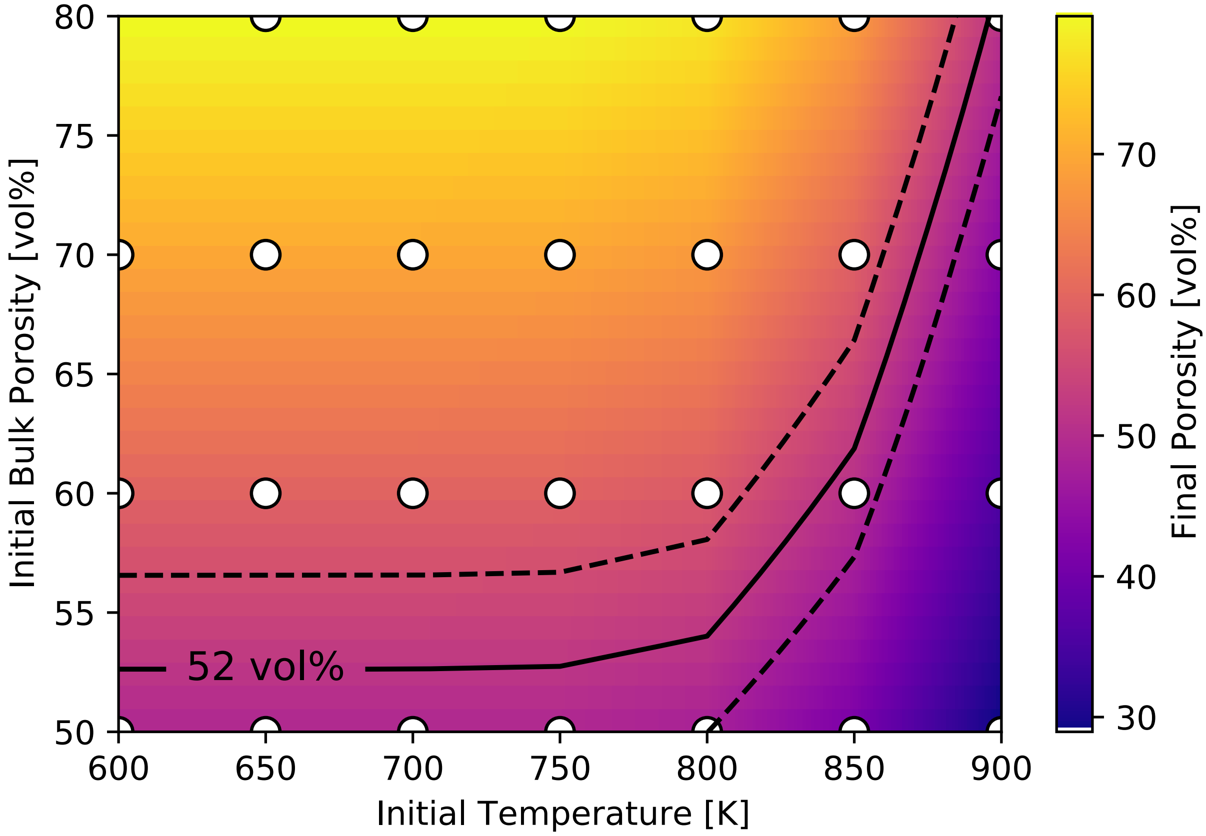

Final bulk porosities for pure iron Psyche models with initially uniform temperatures and porosity profiles and a reference viscosity of 10^{13} Pa s. Symbols and lines are as denoted in Figure S1.

Chapter 4: Moment of Inertia and Tectonic Record of Asteroid 16 Psyche May Reveal Interior Structure and Core Solidification Processes

Fiona Nichols-Fleming[1], Alexander J. Evans[1], Brandon C. Johnson[2,3], and Michael M. Sori[2]

[1]Department of Earth, Environmental and Planetary Sciences, Brown University, Providence, RI

[2]Department of Earth, Atmospheric, and Planetary Sciences, Purdue University, West Lafayette, IN

[3]Department of Physics and Astronomy, Purdue University, West Lafayette, IN

Abstract

The thermal and chemical evolution of 16 Psyche would have been influenced by the direction of core solidification and thickness of an outer (rocky) silicate layer. We model the thermal evolution and core solidification of Psyche for a range of outer silicate layer thicknesses and core sulfur contents to calculate the resulting radial contraction and moments of inertia. We generally find that increasing the thickness of the outer silicate layer by 10 km results in a ~1-km reduction in total radial contraction. Additionally, we find that the timing of full core solidification, and thus a large amount of predicted contraction, can differ by up to 50 Myr for inward versus outward core growth. Finally, our calculated moment-of-inertia factors for models with inward core growth that contain sulfur are consistently larger than those with outward core growth. Ultimately, spacecraft observations of Psyche's moment of inertia and thrust faults at the surface will be able to provide constraints on Psyche's interior evolution, silicate layer thickness, and direction of core solidification.

1 Introduction

The asteroid (16) Psyche (henceforth referred to as Psyche) is the largest of a class of objects throughout the asteroid belt called the M-type asteroids (Shepard et al., 2017). These asteroids are generally classified by their lack of features in visible and near-infrared spectra (Bus & Binzel, 2002; DeMeo et al., 2009; Tholen, 1984) and high radar albedos (Shepard et al., 2008, 2010, 2015, 2017), which suggest that these bodies have metal-rich surfaces. However, existing observations have limited spatial resolution and are largely restricted to the surface (e.g., Elkins-Tanton et al., 2020 and references therein), leaving the formation process and evolution of Psyche largely uncertain. The Psyche mission was designed to address these questions and determine how the asteroid Psyche formed (e.g., Elkins-Tanton et al., 2020, 2022), and complementary modeling efforts are crucial to the interpretation of these planned observations and measurements.

As existing observations of Psyche are limited to bulk properties and the near surface ($\lesssim$ 1 m; e.g., Shepard et al., 2017), Psyche's internal structure and metal mass fraction remain uncertain. Psyche's inferred density from the most recent shape models and mass measurements is $4{,}000 \pm 200$ kg/m^3 (Shepard et al., 2021), equivalent to or lower than the uncompressed densities of Mercury, Venus, and Earth (5,300, 4,000, and 4,050 kg/m^3, respectively; Wieczorek, 2015). Psyche may be a differentiated body with a rocky mantle where iron has been brought to the surface by ferrovolcanism (Johnson et al., 2020) or a core stripped of its mantle from one or more hit-and-run collisions (e.g., Asphaug et al., 2006; Asphaug & Reufer, 2014). Alternatively, Psyche may be an undifferentiated mixture of silicates and metal – a possible parent body to stony-iron meteorites such as mesosiderites (Viikinkoski et al., 2018). However, a recent study suggests that pyroxene signatures observed in mesosiderite samples should be preserved on their parent body, regardless of collisional history, and therefore the very low amount of pyroxene observed on Psyche is inconsistent with a mesosiderite-like composition (Libourel et al., 2023). Another potential composition suggests that Psyche may be purely iron-nickel with a bulk porosity of ~52%, assuming a nominal meteoritic metal composition and density (Elkins-Tanton et al., 2020). However, previous thermal models indicate that a purely porous iron composition for Psyche would require a cold re-accretion ≤ 800 K to retain such a high bulk porosity (Nichols-Fleming et al., 2022). Hence, in this work, we assume that the low bulk density of Psyche is due to the inclusion of some amount of lower density silicate material.

Ultimately, the amount of rocky silicate material within Psyche will influence the thermal evolution of Psyche. For a Psyche-sized body with an effective spherical radius, R_{eff}, of 111 km (Shepard et al., 2021) that is composed of rock and iron, differentiation is likely due to efficient heating by accretion and radioactive decay as long as the material accreted within the first few million years of solar system evolution (e.g., Neumann et al., 2012; Šrámek et al., 2012). Thus, under the assumption that Psyche is an early solar system planetesimal, we expect the rocky material to be separated from the iron in the form of an iron core and a rocky mantle. Models consistent with Psyche's shape and bulk density that assume a differentiated structure find that a silicate outer layer is not well constrained and could reach thicknesses up to 68 km (Kim & Hirabayashi, 2022). This potentially very thick, rocky layer could serve as an insulating blanket for the interior of Psyche due to the lower thermal conductivity of silicates relative to iron (3 and 30 W/m K, respectively; Bierson & Nimmo, 2019; Touloukian et al., 1970), greatly slowing the body's overall cooling process.

Due to the low pressures within Psyche (a central pressure ~100 MPa), core solidification will differ from that of larger planetary bodies. Rather than a solid core nucleating at the center of the core, solid core nucleation will occur at the core-mantle boundary (Williams, 2009). Additionally, analysis of the cooling rates of iron meteorites with varying nickel content indicate that both inward and outward core growth scenarios are possible (Yang et al., 2008, 2010), where outward core growth generates a solid inner core through the accumulation of iron snow and inward core growth proceeds concentrically as shown in Figure 1. Initial sulfur contents up to 18 wt.%, along with other alloying elements, are also expected within the cores of differentiated bodies (e.g., Goldstein et al., 2009). These core sulfur contents will reduce the liquidus of the core (e.g., Ehlers, 1972), and thus delay core solidification and prolong overall cooling of a Psyche mass body. Ultimately, the intricacies associated with the direction of core growth and sulfur content of small, differentiated bodies will influence the thermal evolution of a Psyche mass body as well as the resulting internal structure.

In this work, we determine how observations of Psyche can be used to infer its ancient thermal history. Radial expansion and contraction have historically been used to infer a planetary body's thermal history based on surface observations of pervasive thrust faulting (e.g., Byrne et al., 2014; Solomon, 1977; Solomon & Chaiken, 1976; Watters, 2021). The Psyche spacecraft's planned orbits should provide global imagery and topography with a resolution of ∼15 m/pixel (Jaumann et al., 2022) and thus allow for uniform mapping of any observed faults and estimation of global radius changes. Additionally, the measured gravity field of a body is able to provide constraints on the internal mass distribution. In particular, the moment of inertia (MOI) of a body can be determined from a low-degree spherical harmonic gravity field investigation (e.g., Ceres and Vesta with the Dawn mission; Vaillant et al., 2019). Although the MOI cannot provide a unique solution for the radial density structure of a body, it can be used to estimate the level of differentiation of a body or to distinguish between plausible scenarios for interior structure.

Here, we model Psyche's thermal evolution to determine the relationships between silicate mass fraction, core composition, global contraction, MOI and ancient thermal history. We expand upon the models of Scheinberg et al. (2016) by considering a range of outer silicate layer thicknesses and relating our model results to the observable MOI and record of global contraction on Psyche. We find that silicate layer thickness is the primary control for the total radial contraction experienced by a Psyche mass body with core sulfur content producing minor differences that are unlikely to be independently detected. The direction of core growth influences the early stages of radial contraction within the Psyche mass bodies and results in differences in timing of major contraction and expansion events. Although these timing differences are too small to observe in cases without any core sulfur content, they can extend to ~50 Myr when sulfur is included in the core. Additionally, we find that the MOI for a Psyche that underwent inward core growth is consistently larger than a Psyche that underwent outward core growth. Hence, the difference between inward and outward core growth should be detectable in data acquired by the Psyche spacecraft.

2 Methods

2.1 Thermal Evolution and Solidification Model

To model Psyche's early evolution, we apply a one-dimensional, forward time, central space, finite difference model of thermal conduction in spherical coordinates. We couple our model with the solidification of an initially fluid core overlain by a thin silicate layer. All models are initialized with an outer solid silicate layer at 1300 K and a fluid core at 1820 K. An isothermal core is an appropriate simplification as the temperature difference for the pressure range within the core ($\lesssim$ 100 MPa) is only ~2 K. These temperatures ensure that the silicate layer is solid and reduce the amount of cooling time required for the core temperature to drop below the liquidus for the first time. Therefore, our time zero represents the time at which the outer silicate layer solidifies rather than the formation time of the body. If Psyche underwent a mantle stripping impact event previously, our time zero would represent the time of silicate layer solidification post-mantle stripping event. Additionally, each model has a zero flux central boundary condition as well as a top boundary set to the present-day average Psyche surface temperature of 137 K (Sori et al., 2017). We use a constant radial cell size of 500 m and the spherical radius of each model is calculated such that the modeled mass matches that of Psyche (2.3×10^{19} kg; Elkins-Tanton et al., 2020). Similar to Scheinberg et al. (2016), all models use a simplified core composition of iron and sulfur, with initial core sulfur contents of 0, 1, 5, and 10 wt.%. All material properties used for our models are summarized in Table 1.

Core solidification occurs atop the fluid core because the core adiabat is steeper than the core liquidus for Psyche-sized bodies (Williams, 2009). Thus, when the top of the core cools to the liquidus, solidification begins in the topmost boundary cell. Until the cell is fully solidified, the temperature is held constant at the liquidus and the latent heat released via solidification is balanced by the heat flux at each time step. Hence, for each cell, the volume of iron solidified at each time step is directly limited by the heat flux.

After the topmost boundary cell fully solidifies, models of inward and outward core growth diverge. In the case of inward core growth, once the topmost boundary cell is fully solidified, the cell directly beneath the newly solidified region becomes the topmost boundary cell of the fluid core in the next time step. As the solid outer core progressively grows, the cooling rate of the underlying fluid inner core decreases. In the case of outward core growth, we assume that the solid iron founders to the base of the fluid core on a sufficiently short timescale that can be treated as instantaneous. Upon full solidification of the topmost boundary cell, we convert a number of cells at the base of the fluid core from liquid to solid, where the number of cells is determined such that the mass of solid material is conserved, and the topmost boundary cell is reset to a fully fluid state. This process continues until the core is fully solidified.

Until the core sulfur content reaches the eutectic (31 wt.% sulfur; Ehlers, 1972), all solidifying material is pure iron. Hence, for both inward and outward core growth, the sulfur content of the fluid core and liquidus temperature evolve until the eutectic is reached. We assume that the fluid core is homogeneous and use mass conservation to determine the sulfur content at each timestep using an FeS density expression that depends on the atomic fraction of sulfur, χ

(Morard et al., 2018). After the fluid core reaches the eutectic, the solidifying core material is a eutectic mixture of Fe and FeS with 68.5 wt.% FeS. This eutectic mixture has a different density, latent heat of solidification, and thermal conductivity than pure Fe (see Table 1). Upon full solidification of the core, conductive core and silicate layer cooling proceed until the models conclude at 100 Myr.

Numerical stability of our thermal model is maintained by limiting the timestep Δt to 2% and 20% of the Courant number C (Courant et al., 1967), during and after core solidification, respectively. Using Fourier stability analysis, $C = (\Delta r)^2/2\kappa$ where Δr is the grid size and κ is the thermal diffusivity. Accordingly, our models are capable of resolving sulfur content changes in the fluid core at less than 3.5 wt.% per timestep.

2.2 Calculations of Radial Contraction and Moment of Inertia

We estimate the total planetary contraction

$$\Delta R(t) = \Delta R_{PC}(t) + \sum_{t_i=0}^{n} \Delta R_T(t_i) \tag{1}$$

as a combination of secular cooling ΔR_T and phase changes ΔR_{PC} at each timestep t_i. In this paper, we adopt the sign convention where contraction is considered negative.

The planetary contraction due to secular cooling is

$$\Delta R_T(t_i) = \frac{1}{R^2} \sum_{r_i=0}^{R} \alpha_V(r_i)\, \Delta T(r_i) r_i^2 \Delta r \tag{2}$$

where α_V is the volume coefficient of thermal expansivity and ΔT is the temperature change over the specific interval of time (Solomon & Chaiken, 1976). Although FeS may have a slightly different thermal expansivity than pure iron at relevant pressures ($5 - 12 \times 10^{-5}$ 1/K; (Kusaba et al., 1998; Terranova & de Leeuw, 2017), throughout this work we use a median value of 9.2×10^{-5} 1/K for Psyche's core, representative of pure iron (Anderson & Ahrens, 1994).

The planetary contraction due to the phase change of iron from liquid to solid, as well as the secondary phase change from γ-Fe (austenite) to α-Fe (ferrite) at 1,185 K (Desai, 1986) is calculated as

$$\Delta R_{PC}(t) = R_C - \left(R_C^3 - 3\left[\int \frac{V_{\ell iq} - V_\gamma}{V_\gamma}\, r^2 dr + \int \frac{V_\gamma - V_\alpha}{V_\alpha} r^2\, dr\right]\right)^{1/3} \qquad (3)$$

modified after Solomon (1977), where R_c is the total core radius and $V_{\ell iq}$, V_γ, and V_α are the specific volumes of fluid iron, austenite, and ferrite, respectively. For all timesteps, this radial change is integrated across the region which has undergone one or both phase changes.

In addition, we also calculate principal moments of inertia (MOI) for each of our models. As our models all assume spherical symmetry, the principal MOI value, C, is defined as

$$C = \frac{8\pi}{15}\left[\rho_{inner} r_{icb}^5 + \rho_{outer}\left(r_{cmb}^5 - r_{icb}^5\right) + \rho_m\left(R^5 - r_{cmb}^5\right)\right] \qquad (4)$$

where ρ_{inner}, ρ_{outer}, and ρ_m are the densities of the inner core, outer core, and silicate layer, respectively, r_{icb} is the radius of the inner core, r_{cmb} is the radius of the core-silicate boundary, and R is the planetary radius.

3 Results and Discussion

3.1 Radial Contraction

We modeled Psyche's thermochemical evolution initialized across a range of outer silicate layer thicknesses (1, 10, 20, 30, 40, and 50 km) and initial core sulfur contents (0, 1, 5, and 10 wt.%) for both inward and outward core growth scenarios. As an example, the thermal evolution of a 20-km-thick silicate layer and initial core sulfur content of 5 wt.% is shown in Fig.

2 with inward and outward core growth. For the scenario in Fig. 2, the core fully solidifies over a longer time period for inward core growth (~42 Myr) compared to outward core growth (~4.3 Myr). The rate of secular cooling of the silicate layer is also different between the two models of core growth. In the case of inward core growth, the solid outer core must cool before solidification can proceed. Therefore, the silicate layer cools more in a given period of time compared to outward core growth where the base of the silicate layer remains hotter due to the lack of an insulating solid outer core. Furthermore, the radial position of the solid Fe + FeS layer differs between the two core growth directions as Fe + FeS only crystallizes after the eutectic is reached. In the case of inward core growth, this lower density Fe + FeS layer is at the center of the core while it remains at the top of the core in the outward growth case. This Fe + FeS layer solidifies very quickly in both cases because the sulfur content and therefore the liquidii of the fluid core remain constant through the rest of the solidification process, no longer limiting the rate of core solidification.

Across the ranges of silicate layer thicknesses and initial core sulfur contents considered herein, we find that inward core growth results in consistently longer solidification timescales compared to outward core growth (see Figure 3). As expected, we find that the solidification of a pure iron core occurs much faster than a core with any amount of sulfur content regardless of core growth direction due to the constant liquidus of iron throughout the solidification process. In models that contain sulfur, those with a higher initial sulfur content will reach the eutectic at a faster rate, and therefore the solidification time will be decreased regardless of the direction of core growth. Although the range in solidification times due to variations in sulfur content are largely not visible in the cases of outward core growth, there is variability of approximately the same percentage of the total solidification time as those for inward core growth models.

Additionally, because a thinner silicate layer increases the importance of differences in core evolution, the variations in initial sulfur content have a stronger effect on the solidification time for models with thinner silicate layers regardless of the direction of core growth. While the core growth direction does not influence the starting time of core solidification for our models, we note that the lower liquidii associated with higher initial sulfur contents cause greater delays to the onset of core solidification.

Additionally, we find that there exists a further complexity in the relationship between sulfur content and solidification time due to variation in core size. Since our models are constant in mass, a higher initial sulfur content in the core requires a larger core size which will require more energy loss to cool. This difference in required energy loss for models of constant silicate layer thickness to solidify becomes visible in cases of inward core growth where a higher sulfur content may result in a longer solidification time (e.g., the 5 wt.% case in Figure 3). The behavior is only visible in cases of inward core growth because the core size directly limits heat flux out of the core in these models via the insulating solid outer core.

For all of our models that include sulfur, we also find that thicker silicate layers require longer timescales to reach full core solidification. However, this is not the case for models of pure iron cores. For an iron core, a thicker silicate layer requires a smaller core size to maintain a constant mass and thus less energy is required to complete solidification. This decrease in required energy, along with the competing slower rate at which heat can be lost through a thicker silicate layer, produces a trend where solidification times initially increase and then decrease with increasing silicate thickness. We note that the ratio between solidification timescales for inward to outward core growth models with the same sulfur content are not constant for all silicate layer thicknesses and range between ~5 and ~200. Generally this ratio decreases with thicker silicate layers or lower initial sulfur contents. However, the ratio is much larger for silicate layer thicknesses of 1 km and in these models the ratio also increases for lower sulfur contents. Furthermore, the ratio of solidification times for pure iron models is much larger those that include sulfur for silicate layers thicker than 10 km.

The differences for solidification times determined here are slightly larger than those of Scheinberg et al. (2016). Scheinberg et al. (2016) found solidification times of 10.5 and 0.75 Myr for dendritic inward and concentric outward core growth of a 101-km-radius planetesimal with a 1-km silicate layer and an initial core sulfur content of 6 wt.%, respectively. Our models likely differ from those of Scheinberg et al. (2016) due to their inclusion of fluid dendrites, which can increase the rate of inward core growth. Thus, our solidification timescales for concentric inward core growth (e.g., ~17 Myr for a 1-km silicate layer thickness and a 5 wt.% initial core sulfur content) are longer, producing larger differences between inward and outward core solidification timescales.

The timing of core solidification likely had a significant influence on the timing of geologic activity on Psyche. As previously discussed by Scheinberg et al. (2016), the direction of core growth has a strong influence on asteroidal magnetic fields. Similar to Scheinberg et al. (2016), our findings suggest that, for all cases of inward core growth, portions of the solid outer core cool through the Curie temperature (1,043 K) while a liquid inner core is present. Thus, if the liquid inner core generated a dynamo, a record of an ancient Psyche dynamo may be recorded in the outer core. However, for outward core growth, core solidification occurs too quickly for the solid portions of the core to reach the Curie temperature when a fluid outer core still exists, and any potential internally-generated magnetic field would therefore have to be recorded by the overlying silicate layer. Additionally, our results suggests that a Psyche with inward core growth may have had a longer period of geologic activity than with the same initial conditions and outward core growth.

The solidification times of our models also suggest that mantle-stripping and disruptive impact events, if they occurred in Psyche's history, would likely have happened while the core was still at least partially fluid. The hit-and-run collisions theorized to be able to strip a large portion of mantle off of a planetesimal (e.g., Asphaug et al., 2006) occur only during the accretionary stage of planetary formation ($\lesssim$1.5 Myr post-CAI formation; Yang et al., 2007) and therefore would occur during the process of core solidification in most cases modeled here. Fully disruptive impact events can occur throughout a longer period of solar system evolution, up to 10 Myr post-CAI formation based on the disruption of ordinary chondrite parent bodies at their peak temperatures (Bouvier et al., 2007; Lucas et al., 2020), or possibly even later based on micro-structures within type IVA iron meteorites as discussed in Zhang et al. (2022). These events may therefore occur post-core solidification for models with outward core growth, but are unlikely to occur after the 40 – 50 Myr required for models of inward core growth with silicate layer thickness in excess of 20 km. In the cases where a disruptive impact could occur after the full solidification of the core, little to no record of Psyche's early thermal evolution may be preserved at the surface. However, if the disruption occurs while the core is at least partially fluid, we would still expect to see a tectonic record of the final portion of core solidification and cooling. Due to uncertainties in the re-accretion process and the likelihood of a spherically asymmetric material distribution post-disruption, detailed models of a disrupted Psyche are left to future work.

The planetary contraction history with silicate layer thicknesses of 1, 10, 20, and 50 km and initial core sulfur contents of 0 and 5 wt.% are shown in Figure 4a and 4b, respectively. For reference, Figure 4a also contains a pure iron model with a porosity of 52 vol% and an initial temperature of 600 K (i.e., Nichols-Fleming et al., 2022). Since the full solidification of the core takes under 3 Myr for our sulfur-free models, contraction due to the liquid to γ-Fe phase change is not visible on the 100 Myr scale in Figure 4a. Thus the change in radius for these bodies generally follows the thermal contraction associated with the cooling body. An increasing thickness of the outer silicate layer requires a smaller core size and therefore a smaller volume of material undergoing the liquid to solid phase change. Consequently, thicker silicate layers produce smaller total magnitudes of contraction. An inflection point in the radial contraction history around 20 Myr for the model with a 50 km thick silicate layer (Figure 4a) marks a late period of expansion due to the secondary phase change of iron from γ-Fe to α-Fe (Desai, 1986). Although not shown in Figure 4a, this expansion is also visible in our models with 30 and 40 km silicate layers and a pure iron core composition. While this phase change occurs in the core of all models, it is not seen in the thinner silicate layer models ($\lesssim$ 20 km) because the cooling occurs at a sufficiently fast rate that the thermal contraction is larger than expansion caused by the γ-Fe to α-Fe transition. While a late period of expansion may still be visible for models with silicate layers $\gtrsim$ 20 km that contain sulfur, it is greatly suppressed due to the rapid solidification of the eutectic mixture at about the same temperature as the γ-Fe to α-Fe transition and the thermal contraction of the solid outer core in cases with inward core growth.

Without sulfur in the core, the direction of core growth does not have a significant impact on the change in radius of a body (e.g., Fig. 4a). However, when sulfur is included in the core, the liquidus is lowered thereby greatly increasing the time for full core solidification (e.g., Fig. 3). Thus, as shown in Fig. 4b, the differences between inward and outward core growth, as they approach the same final radius, are readily discernible. Additionally, a rapid period of contraction can be seen in the models in Fig. 4b, for example around 55 Myr for the model with inward core growth and a 50 km thick silicate layer. This steep drop in radius is due to a period of more rapid core solidification that occurs when the eutectic is reached. At this point the liquidus remains constant and the rate of core solidification is no longer limited by the decreasing of the liquidii with the evolving sulfur content. This period of core evolution is reached later in cases of inward core growth due to the insulating effect of the solid outer core. The thermal contraction due to the simultaneous cooling of the solid outer core also causes this rapid period of contraction to appear larger for cases of inward core growth. The differences in timing of the steep decrease in radius and the late period of expansion for inward and outward core growth increases with increasing silicate layer thickness up to ~50 Myr for our modeled bodies with silicate layer thicknesses of 50 km. Additional variation in this timing due to different initial sulfur contents is limited to ~4 million years.

Regardless of initial core sulfur content, the magnitude of the total radial contraction experienced by Psyche is primarily determined by the thickness of the outer silicate layer, with thicker layers producing lesser amounts of radial contraction. Generally, the addition of a ~10-km-thick silicate layer atop the core reduces the final magnitude of contraction by ~1 km. Variations in core sulfur content produce a modest effect on radial contraction due to increasing core sizes with increasing sulfur content, producing differences on total change in radius $\lesssim$ 300 m. Additionally, for all core sulfur contents we consider, the thickest outer silicate layer case (50 km) has ~2.5 km of contraction, similar that of a porous iron Psyche (~1.6 km). Our result here suggests that a differentiated Psyche with a thick silicate layer (> 50 km) overlying its core may be indistinguishable from a porous iron body using radial contraction estimates alone.

For bodies that experience large amounts of radial contraction, widespread thrust faults can be used to infer the extent of radial contraction experienced by the body. To estimate the extent of thrust faulting we might expect for each of our models, we calculate the linear and areal strains associated with the final radius change for each model, which are 0.02 – 0.06 and 0.04–0.13, respectively. The associated stress from a global change in radius depends on the linear strain and is given by

$$\sigma = \frac{E}{(1-\nu)}\varepsilon \tag{5}$$

where we use a Young's Modulus $E = 80$ GPa and a Poisson's ratio $\nu = 0.25$, typical of a rocky lithosphere following Watters & Nimmo (2009). Therefore, the total radius changes calculated from our models correspond to stresses between 2.4 and 7 GPa, which are over an order of magnitude larger than the compressive strength of granite (~130 MPa; e.g., Stowe, 1969; Villeneuve et al., 2018). Additionally, when assuming a fault plane dip of 30° and a displacement to fault length ratio $\gamma = 7 \times 10^{-3}$ (consistent with faults on Mercury; e.g., Watters, 2021), we can estimate the number of faults of a given length scale expected from our models' areal strain via

$$N = \frac{\varepsilon\, A}{\gamma\, L^2 \sin 30°} \tag{6}$$

where A is the body's surface area and L is the fault length. The areal strains of 0.04 – 0.13 predict ~12 to ~60 thousand faults with a length of 10 km and therefore a displacement of 70 m. If we instead assume a fault length of 100 km, these strains could be accommodated by 200 – 400 faults each with 700 m of displacement. Regardless of fault length, the larger number of faults are expected for the case of a 1 km thick silicate layer and vice versa for the 50 km thick silicate layer. Across all fault types on Earth, displacement to length ratios may vary from

$\sim 5 \times 10^{-3} - 10^{-1}$ (e.g., Cowie & Scholz, 1992 and references therein) due to differences in rock type and tectonic state. Using the maximum ratio observed for Earth, we would expect the previously discussed displacements to be reduced by a factor of ~10 and therefore the number of predicted faults to accommodate the modeled strain would increase by a factor of 10. Thus, we expect numerous faults to have formed due to predicted changes in radius if Psyche is an undisrupted, differentiated body. Furthermore, if the surface ages of regions of contractional faults are known to an accuracy greater than ~50 Myr, the age of that contraction could be used to distinguish the direction of core solidification. Alternatively, if a lack of thrust faults are observed by the Psyche spacecraft, this could suggest that Psyche formed via cool re-accretion of iron with high porosity or that the surface is younger than our predicted ancient contraction. This young surface age could be due to a mantle-stripping or full disruption event, but the event would need to occur after the solidification of the core to prevent ongoing radius changes due to portions of the core solidifying after re-accretion. A disruption event mid-core solidification would remove the record of any earlier contractional features and therefore reduce the final observed magnitude of contraction relative to an undisrupted body with the same silicate layer thickness. Overall, the analysis of Psyche's contractional history can be used to help break the non-uniqueness of planned measurements of the Psyche spacecraft such as the gravity field and the electrical conductivity.

3.2 Internal Structure and Moment of Inertia

The moment of inertia (MOI) is a measure of the resistance to rotation of a body about a particular axis and is dependent on the distribution of mass within that body. Generally, higher values of the MOI indicate mass concentrated farther from the rotation axis and vice versa for lower MOI values. The MOI factor, defined as C/MR^2, is a dimensionless quantity that specifically represents the radial distribution of mass within a body where again a higher value indicates mass concentration farther from the center of the body. A value of 0.4 is representative of a uniform sphere, therefore the extent to which the MOI factor is below 0.4 may also indicate the level of differentiation of a body.

The radial position of a eutectic layer will be different for cases of inward and outward core growth (e.g., Figure 2), and therefore we expect there to be a difference in the moment of inertia for bodies of the same mass that have undergone these different core solidification processes. The principal MOI of each of our models is calculated following the process described in Section 2.2 and the values of the MOI factor for initial core sulfur contents of 1, 5, and 10 wt.% are shown for all of the silicate layer thicknesses in this work in Figure 5a along with a horizontal line indicating the expected value of a uniform density sphere. Our results indeed show that models of inward core growth consistently have higher MOI factors than those that include outward core growth due to the denser composition of their solid outer cores. A thicker silicate layer reduces the size of the core and adds more material at a lower density than the core. Therefore, increasing the silicate layer thickness generally decreases the MOI factor. A higher initial core sulfur content, however, results in a larger initial core volume as well as a thicker eutectic layer within the core. Therefore, models with higher initial core sulfur contents also generally have higher MOI factors.

Further complexity is also seen in the relationship with MOI factor at high silicate layer thicknesses. After a critical thickness (~30 km), the silicate layer becomes the dominant fraction of the body. This dominant layer has a constant density, therefore at high silicate layer thicknesses, there is an uptick in MOI factor. This behavior is seen for a majority of the models shown in Figure 5a, but variations in the critical layer thickness exist for different core sulfur contents.

Figure 5b shows the differences in the MOI factor between inward and outward core growth for the models from Figure 5a. The Psyche mission's gravity investigation is designed based on experience from the Dawn mission to Ceres and Vesta (e.g., Zuber et al., 2022), thus for comparison the uncertainty in the MOI factors for Ceres and Vesta (0.005 and 0.013, respectively; Vaillant et al., 2019) are indicated in Figure 5b with blue and red dashed lines, respectively. For thicker silicate layers, core sizes are smaller and therefore the influence of the two-layered core structure on the MOI is decreased. This results in decreasing differences between MOI factors for increasing silicate layer thicknesses. Alternatively, higher initial sulfur contents require larger core sizes and therefore result in a stronger influence of the two-layer core structure. Therefore, there is generally a larger difference in MOI factor between inward and outward core growth scenarios with increasing initial core sulfur content. The variations due to our range of sulfur contents appears smaller for thicker silicate layers, but represents a similar percentage of the average difference between inward and outward MOI factors for all modeled silicate layer thicknesses. Regardless of initial core sulfur content, the difference between MOI factors for inward and outward core growth remains above the uncertainty in Vesta and Ceres' MOI factors for silicate layer thicknesses $\lesssim 30$ km and $\lesssim 40$ km, respectively. It is important to note that these results hold only in the case of an undisrupted body, as catastrophic impact events may change positions of solidified materials within a body or trigger an overturn of the gravitationally unstable density structure resulting from inward core growth.

Overall, the differences in MOI factor due to the direction of core growth suggest that the Psyche mission's gravity investigation should be able to distinguish which process occurred in

Psyche's early evolution. The addition of further alloying elements in the core such as carbon and nickel will increase these differences in MOI factor as long as they are incompatible. For these alloys, the difference in density between the inner and outer cores will be larger and therefore the influence of the different radial positions of the denser layer will be more significant. However, our modeled cases of core solidification are end-member scenarios and true core solidification processes may progress dendritically inward as described in Scheinberg et al. (2016) or there may be inward and outward core growth occurring simultaneously. In these cases we would expect the density contrast between the two core layers to be reduced and thus the difference in MOI factors to be reduced as well. If solidification progresses dendritically inward, we may also expect ferrovolcanic activity to occur, which would bring FeS into the outer silicate layer or even onto the surface (Johnson et al., 2020). This would reduce the differences between concentric and dendritic inward solidification scenarios as the outer core would have a bulk composition closer to pure iron, but this process would also increase the density of the silicate layer. However, it is unlikely that enough material would experience ferrovolcanism to dramatically influence the MOI values. Additionally, variations in silicate layer composition themselves will change the absolute value of the MOI, as a lower density silicate layer will reduce the silicate layer's contribution to the MOI. However, a lower density silicate layer will also require a larger core volume to match Psyche's mass, which will increase the differences between MOI factors for inward and outward core solidification. The opposite is expected to be true for a higher density silicate layer composition. Due to the uncertainties in true core composition as well as the core solidification process, we leave more detailed considerations of these competing effects to future work.

While our models are all one-dimensional, and thus assume spherical symmetry, Psyche's true shape is triaxial ($278 \times 238 \times 171$ km; Shepard et al., 2021). We can estimate how the MOI ratios may change for an oblate spheroid shaped body by using the constant total body volume from our models and Psyche's aspect ratio of 171:278 (Shepard et al., 2021). We calculate the MOI ratios for two end-member layer shapes within an oblate spheroid shaped body: (1) a spherical core with radii derived by our models overlayed by an ellipsoidal silicate layer, and (2) an ellipsoidal core and silicate layer with constant layer thicknesses as derived by our models. In the case of a spherical core, models with silicate layer thicknesses ≤ 20 km have the model-defined core-silicate boundary larger than the semi-minor axis of the calculated ellipsoid of the same total volume. For these models we use the semi-minor axes as the core-silicate boundary, and therefore lose some volume of the outer core. For the ellipsoidal core calculations, increasing volumes of both the inner and outer core are lost with lower initial sulfur contents and higher silicate layer thicknesses. Therefore, these estimates should be understood simply as approximations and not an ideal conversion to the non-spherical shape of Psyche. The resulting MOI ratio values from ellipsoids with spherical and ellipsoidal core shapes are changed by 0.01 – 0.07 and 0.0001 – 0.02, respectively. However, the differences between these values for inward vs outward core growth in each case are reduced by $\lesssim 0.03$ (Supplemental Figures 1 and 2). Thus, the difference in MOI factor between inward and outward core growth likely remains observable for the triaxial shape of Psyche.

4 Conclusions

The modern, observable surface and interior structure of Psyche will allow us to see back in time to its ancient past and early thermal evolution. Based on our spherical, one-dimensional thermal models, we conclude that

- Measured change in radius from thrust faults, if observed on Psyche's surface, can provide an independent constraint on the thickness of Psyche's outer silicate layer and break non-uniqueness in observations from the Psyche spacecraft.
- The timing of the majority of contractional and extensional features, if present, may be able to differentiate inward and outward core solidification direction if surface ages are known to greater than ~50 Myr precision and sulfur was present in the core.
- A lack of observed thrust faults may suggest that Psyche underwent a cool re-accretion with high porosity and an iron composition or that Psyche's surface is younger than our predicted ancient tectonism.
- The moment of inertia measured by the Psyche spacecraft should be able to determine the direction of solidification of Psyche's core if Psyche is an undisrupted, differentiated planetesimal.

References

Ahrens, T. J., Holland, K. G., & Chen, G. Q. (2002). Phase diagram of iron, revised-core temperatures. *Geophysical Research Letters*, *29*(7), 54-1-54–4. https://doi.org/10.1029/2001GL014350

Anderson, W. W., & Ahrens, T. J. (1994). An equation of state for liquid iron and implications for the Earth's core. *Journal of Geophysical Research: Solid Earth*, *99*(B3), 4273–4284. https://doi.org/10.1029/93JB03158

Asphaug, E., & Reufer, A. (2014). Mercury and other iron-rich planetary bodies as relics of inefficient accretion. *Nature Geoscience*, *7*, 564–568. https://doi.org/10.1038/ngeo2189

Asphaug, E., Agnor, C. B., & Williams, Q. (2006). Hit-and-run planetary collisions. *Nature*, *439*, 155–160. https://doi.org/10.1038/nature04311

Bierson, C. J., & Nimmo, F. (2019). Using the density of Kuiper Belt Objects to constrain their composition and formation history. *Icarus*, *326*, 10–17. https://doi.org/10.1016/j.icarus.2019.01.027

Bouvier, A., Blichert-Toft, J., Moynier, F., Vervoort, J. D., & Albarède, F. (2007). Pb–Pb dating constraints on the accretion and cooling history of chondrites. *Geochimica et Cosmochimica Acta*, *71*(6), 1583–1604. https://doi.org/10.1016/j.gca.2006.12.005

Bus, S. J., & Binzel, R. P. (2002). Phase II of the Small Main-Belt Asteroid Spectroscopic Survey: A Feature-Based Taxonomy. *Icarus*, *158*(1), 146–177. https://doi.org/10.1006/icar.2002.6856

Byrne, P. K., Klimczak, C., Celâl Şengör, A. M., Solomon, S. C., Watters, T. R., & Hauck, I. I. (2014). Mercury's global contraction much greater than earlier estimates. *Nature Geoscience*, *7*(4), 301–307. https://doi.org/10.1038/ngeo2097

Chase, M. W., Jr. (1998). NIST-JANAF thermochemical tables, 4th edition. *Journal of Physical and Chemical Reference Data*, *9*, 1–1951.

Courant, R., Friedrichs, K., & Lewy, H. (1967). On the Partial Difference Equations of Mathematical Physics. *IBM Journal of Research and Development*, *11*, 215–234. https://doi.org/10.1147/rd.112.0215

Cowie, P. A., & Scholz, C. H. (1992). Displacement-length scaling relationship for faults: data synthesis and discussion. *Journal of Structural Geology*, *14*(10), 1149–1156. https://doi.org/10.1016/0191-8141(92)90066-6

DeMeo, F. E., Binzel, R. P., Slivan, S. M., & Bus, S. J. (2009). An extension of the Bus asteroid taxonomy into the near-infrared. *Icarus*, *202*(1), 160–180. https://doi.org/10.1016/j.icarus.2009.02.005

Desai, P. D. (1986). Thermodynamic Properties of Iron and Silicon. *Journal of Physical and Chemical Reference Data*, *15*(3), 967–983. https://doi.org/10.1063/1.555761

Ehlers, E. G. (1972). *The Interpretation of Geological Phase Diagrams*. W. H. Freeman.

Elkins-Tanton, L. T., Asphaug, E., Bell, J. F., Bercovici, H., Bills, B., Binzel, R., et al. (2020). Observations, Meteorites, and Models: A Preflight Assessment of the Composition and Formation of (16) Psyche. *Journal of Geophysical Research (Planets)*, *125*, e06296. https://doi.org/10.1029/2019JE006296

Elkins-Tanton, L. T., Asphaug, E., Bell, J. F., Bierson, C. J., Bills, B. G., Bottke, W. F., et al. (2022). Distinguishing the Origin of Asteroid (16) Psyche. *Space Science Reviews*, *218*(3), 17. https://doi.org/10.1007/s11214-022-00880-9

Fulton, C. H. (1910). *Principles of Metallurgy: An Introduction to the Metallurgy of the Metals*. McGraw-Hill book Company.

Goldstein, J. I., Scott, E. R. D., & Chabot, N. L. (2009). Iron meteorites: Crystallization, thermal history, parent bodies, and origin. *Chemie Der Erde / Geochemistry*, *69*, 293–325. https://doi.org/10.1016/j.chemer.2009.01.002

Helffrich, G. (2017). Mars core structure—concise review and anticipated insights from InSight. *Progress in Earth and Planetary Science*, *4*(1), 24. https://doi.org/10.1186/s40645-017-0139-4

Jaumann, R., Bell, J. F., Polanskey, C. A., Raymond, C. A., Aspaugh, E., Bercovici, D., et al. (2022). The Psyche Topography and Geomorphology Investigation. *Space Science Reviews*, *218*(2), 7. https://doi.org/10.1007/s11214-022-00874-7

Johnson, B. C., Sori, M. M., & Evans, A. J. (2020). Ferrovolcanism on metal worlds and the origin of pallasites. *Nature Astronomy*, *4*(1), 41–44. https://doi.org/10.1038/s41550-019-0885-x

Kim, Y., & Hirabayashi, M. (2022). A Numerical Approach Using a Finite Element Model to Constrain the Possible Interior Layout of (16) Psyche. *The Planetary Science Journal*, *3*(5), 122. https://doi.org/10.3847/PSJ/ac6b39

Kusaba, K., Syono, Y., Kikegawa, T., & Shimomura, O. (1998). High pressure and temperature behavior of FeS. *Journal of Physics and Chemistry of Solids*, *59*(6), 945–950. https://doi.org/10.1016/S0022-3697(98)00015-8

Libourel, G., Beck, P., Nakamura, A. M., Vernazza, P., Ganino, C., & Michel, P. (2023). V-type Asteroids as the Origin of Mesosiderites. *The Planetary Science Journal*, *4*(7), 123. https://doi.org/10.3847/PSJ/ace114

Lucas, M. P., Dygert, N., Ren, J., Hesse, M. A., Miller, N. R., & McSween, H. Y. (2020). Evidence for early fragmentation-reassembly of ordinary chondrite (H, L, and LL) parent bodies from REE-in-two-pyroxene thermometry. *Geochimica et Cosmochimica Acta*, *290*, 366–390. https://doi.org/10.1016/j.gca.2020.09.010

Miettinen, J. (1997). Calculation of solidification-related thermophysical properties for steels. *Metallurgical and Materials Transactions B*, *28*(2), 281–297. https://doi.org/10.1007/s11663-997-0095-2

Morard, G., Bouchet, J., Rivoldini, A., Antonangeli, D., Roberge, M., Boulard, E., et al. (2018). Liquid properties in the Fe-FeS system under moderate pressure: Tool box to model small planetary cores. *American Mineralogist*, *103*. https://doi.org/10.2138/am-2018-6405

Neumann, W., Breuer, D., & Spohn, T. (2012). Differentiation and core formation in accreting planetesimals. *Astronomy & Astrophysics*, *543*, A141. https://doi.org/10.1051/0004-6361/201219157

Nichols-Fleming, F., Evans, A. J., Johnson, B. C., & Sori, M. M. (2022). Porosity Evolution in Metallic Asteroids: Implications for the Origin and Thermal History of Asteroid 16 Psyche. *Journal of Geophysical Research: Planets*, *127*(2), e2021JE007063. https://doi.org/10.1029/2021JE007063

Scheinberg, A., Elkins-Tanton, L. T., Schubert, G., & Bercovici, D. (2016). Core solidification and dynamo evolution in a mantle-stripped planetesimal. *Journal of Geophysical Research (Planets)*, *121*, 2–20. https://doi.org/10.1002/2015JE004843

Shepard, M. K., Clark, B. E., Nolan, M. C., Howell, E. S., Magri, C., Giorgini, J. D., et al. (2008). A radar survey of M- and X-class asteroids. *Icarus*, *195*(1), 184–205. https://doi.org/10.1016/j.icarus.2007.11.032

Shepard, M. K., Clark, B. E., Ockert-Bell, M., Nolan, M. C., Howell, E. S., Magri, C., et al. (2010). A radar survey of M- and X-class asteroids II. Summary and synthesis. *Icarus*, *208*(1), 221–237. https://doi.org/10.1016/j.icarus.2010.01.017

Shepard, M. K., Taylor, P. A., Nolan, M. C., Howell, E. S., Springmann, A., Giorgini, J. D., et al. (2015). A radar survey of M- and X-class asteroids. III. Insights into their composition, hydration state, & structure. *Icarus*, *245*, 38–55. https://doi.org/10.1016/j.icarus.2014.09.016

Shepard, M. K., Richardson, J., Taylor, P. A., Rodriguez-Ford, L. A., Conrad, A., de Pater, I., et al. (2017). Radar observations and shape model of asteroid 16 Psyche. *Icarus*, *281*, 388–403. https://doi.org/10.1016/j.icarus.2016.08.011

Shepard, M. K., de Kleer, K., Cambioni, S., Taylor, P. A., Virkki, A. K., Rívera-Valentin, E. G., et al. (2021). Asteroid 16 Psyche: Shape, Features, and Global Map. *The Planetary Science Journal*, *2*, 125. https://doi.org/10.3847/PSJ/abfdba

Solomon, S. C. (1977). The relationship between crustal tectonics and internal evolution in the moon and Mercury. *Physics of the Earth and Planetary Interiors*, *15*(2), 135–145. https://doi.org/10.1016/0031-9201(77)90026-7

Solomon, S. C., & Chaiken, J. (1976). Thermal expansion and thermal stress in the moon and terrestrial planets: clues to early thermal history. *Lunar and Planetary Science Conference Proceedings*, *3*, 3229–3243.

Sori, M. M., Landis, M. E., Bapst, J., Bramson, A. M., Byrne, S., Reddy, V., & Shepard, M. K. (2017). Ice Stability on Psyche and Implications for the Planetary Core Hypothesis, *48*, 2550. Presented at the Lunar and Planetary Science Conference.

Šrámek, O., Milelli, L., Ricard, Y., & Labrosse, S. (2012). Thermal evolution and differentiation of planetesimals and planetary embryos. *Icarus*, *217*(1), 339–354. https://doi.org/10.1016/j.icarus.2011.11.021

Stowe, R. L. (1969). *Strength and deformation properties of granite, basalt, limestone, and tuff at various loading rates* (Report). *This Digital Resource was created from scans of the Print Resource.* Concrete Laboratory (U.S.). Retrieved from https://erdc-library.erdc.dren.mil/jspui/handle/11681/11425

Terranova, U., & de Leeuw, N. H. (2017). Phase stability and thermodynamic properties of FeS polymorphs. *Journal of Physics and Chemistry of Solids*, *111*, 317–323. https://doi.org/10.1016/j.jpcs.2017.07.033

Tholen, D. J. (1984, September). *Asteroid Taxonomy from Cluster Analysis of Photometry.* (PhD Thesis). University of Arizona, Tucson.

Touloukian, Y. S., Powell, R. W., Ho, C. Y., & Klemens, P. G. (1970). *Thermophysical properties of matter - the TPRC data series. Volume 1. Thermal conductivity - metallic elements and alloys. (Reannouncement). Data book* (No. AD-A-951935/6/XAB). Purdue Univ., Lafayette, IN (United States). Thermophysical and Electronic Properties Information Center. Retrieved from https://www.osti.gov/biblio/5447756-thermophysical-properties-matter-tprc-data-series-volume-thermal-conductivity-metallic-elements-alloys-reannouncement-data-book

Turcotte, D. L., & Schubert, G. (2002). Geodynamics - 2nd Edition. *Geodynamics - 2nd Edition, by Donald L. Turcotte and Gerald Schubert, Pp. 472. Cambridge University Press, April 2002. ISBN-10: 0521661862. ISBN-13: 9780521661867. LCCN: QE501 .T83 2002*. https://doi.org/10.2277/0521661862

Vaillant, T., Laskar, J., Rambaux, N., & Gastineau, M. (2019). Long-term orbital and rotational motions of Ceres and Vesta. *Astronomy & Astrophysics*, *622*, A95. https://doi.org/10.1051/0004-6361/201833342

Viikinkoski, M., Vernazza, P., Hanuš, J., Le Coroller, H., Tazhenova, K., Carry, B., et al. (2018). (16) Psyche: A mesosiderite-like asteroid? *Astronomy and Astrophysics*, *619*, L3. https://doi.org/10.1051/0004-6361/201834091

Villeneuve, M. C., Heap, M. J., Kushnir, A. R. L., Qin, T., Baud, P., Zhou, G., & Xu, T. (2018). Estimating in situ rock mass strength and elastic modulus of granite from the Soultz-sous-Forêts geothermal reservoir (France). *Geothermal Energy*, *6*(1), 11. https://doi.org/10.1186/s40517-018-0096-1

Watters, T. R. (2021). A case for limited global contraction of Mercury. *Communications Earth & Environment*, *2*(1), 1–9. https://doi.org/10.1038/s43247-020-00076-5

Watters, T. R., & Nimmo, F. (2009). *The Tectonics of Mercury*. *Planetary Tectonics (Cambridge Planetary Science) Edited by Thomas R. Watters and Richard A. Schultz* (pp. 15–80). https://doi.org/10.1017/CBO9780511691645.003

Wieczorek, M. A. (2015). 10.05 - Gravity and Topography of the Terrestrial Planets. In G. Schubert (Ed.), *Treatise on Geophysics (Second Edition)* (pp. 153–193). Oxford: Elsevier. https://doi.org/10.1016/B978-0-444-53802-4.00169-X

Wieczorek, M. A., Neumann, G. A., Nimmo, F., Kiefer, W. S., Taylor, G. J., Melosh, H. J., et al. (2013). The Crust of the Moon as Seen by GRAIL. *Science*, *339*, 671–675. https://doi.org/10.1126/science.1231530

Williams, Q. (2009). Bottom-up versus top-down solidification of the cores of small solar system bodies: Constraints on paradoxical cores. *Earth and Planetary Science Letters*, *284*(3), 564–569. https://doi.org/10.1016/j.epsl.2009.05.019

Yang, J., Goldstein, J. I., & Scott, E. R. D. (2007). Iron meteorite evidence for early formation and catastrophic disruption of protoplanets. *Nature*, *446*, 888–891. https://doi.org/10.1038/nature05735

Yang, J., Goldstein, J. I., & Scott, E. R. D. (2008). Metallographic cooling rates and origin of IVA iron meteorites. *Geochimica et Cosmochimica Acta*, *72*(12), 3043–3061. https://doi.org/10.1016/j.gca.2008.04.009

Yang, J., Goldstein, J. I., Michael, J. R., Kotula, P. G., & Scott, E. R. D. (2010). Thermal history and origin of the IVB iron meteorites and their parent body. *Geochimica et Cosmochimica Acta*, *74*(15), 4493–4506. https://doi.org/10.1016/j.gca.2010.04.011

Yomogida, K., & Matsui, T. (1983). Physical properties of ordinary chondrites. *Journal of Geophysical Research: Solid Earth*, *88*(B11), 9513–9533. https://doi.org/10.1029/JB088iB11p09513

Young, H. D. (1992). *University physics.* (8th ed.). Reading, Mass: Addison-Wesley Pub. Co.

Yu, S., Tosi, N., Schwinger, S., Maurice, M., Breuer, D., & Xiao, L. (2019). Overturn of Ilmenite-Bearing Cumulates in a Rheologically Weak Lunar Mantle. *Journal of Geophysical Research: Planets*, *124*(2), 418–436. https://doi.org/10.1029/2018JE005739

Zhang, Z., Bercovici, D., & Elkins-Tanton, L. (2022). Cold Compaction and Macro-Porosity Removal in Rubble-Pile Asteroids: 2. Applications. *Journal of Geophysical Research: Planets*, *127*(10), e2022JE007343. https://doi.org/10.1029/2022JE007343

Zuber, M. T., Park, R. S., Elkins-Tanton, L. T., Bell, J. F., Bruvold, K. N., Bercovici, D., et al. (2022). The Psyche Gravity Investigation. *Space Science Reviews*, *218*(8), 57. https://doi.org/10.1007/s11214-022-00905-3

Tables

Parameter	Description	Value
$\boldsymbol{M}$	Planetary Mass[a]	2.3×10^{19} kg
$\boldsymbol{T_{0,m}}$	Initial Temperature, silicate shell	1,300 K
$\boldsymbol{T_{0,c}}$	Initial Temperature, core	1,820 K
$\boldsymbol{T_{surf}}$	Surface Temperature[b]	137 K
$\boldsymbol{\rho_m}$	Density, silicate shell[c,d]	3,300 kg/m³
$\boldsymbol{\rho_c}$	Density, solid Fe[e]	7,500 kg/m³
$\boldsymbol{\rho_c}$	Density, liquid core[f]	$6{,}950 - 5176\chi - 3108\chi^2$ kg/m³
$\boldsymbol{k_m}$	Thermal Conductivity, silicate shell[g]	3 W/m K
$\boldsymbol{k_{Fe}}$	Thermal Conductivity, solid Fe[h]	30 W/m K
$\boldsymbol{k_\ell}$	Thermal Conductivity, liquid Fe[h]	40 W/m K
$\boldsymbol{k_{FeS}}$	Thermal Conductivity, FeS[i]	4.6 W/m K
$\boldsymbol{C_{p,m}}$	Specific Heat Capacity, silicate shell[g]	1,000 J/kg K
$\boldsymbol{C_{p,Fe}}$	Specific Heat Capacity, Fe[j]	835 J/kg K
$\boldsymbol{C_{p,FeS}}$	Specific Heat Capcity, FeS[k,l]	600 J/kg K
$\boldsymbol{L_{Fe}}$	Latent Heat of fusion, Fe[m]	2.56×10^5 J/kg
$\boldsymbol{L_{FeS}}$	Latent Heat of Fusion, FeS[n]	1.33×10^5 J/kg
$\boldsymbol{\alpha_m}$	Thermal expansivity, silicate shell[o]	2×10^{-5} 1/K
$\boldsymbol{\alpha_{Fe}}$	Thermal Expansivity, Fe[p]	9.2×10^{-5} 1/K
$\boldsymbol{V_{\ell iq}}$	Specific Volume, liquid Fe[p]	7.956 cm³/mol
$\boldsymbol{V_\gamma}$	Specific Volume, γ-Fe[q]	7.533 cm³/mol
$\boldsymbol{V_\alpha}$	Specific Volume, α-Fe[r]	7.578 cm³/mol

[a]Elkins-Tanton et al. (2020). [b]Sori et al. (2017). [c]Johnson et al. (2020). [d]Wieczorek et al. (2013). [e]Scheinberg et al. (2016). [f]Morard et al. (2018). [g]Bierson & Nimmo (2019). [h]Touloukian et al. (1970). [i]Yomogida & Matsui (1983). [j]Desai (1986). [k]Chase (1998). [l]Helffrich (2017). [m]Young (1992). [n]Fulton (1910). [o]Turcotte & Schubert (2002). [p]Anderson & Ahrens (1994). [q]Ahrens et al. (2002). [r]Miettinen (1997).

Table 1. Psyche material properties and parameter values used in this work.

Figures

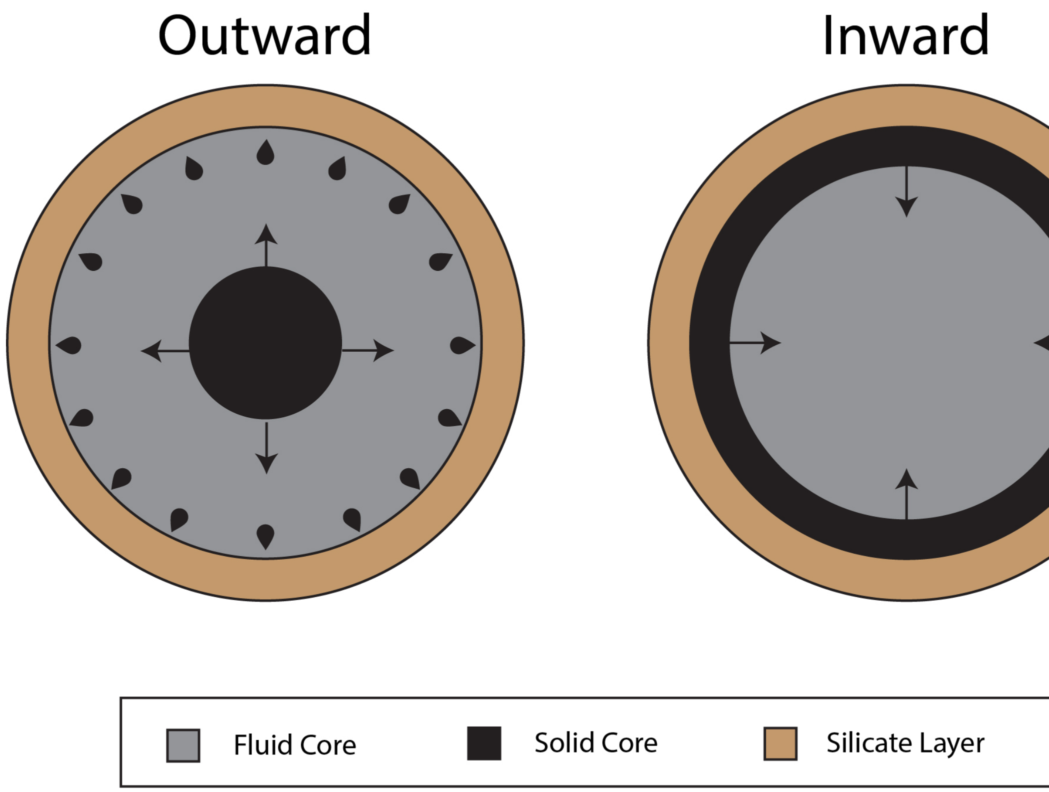

Figure 1. Schematic illustrating concentric outward solid core growth (left) and concentric inward solid core growth (right). For outward solid core growth, solid core material nucleates at the top of the core and instantaneously settles to the base of the fluid core. For inward solid core growth, the solid outer core grows from in-place crystallization at the top of the fluid core.

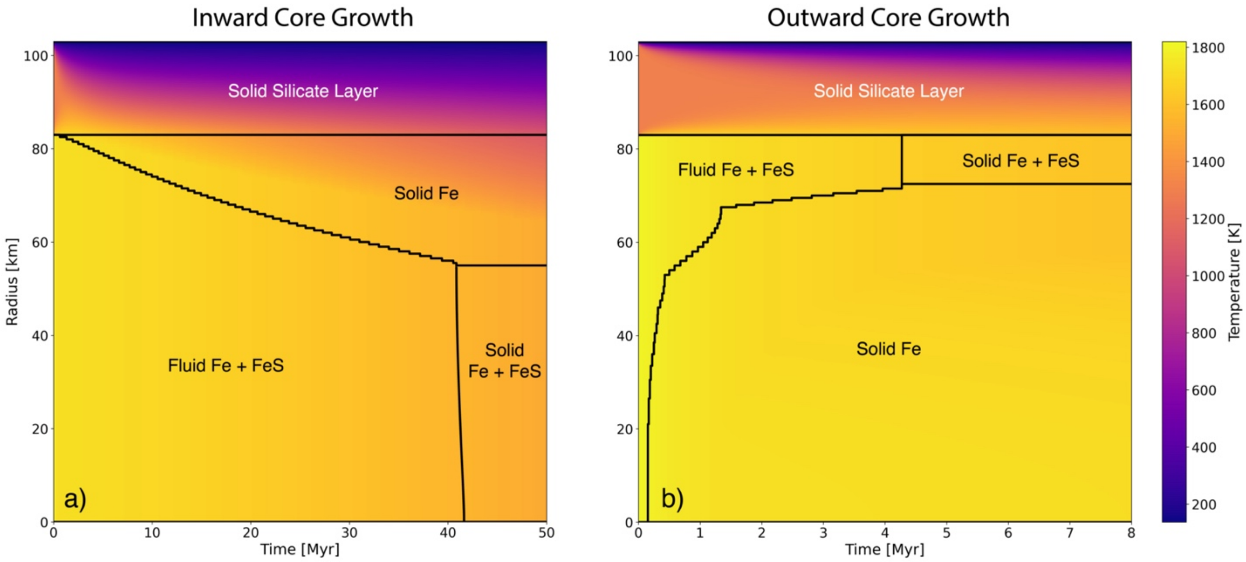

Figure 2. Thermal evolution of Psyche with a silicate outer layer thickness of 20 km and initial core sulfur content of 5 wt.% for (a) inward and (b) outward core growth. Compositions and state (fluid or solid) of materials are shown. Please note the different timescales covered for inward and outward core growth, 50 and 8 Myr, respectively.

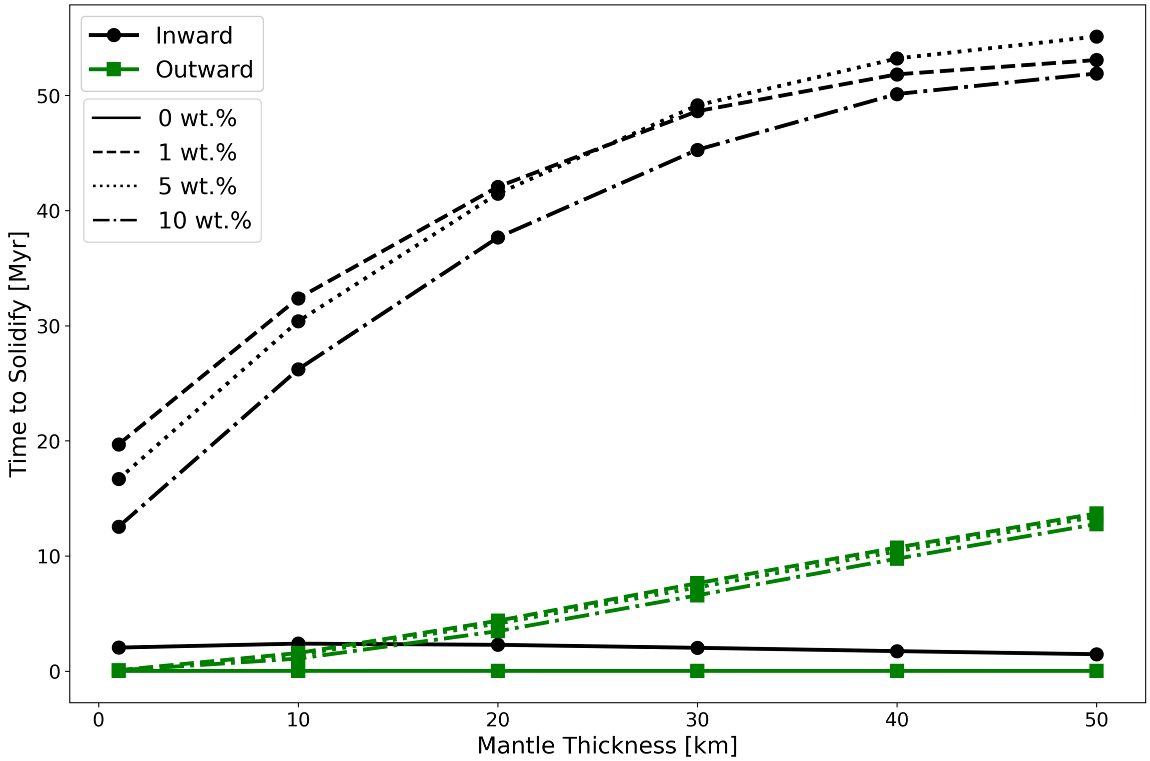

Figure 3. Core solidification timescales for a range of silicate layer thicknesses (1, 10, 20, 30, 40, and 50 km). Models of inward (black circles) and outward (green square) growth directions are shown. The times are determined between the beginning and ending of core solidification and solid, dashed, dotted, and dash-dotted lines represent models with 0, 1, 5, and 10 wt.% initial core sulfur contents, respectively.

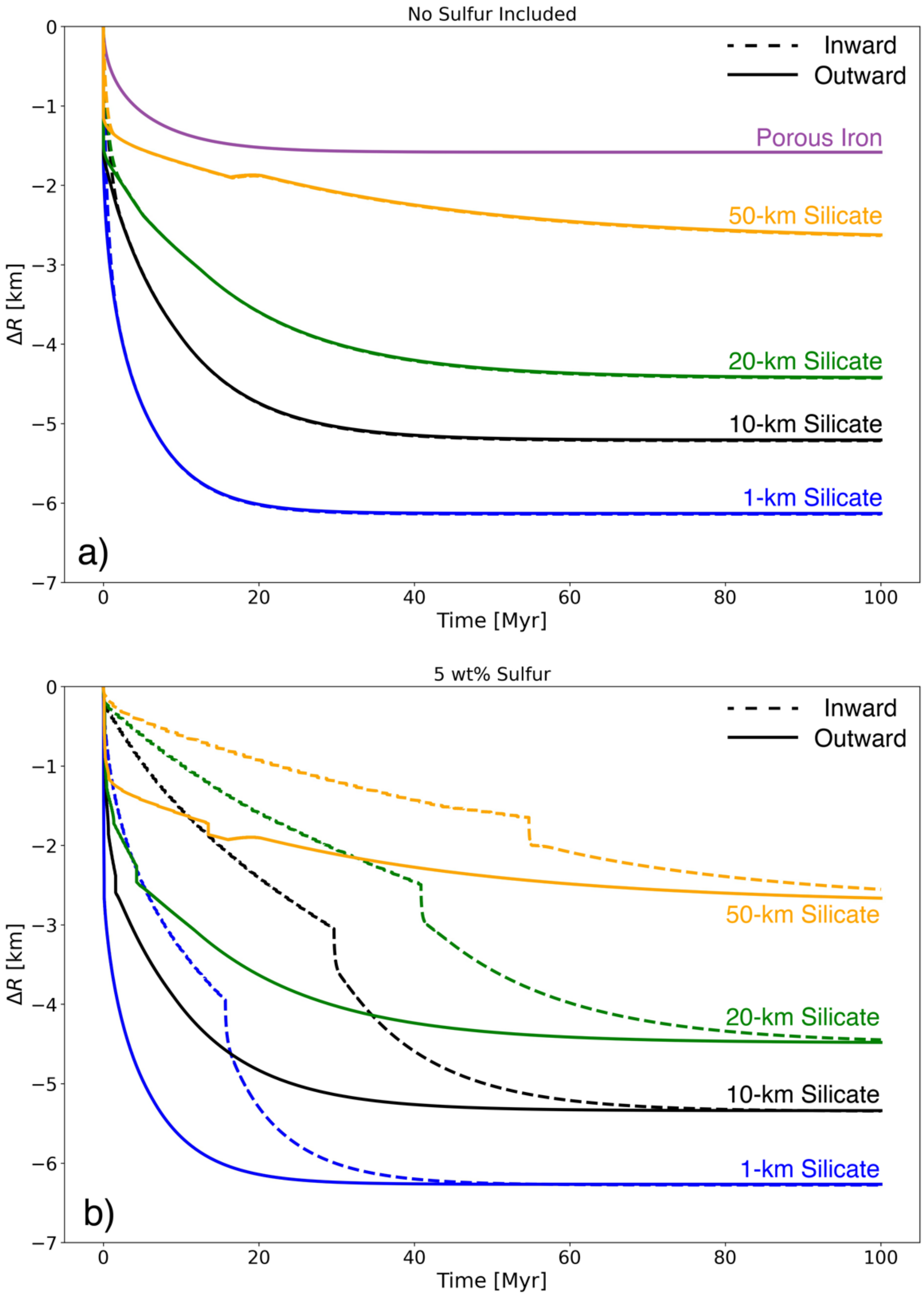

Figure 4. Radial contraction for Psyche with initial core sulfur content of (a) 0 wt.% and (b) 5 wt.%. Outer silicate layer thicknesses of 1 (blue), 10 (black) , 20 (green), and 50 km (orange) are shown. Inward (dashed) and outward core (solid) growth processes are both included. For reference, the porous iron Psyche model (600-K initial temperature, 52-vol.% initial porosity) of Nichols-Fleming et al., 2022 (purple) is also shown in (a).

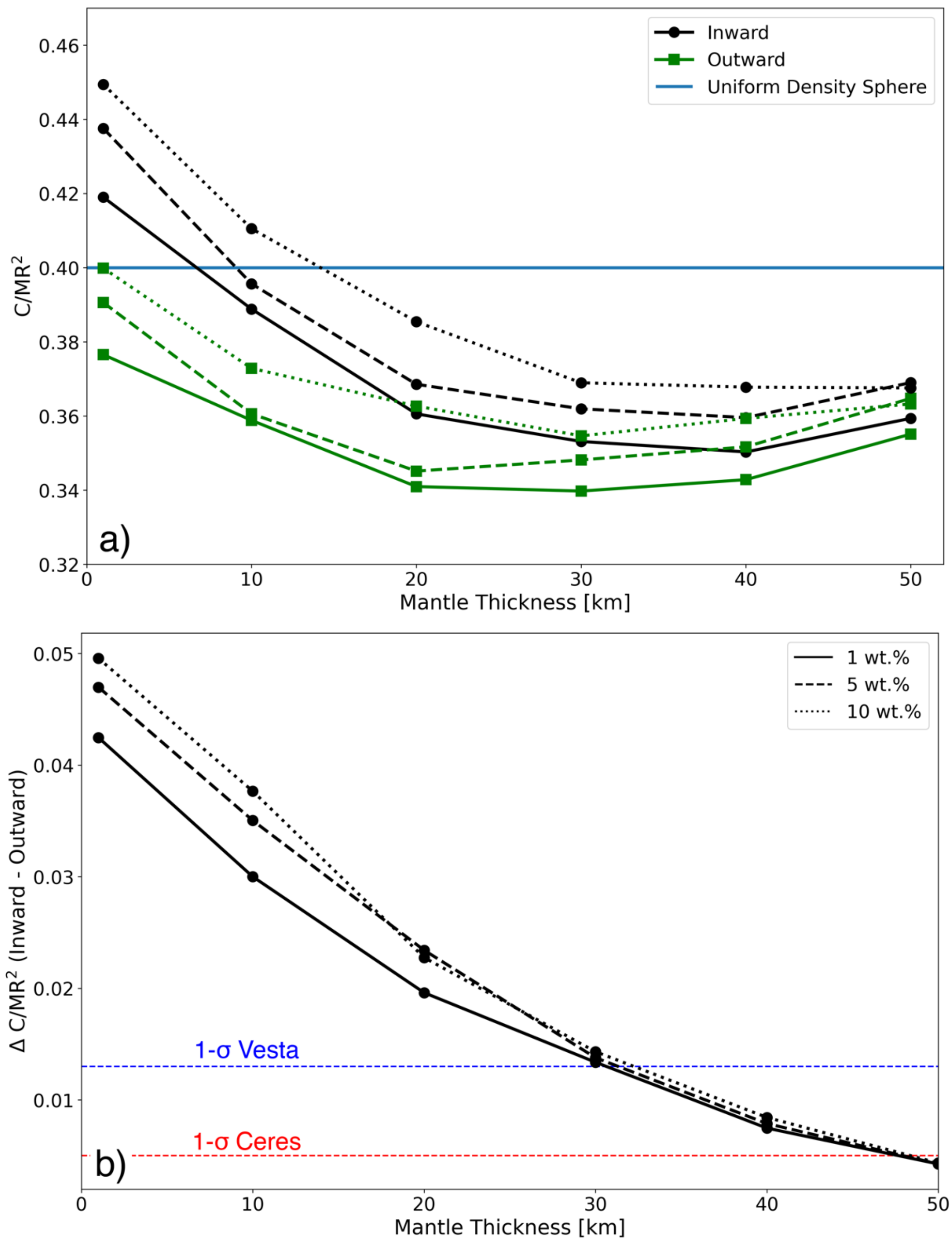

Figure 5. (a) MOI ratios for a range of silicate layer thickness (1, 10, 20, 30, 40, and 50 km). Models of inward (black circles) and outward (green squares) growth directions are shown. Solid, dashed, and dotted lines represent models with 1, 5, and 10 wt.% initial core sulfur contents, respectively, and the blue horizontal line represents the MOI ratio for a sphere of constant density. (b) The difference in MOI ratios for inward and outward core growth with silicate layer thicknesses of 1, 10, 20, 30, 40, and 50 km. Dashed lines showing the 1-σ uncertainties in MOI ratios of Vesta and Ceres from Vaillant et al. (2019) are shown in blue and red, respectively.

Supplemental Figures

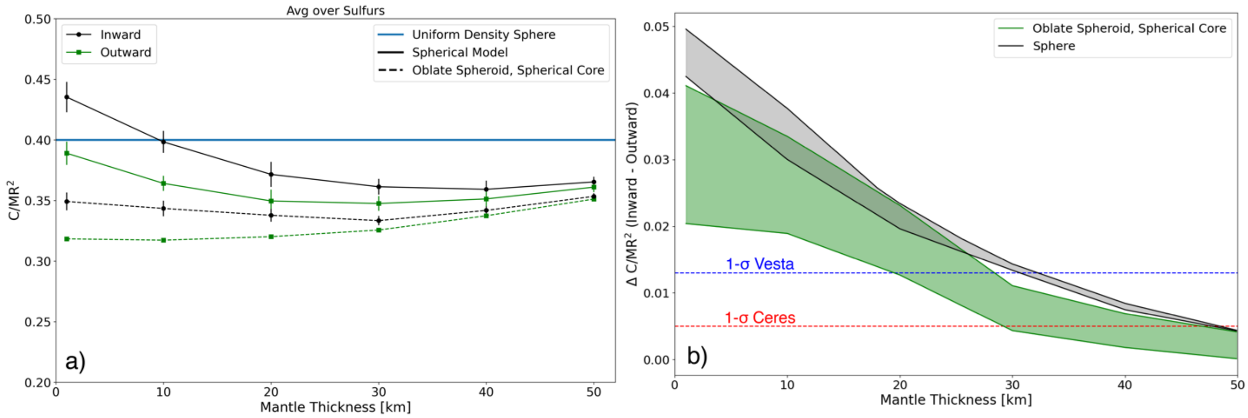

Figure S1. (a) MOI ratios for a range of silicate layer thickness (1, 10, 20, 30, 40, and 50 km). Models of inward (black circles) and outward (green squares) growth directions are shown for a spherical shape (solid lines) and an oblate shape with a spherical core (dashed lines). Values are averaged over models with 1, 5, and 10 wt.% initial core sulfur contents with error bars indicating the standard deviation of these values across the range of sulfur contents and the blue horizontal line represents the MOI ratio for a sphere of constant density. (b) The difference in MOI ratios for inward and outward core growth with silicate layer thicknesses of 1, 10, 20, 30, 40, and 50 km. The grey and green shaded regions show the variation in these differences due to initial sulfur contents between 1 and 10 wt.% for the spherical shape and oblate shape with a spherical core, respectively. Dashed lines showing the 1-σ uncertainties in MOI ratios of Vesta and Ceres from Vaillant et al. (2019) are shown in blue and red, respectively.

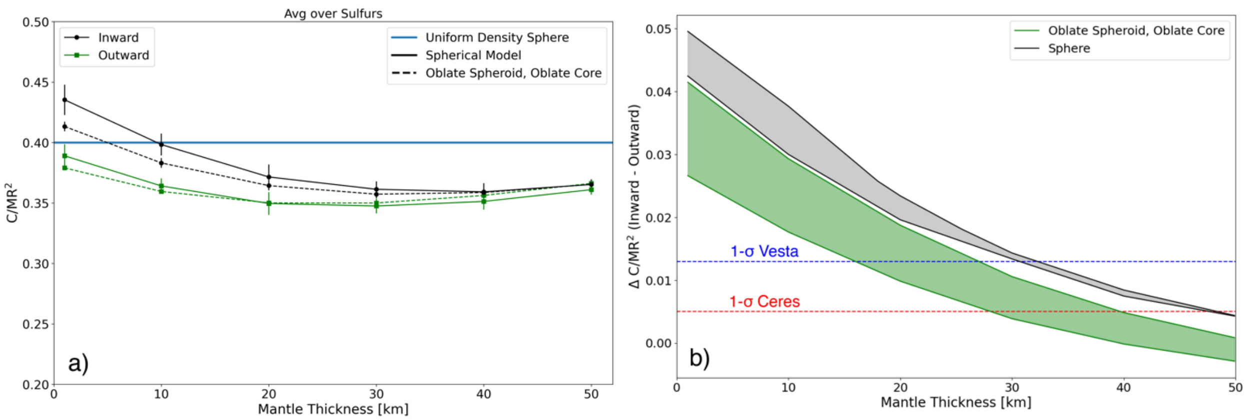

Figure S2. (a) MOI ratios for a range of silicate layer thickness (1, 10, 20, 30, 40, and 50 km). Models of inward (black circles) and outward (green squares) growth directions are shown for a spherical shape (solid lines) and an oblate shape with an oblate core (dashed lines). Values are averaged over models with 1, 5, and 10 wt.% initial core sulfur contents with error bars indicating the standard deviation of these values across the range of sulfur contents and the blue horizontal line represents the MOI ratio for a sphere of constant density. (b) The difference in MOI ratios for inward and outward core growth with silicate layer thicknesses of 1, 10, 20, 30, 40, and 50 km. The grey and green shaded regions show the variation in these differences due to initial sulfur contents between 1 and 10 wt.% for the spherical shape and oblate shape with an oblate core, respectively. Dashed lines showing the 1-σ uncertainties in MOI ratios of Vesta and Ceres from Vaillant et al. (2019) are shown in blue and red, respectively.

Conclusions and Future Outlook

Fiona Nichols-Fleming

Department of Earth, Environmental and Planetary Sciences, Brown University, Providence, RI

In this dissertation, we have explored the magnetic and thermal evolutions of two ancient solar system bodies. For the Moon, we investigated a new process to modify and enhance the strength of the very early era of the lunar dynamo in Chapter 2. We determined that accretion of cool impactor core material could introduce variability and increase the surface field intensities of an existing core dynamo for a short period of time ($\lesssim 10{,}000$ years), however cool impact core material could not be solely responsible for the high-intensity era of the lunar magnetic paleorecord. Additionally, we have studied the thermal evolution of the asteroid 16 Psyche for a range of hypothesized interior compositions in Chapters 3 and 4. We first determined that a highly porous iron composition for Psyche is unlikely based upon the cool temperatures ($\lesssim 800$ K) required to retain porosities above 50% until today (Nichols-Fleming et al., 2022). Based on this work, we then used a different model of Psyche composed of an iron-sulfur core and a silicate outer layer to predict how the observable moment of inertia and tectonic record may inform the interior structure and the process of core solidification. In this chapter, I focus on some of the major unanswered questions that remain for the Moon and Psyche and how work stemming from this dissertation can address these questions in the future.

Although we've been exploring the Moon for over 60 years, many unresolved scientific questions remain. Particularly, the existence of a lunar dynamo along with the source of variability and surprisingly high intensities early in the paleomagnetic record continue to be active areas of debate within the community (e.g., Tarduno et al., 2021; Tikoo & Evans, 2022; Weiss & Tikoo, 2014). While our work cannot solely explain the lunar paleomagnetic record, a combination of our model and other mechanisms that can produce intermittently high magnetic field intensities should be considered. Additionally, further work modeling asymmetric layers of impactor material on the lunar core-mantle boundary, mixing of impactor core material with the lunar core, and explicit modeling of the three-dimensional dynamo process will be able to provide a more complete insight into how cool material at the core-mantle boundary influences a core dynamo. Furthermore, although our models were specifically tailored to the Moon, we would expect the accretion of impactor core material to occur on other solar system bodies as well. Thus, for any bodies in which a dynamo is inferred from observations or returned samples, short-lived increases in field intensity due to impactor core accretion should be considered along with traditional core convection dynamo models to understand the evolution of their magnetic fields.

For Psyche, it seems like there may be more unanswered than answered scientific questions. The composition and interior structure of Psyche is maybe the largest of these questions and, while this likely won't be solved until the arrival of the Psyche spacecraft, we hope that our work will serve as a point of reference for new data. Continued modeling efforts that include heat production within the silicate outer layer, additional core compositions, and explicit consideration of Psyche's triaxial shape can also provide further insight into the compositions and interior structures that may be consistent with current and future Psyche data. Our thermal models can also be easily applied to other M-type asteroids, as many share the same discrepancy between observations indicating a metal-rich surface (e.g., Shepard et al., 2008, 2010, 2015, 2017) and densities much lower than meteoritic metal (e.g., Descamps et al., 2008; Elkins-Tanton et al., 2020; Marchis et al., 2021; Pätzold et al., 2011; Sierks et al., 2011). Additionally, the simple thermal models for a differentiated Psyche can be combined with the smoothed-particle hydrodynamics (SPH) models of hit-and-run collisions (e.g., Asphaug et al., 2006) to determine the relationship between mantle-stripping events and thermal evolution. Finally, models of the relationship between thermal evolution and tectonic history can be applied to many other bodies throughout the solar system similar to what has been done previously for the Moon and Mercury (e.g., Byrne et al., 2014; Solomon, 1977; Solomon & Chaiken, 1976; Watters, 2021). This may be particularly interesting for bodies where extensive mapping of the surface has already been completed, such as the asteroid Vesta or outer solar system moons like Ganymede, Callisto, Enceladus, and Dione. In these cases, direct comparisons can immediately be made between their thermal evolution, interior structure, and observed record of tectonic activity.

Throughout this dissertation we have investigated the thermal and magnetic evolutions of two planetary bodies that remain as remnants of the early era of the solar system and discussed the promise for future work relating the modeling of planetary interiors to observable data. Each of these projects emphasize the central theme of this work: understanding the geophysical evolution of solar system bodies in the context of their observable features and data. With the next few decades containing planned human exploration of the Moon and a dedicated mission to Psyche, the importance of this type of modeling will undoubtedly continue to grow along with these efforts.

References

Asphaug, E., Agnor, C. B., & Williams, Q. (2006). Hit-and-run planetary collisions. *Nature*, *439*, 155–160. https://doi.org/10.1038/nature04311

Byrne, P. K., Klimczak, C., Celâl Şengör, A. M., Solomon, S. C., Watters, T. R., & Hauck, I. I. (2014). Mercury's global contraction much greater than earlier estimates. *Nature Geoscience*, *7*(4), 301–307. https://doi.org/10.1038/ngeo2097

Descamps, P., Marchis, F., Pollock, J., Berthier, J., Vachier, F., Birlan, M., et al. (2008). New determination of the size and bulk density of the binary Asteroid 22 Kalliope from observations of mutual eclipses. *Icarus*, *196*(2), 578–600. https://doi.org/10.1016/j.icarus.2008.03.014

Elkins-Tanton, L. T., Asphaug, E., Bell, J. F., Bercovici, H., Bills, B., Binzel, R., et al. (2020). Observations, Meteorites, and Models: A Preflight Assessment of the Composition and Formation of (16) Psyche. *Journal of Geophysical Research (Planets)*, *125*, e06296. https://doi.org/10.1029/2019JE006296

Marchis, F., Jorda, L., Vernazza, P., Brož, M., Hanuš, J., Ferrais, M., et al. (2021). (216) Kleopatra, a low density critically rotating M-type asteroid. *Astronomy & Astrophysics*, *653*, A57. https://doi.org/10.1051/0004-6361/202140874

Nichols-Fleming, F., Evans, A. J., Johnson, B. C., & Sori, M. M. (2022). Porosity Evolution in Metallic Asteroids: Implications for the Origin and Thermal History of Asteroid 16 Psyche. *Journal of Geophysical Research: Planets*, *127*(2), e2021JE007063. https://doi.org/10.1029/2021JE007063

Pätzold, M., Andert, T. P., Asmar, S. W., Anderson, J. D., Barriot, J.-P., Bird, M. K., et al. (2011). Asteroid 21 Lutetia: Low Mass, High Density. *Science*, *334*(6055), 491–492. https://doi.org/10.1126/science.1209389

Shepard, M. K., Clark, B. E., Nolan, M. C., Howell, E. S., Magri, C., Giorgini, J. D., et al. (2008). A radar survey of M- and X-class asteroids. *Icarus*, *195*(1), 184–205. https://doi.org/10.1016/j.icarus.2007.11.032

Shepard, M. K., Clark, B. E., Ockert-Bell, M., Nolan, M. C., Howell, E. S., Magri, C., et al. (2010). A radar survey of M- and X-class asteroids II. Summary and synthesis. *Icarus*, *208*(1), 221–237. https://doi.org/10.1016/j.icarus.2010.01.017

Shepard, M. K., Taylor, P. A., Nolan, M. C., Howell, E. S., Springmann, A., Giorgini, J. D., et al. (2015). A radar survey of M- and X-class asteroids. III. Insights into their composition, hydration state, & structure. *Icarus*, *245*, 38–55. https://doi.org/10.1016/j.icarus.2014.09.016

Shepard, M. K., Richardson, J., Taylor, P. A., Rodriguez-Ford, L. A., Conrad, A., de Pater, I., et al. (2017). Radar observations and shape model of asteroid 16 Psyche. *Icarus*, *281*, 388–403. https://doi.org/10.1016/j.icarus.2016.08.011

Sierks, H., Lamy, P., Barbieri, C., Koschny, D., Rickman, H., Rodrigo, R., et al. (2011). Images of Asteroid 21 Lutetia: A Remnant Planetesimal from the Early Solar System. *Science*, *334*(6055), 487–490. https://doi.org/10.1126/science.1207325

Solomon, S. C. (1977). The relationship between crustal tectonics and internal evolution in the moon and Mercury. *Physics of the Earth and Planetary Interiors*, *15*(2), 135–145. https://doi.org/10.1016/0031-9201(77)90026-7

Solomon, S. C., & Chaiken, J. (1976). Thermal expansion and thermal stress in the moon and terrestrial planets: clues to early thermal history. *Lunar and Planetary Science Conference Proceedings*, *3*, 3229–3243.

Tarduno, J. A., Cottrell, R. D., Lawrence, K., Bono, R. K., Huang, W., Johnson, C. L., et al. (2021). Absence of a long-lived lunar paleomagnetosphere. *Science Advances*, *7*(32), eabi7647. https://doi.org/10.1126/sciadv.abi7647

Tikoo, S. M., & Evans, A. J. (2022). Dynamos in the Inner Solar System. *Annual Review of Earth and Planetary Sciences*, *50*(1), 99–122. https://doi.org/10.1146/annurev-earth-032320-102418

Watters, T. R. (2021). A case for limited global contraction of Mercury. *Communications Earth & Environment*, *2*(1), 1–9. https://doi.org/10.1038/s43247-020-00076-5

Weiss, B. P., & Tikoo, S. M. (2014). The lunar dynamo. *Science*, *346*(6214), 1198. https://doi.org/10.1126/science.1246753